Nano-cellular Microstructure Evolution In Ion-Induced Chemical Vapor Deposition (II-CVD) Of Copper

by

Francis L. Ross III

S.B. Metallurgy and Materials Science
Columbia University (1990)

Submitted to the Department of Materials Science and Engineering in Partial Fulfillment of the Requirements for the Degree of

Doctor of Philosophy in Materials Science and Engineering

at the

Massachusetts Institute of Technology
September 2003

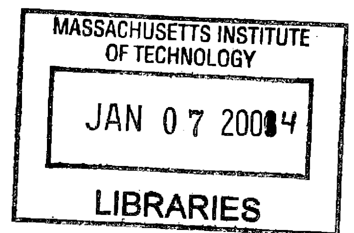
MASSACHUSETTS INSTITUTE OF TECHNOLOGY
JAN 07 2004
LIBRARIES

© 2003 Massachusetts Institute of Technology
All rights reserved

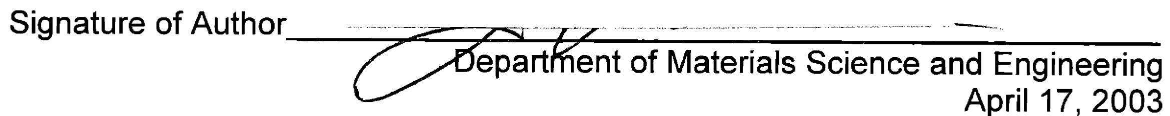

Signature of Author ____________________
Department of Materials Science and Engineering
April 17, 2003

Certified by ____________________
Carl V. Thompson
Matoula Salapatas Professor of Materials Science and Engineering
Thesis Advisor

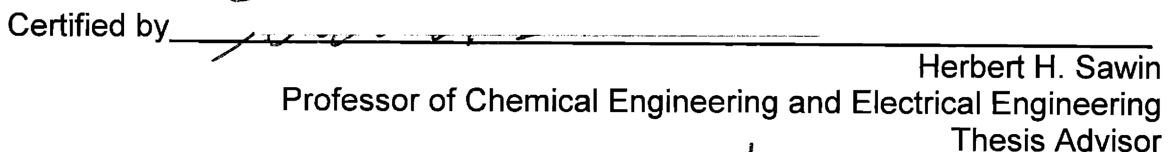

Certified by ____________________
Herbert H. Sawin
Professor of Chemical Engineering and Electrical Engineering
Thesis Advisor

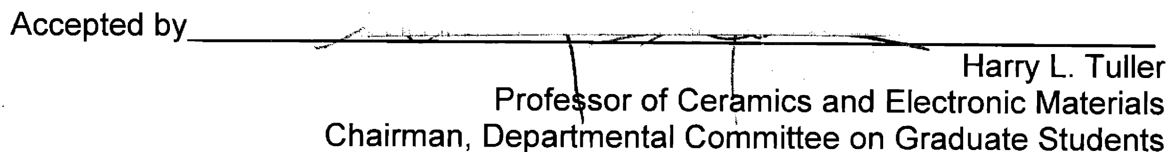

Accepted by ____________________
Harry L. Tuller
Professor of Ceramics and Electronic Materials
Chairman, Departmental Committee on Graduate Students

ARCHIVES

Nano-cellular Microstructure Evolution In Ion Induced Chemical Vapor Deposition (II-CVD) Of Copper

by
Francis L. Ross III

Submitted to the Department of Materials Science and Engineering on April 17, 2003 in Partial Fulfillment of the Requirements for the Degree of Doctor of Philosophy in Materials Science and Engineering

Abstract

A systematic investigation of the microstructure produced in ion-induced chemical vapor deposition (II-CVD) of copper from copper(I)hexafluoroacetylacetonatevinyltrimethylsilane (Cu(I)hfacVTMS) gas precursor is reported. II-CVD involves the ion-driven decomposition of Cu(I)hfacVTMS and subsequent deposition of copper films at ambient temperature. The thin films were grown with the aid of a broad beam Kaufman source in a "multibeam apparatus", which allowed monitoring of experimental conditions – growth rate, temperature, ion beam flux, ion beam energy and gas precursor flux. Deposition temperatures ranged from room temperature to 100°C. The desirable operation range is the "ion-flux-limited regime", in which sufficient precursor flux allows the growth rate to scale with the ion flux.

Plan-view TEM and cross-sectional TEM (XTEM) show that the film develops a characteristic cellular microstructure of continuous crystalline copper columns (15 nm diameter) surrounded by an amorphous phase containing both carbon impurity and copper. The column diameter increases with temperature but is not affected by the growth rate for temperatures up to 60°C. At higher temperatures, the growth mechanism is not purely ion driven due to the onset of thermal CVD. However, quantitative XPS (x-ray photoelectron spectroscopy) shows that the film purity not only increases with substrate temperature, but also increases with decreasing growth rate due to the kinetics of byproduct desorption. STEM-EDS (scanning transmission electron microscopy - energy dispersive x-ray spectroscopy) shows that the intercolumnar spaces contain more copper at lower growth rates for a given substrate temperature.

Hydrogen-atom-assisted II-CVD effectively removed all carbonaceous impurity to within the detection limit of XPS. The cellular microstructure is not observed in these films; however, deposition at 100°C produces films that still retain a columnar structure even though the atomic fraction of carbon is only ~0.5%. This high temperature growth process has a mixed mechanism where the ion beam flux also enhances the kinetics of the thermal CVD process.

The microstructure evolution is modeled as a cellular growth process that is controlled by surface transport of carbon impurity. The cellular mechanism is corroborated by the sharp transitions observed in XTEM for a change in deposition conditions. The surface diffusion is not only a function of temperature but also the ion flux. This explains why the column diameter remains independent of growth rate at constant temperature. The model assumes an approximately linear dependence of the diffusion constant's pre-exponential factor with ion the flux. The model predicts column diameters that are in good agreement with experimental data. The model was designed to integrate with Chiang's kinetic model to provide a foundation for depositing controlled microstructures using II-CVD.

The work presented here demonstrates the possibility of growing controlled nano-cellular microstructures using a low voltage broad ion beam at or near ambient temperature. Films with such nano-cellular structures are expected to have highly anisotropic properties that could be used in a variety of applications, including magnetics. It is possible that other metallic nanostructures with specific functionality could be deposited using other precursors with the appropriate chemistry.

Thesis Supervisor: Carl V. Thompson
Title: Matoula Salapatas Professor of Materials Science and Engineering

Thesis Supervisor: Herbert H. Sawin
Title: Professor of Chemical Engineering and Electrical Engineering

Table of Contents

ACKNOWLEDGEMENTS **7**

CHAPTER 1: INTRODUCTION **8**

1.1 The II-CVD process 9

1.2 Motivation 9

1.3 Background 13

1.4 Physical Model 15

1.5 Kinetic Model 19

1.6 Removal of Carbon Impurity by Hydrogen Atom Beam 23

1.7 Microstructure 25

1.8 Objectives 28

CHAPTER 2: EXPERIMENTAL HARDWARE AND ANALYTICAL TECHNIQUES **31**

2.1 Multibeam Vacuum Chamber 31

2.2 Quartz Crystal Microbalance (QCM) Assembly 34

2.3 Gas Precursor. 38

2.4 Ion Gun 41

2.5 Hydrogen atom beam source 48

2.6 Ion Probe 53

2.7 Transmission Electron Microscopy (TEM) 55

2.8 Cross-sectional Transmission Electron Microsocpy (XTEM) 57

2.9 Atomic Force Microscopy & Scanning Electron Microscopy 60

2.10 X-ray Photoelectron Spectroscopy 61

2.11 Scanning Transmission Electron Microscopy (STEM) & Energy-Dispersive X-ray Spectroscopy (EDS) 64

2.12 Resistivity 66

CHAPTER 3: EXPERIMENTAL RESULTS **68**

3.1 CHEMISTRY AND ADSORPTION OF CU(I)HFAC(VTMS) PRECURSOR 68
3.2 RATE EXPERIMENTS 72
3.3 QUANTITATIVE MICROSCOPY 76
3.3.1 Column Diameter *76*
3.3.2 Volume fraction *78*
3.3.3 Interface Area per Unit Volume and Mean Free Path *79*
3.3.4 Validity of Quantitative Analysis *79*
3.3.5 Volume Fraction by Point Counting *81*
3.4 MICROSTRUCTURE EVOLUTION: ION-FLUX-LIMITED REGIME 82
3.5 MICROSTRUCTURE EVOLUTION: GAS FLUX LIMITED REGIME 98
3.6 TEM DIFFRACTION 102
3.7 H-ATOM ASSISTED II-CVD 105
3.8 XPS QUANTITATIVE ANALYSIS. 108
3.9 STEM-EDS ANALYSIS 113
3.10 MICROSTRUCTURE EVOLUTION: ION BEAM VOLTAGE 118
3.11 TOPOGRAPHY: AFM AND SEM 125
3.12 SUMMARY 128

CHAPTER 4: MICROSTRUCTURE MODEL **131**

4.1 REVISITING THE KINETIC MODEL 131
4.2 CELLULAR GROWTH 138
4.3 SURFACE DIFFUSION 145
4.4 THE MICROSTRUCTURE MODEL 147
4.4.1 Surface Diffusion Modeling In The Literature *149*
4.4.2 Microstructure Model for II-CVD *150*
4.4.3 Activation Energy for Surface Diffusion *154*
4.4.4 Testing The Model: Ion-Flux-Limited Regime *155*
4.4.5 Testing The Model: Ion Beam Voltage *161*
4.4.6 Testing The Model In the Gas-Flux-Limited Regime *163*

4.5 "HIGH" TEMPERATURE II-CVD 165
4.6 DISCUSSION 169
CHAPTER 5: CONCLUSIONS AND FUTURE WORK 172
APPENDIX A: VOLUME FRACTION OF CLOSE PACKED COLUMNS 174
APPENDIX B: MICROSTRUCTURE MODEL 175
APPENDIX C: GLOSSARY 178
ENDNOTES 179

Acknowledgements

I would like to thank my advisors, Professors Thompson and Sawin, for giving me the opportunity to conduct this very interesting research and their understanding regarding the delayed completion. The National Science Foundation funded the research under DMR-9202633. I would also like to thank my lab partner Tony Chiang for his assistance and collaboration. In addition, thanks to my committee members, Professors Sadoway and Russell.

I dedicate this work to Cat and my Father. I am very sad that I did not complete it before his death.

Chapter 1: Introduction

The term, "Ion-Induced Chemical Vapor Deposition" (II-CVD), was coined to provide a more accurate description of the deposition mechanism. Past research at MIT refers to "ion beam induced deposition", which is often confused with the more common "ion assisted deposition" processes or even ion sputter deposition. The key difference between II-CVD and thermal CVD is that the latter is pyrolytic while the former requires energy transfer from an impinging ion beam.

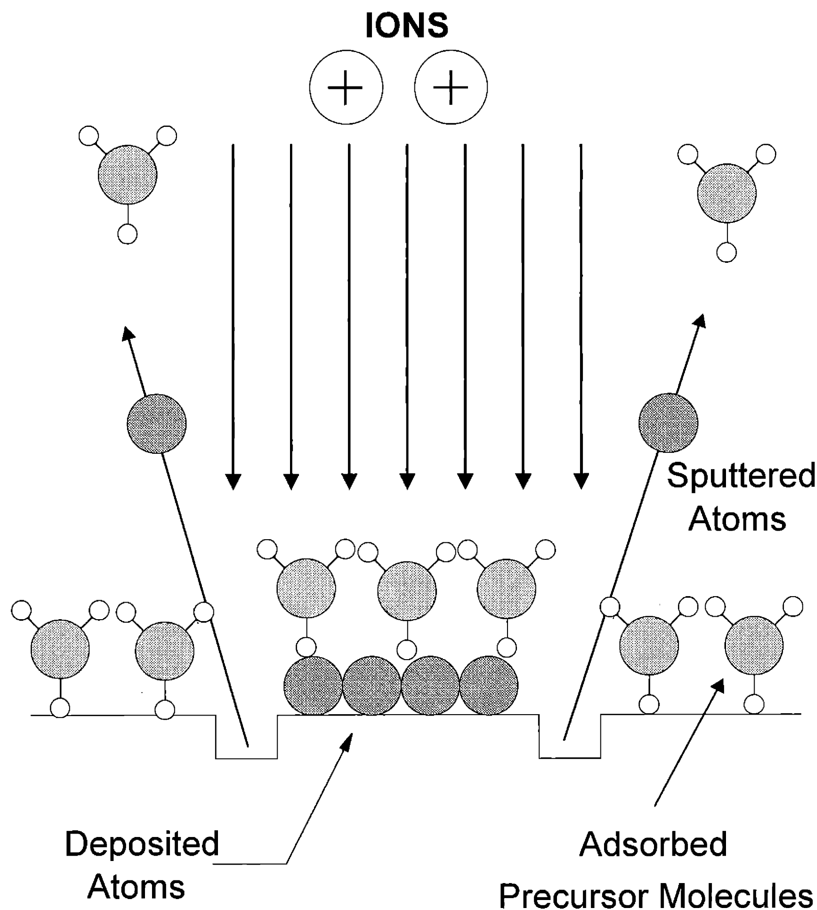

Figure 1.1: Illustration of II-CVD. Atoms deposit when the ion beam impinges on substrate area covered with adsorbed precursor. The ion beam sputters the surface atoms if no gas molecules are absorbed. Insufficiently rapid replenishment of the adsorbed layer leads to net sputtering.

1.1 The II-CVD process

A Metalorganic-CVD (MOCVD) precursor adsorbs onto a substrate. The impinging ions decompose the adsorbed precursor to deposit metal and, inevitably, carbonaceous residue. Local dosing of the precursor minimizes the gas load on the vacuum system, which maintains a sufficiently long mean free path so that the ion beam does not scatter. Figure 1.1 provides a schematic of illustration of II-CVD.

1.2 Motivation

This section describes the original motivation for pursuing research into II-CVD. The goal has been to deposit low resistivity metal lines by achieving high purity as carbonaceous residue is eliminated. However, this research evolved into a more fundamental study of the nature of II-CVD and a search for an understanding of the mechanism that leads to the remarkable cellular microstructure shown in Figure 1.2. The groundbreaking understanding of the microstructure evolution is the key achievement of this work. Notwithstanding, the history, applications and original motivation for research in this field are presented in this chapter. Focused Ion Beam (FIB) mask and chip repair are the primary commercial applications of II-CVD. The FIB uses a gallium liquid metal ion source in conjunction with electrostatic lenses to focus an energetic (~25 KeV) ion beam to a spot size below 100 nm. (The minimum spot size of the Micrion 9800 is rated at 8 nm.)[1] The FIB has complementary nanoscale deposition and milling capabilities: the energetic ion beam is used for either high resolution sputtering or II-CVD of metal lines, vias and pads. Analogous to Scanning Electron Microscopes (SEMs), FIB systems image by collecting secondary electrons emitted during fast rastering of the substrate. This allows

the operator to locate and position the sample. Computer controlled beam deflectors allow definition of high resolution features for deposition or milling.

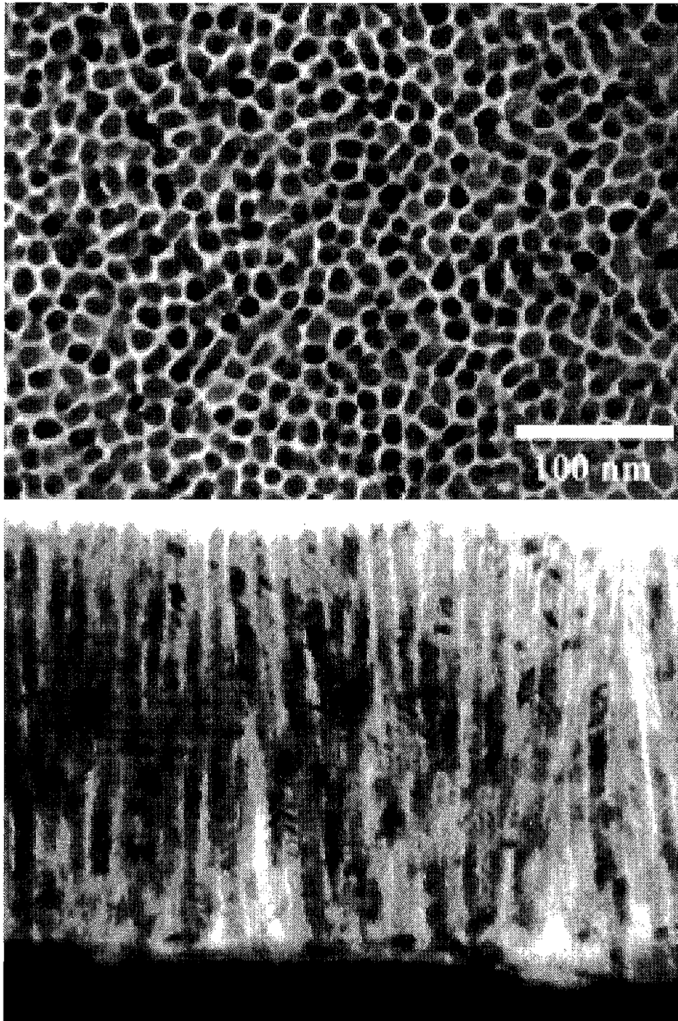

Figure 1.2: Characteristic microstructure of II-CVD copper in plan view (above) and cross-section (below) using 500 eV Argon ions and Cupraselect® precursor at 25°C. The plan view sample is 500 Å thick. The cross-sectional sample exhibits the remarkable aspect ratio of II-CVD films; here, nearly 20:1.

This "cut and patch" technique is employed to repair defective integrated circuit prototypes. FIB milling is used to remove isolation and probe into the device. The FIB cuts off unwanted interconnects and then uses II-CVD to deposit new metal lines. Cut wires are re-isolated by II-CVD of silicon dioxide using a siloxane and

oxygen gas mixture. Figure 1.3 illustrates an example of this application. Another application involves connecting two levels of metal lines (M1 and M2) by milling away the isolation and subsequently depositing a via. A redesign can be implemented in a just a few hours, rather than having to go back and lay out new masks and start from scratch. IBM Analytical reported repairing small lots of wafers in order to keep a development schedule on track.[2] FIB chip repair is especially effective if the chip has more than one defect; conventional processing would require multiple mask iterations. Thus, FIB on-chip redesign reduces the impact of layout and logic errors, which would otherwise lead to higher development costs and longer time to market.

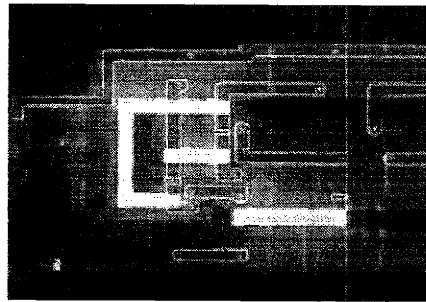

Figure 1.3: FIB circuit wiring repair: three new lines (appear bright) are deposited and three cuts are made. The rightmost cut is on a lower level of metal. From [2].

The main drawback of II-CVD is the high resitivity associated with impurity of the metal films. The standard precursor in commercial FIB systems is tungsten hexacarbonyl ($W(CO)_6$), which deposits tungsten with a resistivity of approximately 200 μΩ-cm (5.3 μΩ-cm for bulk W). Increasing the metal line thickness up to 2 μm decreases the sheet resistance, but 1 Ω/square is still much too high for long wiring runs. IBM's makeshift solution combined II-CVD tungsten local interconnects with laser CVD gold conductors.[3] Note that laser CVD's minimum linewidth is on the order of several microns.

The high resolution of FIB makes it ideal for X-ray lithography mask repair. Sputtering removes opaque defects while II-CVD adds new features. Here, the metal has a high Z number and the impurity content has to be limited in order to achieve adequate x-ray absorption.

Submicron FIB direct-write is a useful research and development tool; however, it is a serial process so it has absolutely no viability as a production tool. On the other hand, ion beam projection lithography (IPL) is competing with x-ray and electron-beam lithography to become the technology of choice if and when optical lithography finally becomes untenable at design rules below 0.10 μm. The Austrian firm, Ion Microfabrication Systems (IMS), was on the forefront of IPL development starting in the mid-1980s.[4] IMS was manufacturing the ion optical column for the Advanced Lithography Group's (ALG) IPL prototype.[5] The system was designed to have <0.02 μm pattern distortion over a $20mm^2$ field with 3X demagnification.[6] Figure 1.4 is a schematic representation of an IPL system. IPL could be modified to accommodate resistless wafer-scale metallization via II-CVD. The development of such a tool lies in the distant future and hinges upon the adoption and successful commercialization of IPL for lithography. Nevertheless, a thorough understanding of the II-CVD mechanism is essential before any serious consideration of potential wafer-scale processing.

Clearly, the capability of depositing pure, low resistivity II-CVD films would improve the viability of FIB chip repair. An obvious solution is substrate heating which serves to enhance organic byproduct removal and reduce the fraction of carbon impurity.

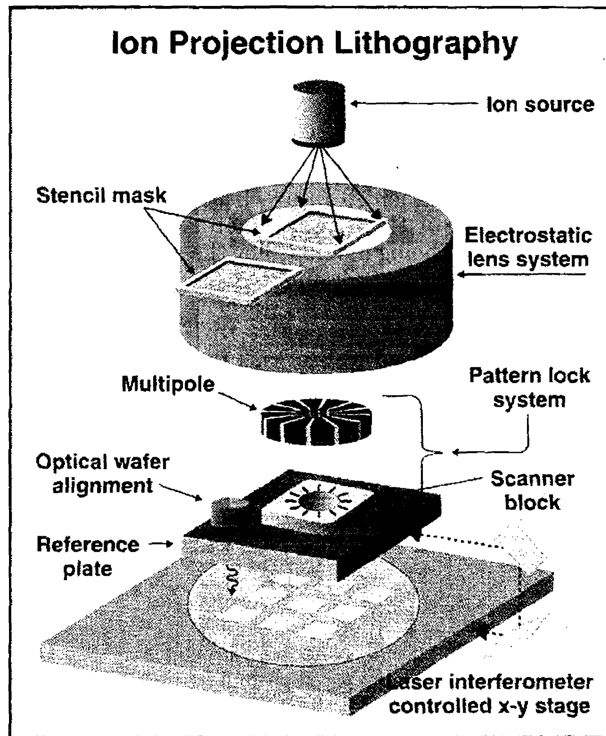

Figure 1.4: Schematic of Ion Projection Lithography system. From [6].

1.3 Background

This section delineates the highlights of the short history of II-CVD processing. II-CVD had not been attempted until 1984 when Gamo used trimethyl aluminum (TMA) to deposit aluminum films, which contained only 20% Al.[7] Table 1-1 summarizes research through the mid 1990s: the focus was primarily to identify and test new precursors. The low purity of the films led to resistivities up to three orders of magnitude greater than the respective pure metal. Gallium appeared as an impurity because the high energy FIB implants the element from the ion source.

Metal Deposited	Precursor (ref.)	Composition (Atomic %)	Resistivity (ρ) (μΩ-cm)	Pure Metal (ρ) (μΩ-cm)
Aluminum	$(CH_3)_3NAlH_3$	Al%:Ga%:C%:N% -	900	2.74
Copper	$C_{10}H_{13}CuF_6O_2Si$	Cu%:C% 50-80:20-50	50-150	1.67
Gold	$C_7H_7F_6O_2Au$	Au%:C%:Ga% 50:35:15	500-1500	2.44
Platinum	$C_9H_{17}Pt$	Pt%:C%:Ga%:O 24-45:24-55:19-28:2-3	70-700	10.4
Tungsten	$W(CO)_6$	W%:C%:Ga%:O% 75:10:10:5	150-225	5.3

Table 1-1: Composition and resistivity of various II-CVD metal films.

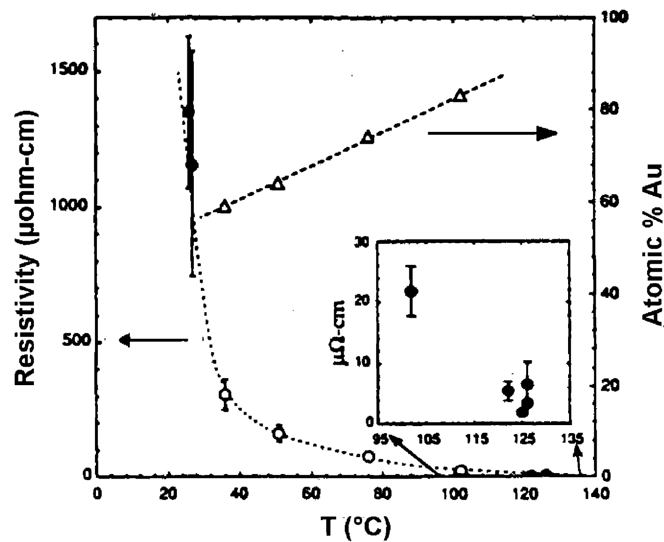

Figure 1.5: Resistivity and composition versus temperature FIB II-CVD films deposited from DMGhfac. From [8].

Research at MIT turned towards improving the process by solving the impurity incorporation problem. Substrate heating yielded significant improvement in film purity and resistivity.[8] Figure 1.5 shows the effect of temperature on composition and resistivity. The temperature dependence was attributed to enhanced organic byproduct desorption; in other words, organic byproducts from the decomposed metalorganic precursor have a higher probability of escaping instead of being deposited as carbon.

Substrate heating appears to be a practical solution, but it poses two serious problems. Higher substrate temperatures lead to slow but finite thermal CVD outside the ion irradiated zone. Moreover, positional accuracy is compromised by thermal drift. The IBM chip repair process illustrates the importance of maintaining positional accuracy: the FIB system (Micrion 9800) has a laser-interferometer controlled stage with a rated accuracy of $\pm$ 0.25 μm. It interfaces to a computer running Knights Technology's Merlin Maskview so that the operator can input layout modifications as a dataset. This allows blind navigation and a semi-automated FIB repair process.[3] Clearly substrate heating is not a satisfactory solution.

1.4 Physical Model

The early work on II-CVD was primarily empirical. Random experimentation with various organometallic gas precursors was not going to divulge the fundamental mechanisms of Ion-Induced CVD. Andrew Dubner at MIT conducted the first fundamental research on II-CVD. [9,10,11] He focused on the physics of the deposition process. This understanding of the physical mechanism of II-CVD serves as an important stepping-stone on the road to understanding the kinetics and microstructure evolution of II-CVD.

Note that Dubner was the first person to use broad ion beams in his research: a broad beam deposited a blanket film and the instantaneous growth rate was monitored using a quartz crystal microbalance. This allowed vastly improved monitoring of the depostion conditions as compared to a focused ion beam (FIB) process. Broad beam deposition was also employed in the research that is presented here. (See Chapter 2.)

Dubner described the II-CVD process as competition between deposition and sputtering. The incident ion beam causes both deposition through precursor decomposition and material removal through sputtering. Thus, an expression for net deposition yield (Y_{net}) in terms of the number of deposited atoms per incident ion:

$$Y_{net} = Y_d - Y_s \quad [1.1]$$

Y_d is the number of decomposed precursor molecules per ion and Y_s is the number of sputtered atoms per ion. Y_d is a function of adsorbed precursor coverage (Θ) and the ion decomposition cross section (Ω_d):

$$Y_d = \Theta\Omega_d$$

Θ is a function of the precursor flux, the substrate temperature and physical or chemical interaction between the precursor and substrate. Ω_d is a function of the ion mass, ion energy and the ion/substrate interaction.

Dubner sought to isolate the physical mechanism by focusing on this ion/substrate interaction and the energy transfer mechanism. An incident energetic ion transfers its energy to the substrate through nuclear stopping (S_n) and electronic stopping (S_e) collisions. The elastic nuclear collisions result in displacements of substrate atoms, which undergo further collisions if sufficient energy is transferred. This progression of branched atomic displacements is

known as a *collision cascade*. Random events in the cascade redirect atoms back towards the surface. If a collision with the surface imparts more than the surface binding energy, the excited surface atom (ESA) is ejected. However, this does not happen if the surface is covered with adsorbed organometallic precursor. Instead, the ESA imparts energy to decompose the adsorbed organometallic molecule and deposits metal and, unfortunately, carbonaceous impurity.

Dubner examined deposition of gold from $C_7H_7F_60_2$ (DMG(hfac)) using the full range of noble gas ions. The results show that Y_d scales with nuclear stopping power. Furthermore, he measured decomposition yields that were as high as 20. This precludes direct collisions with adsorbed molecules as the governing mechanism. This evidence suggests that the energy transfer is analogous to sputtering where the process is *substrate mediated* through a collision cascade.

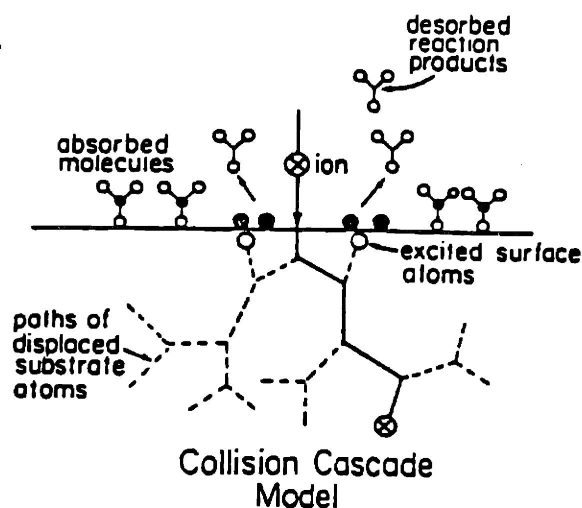

Figure 1.6: Schematic of the Collision Cascade Model. Impinging ions initiate a cascade of displaced surface atoms, which then produces excited surface atoms that decompose adsorbed precursor molecules. From [9].

Figure 1.6 illustrates the collision cascade model of II-CVD. Sputtering was simulated by the TRIM-TC software package. Here, surface binding energy data were not readily available so the simulation used the heat of sublimation as the threshold for ejection of an ESA. For II-CVD the activation energy threshold for adsorbed gas precursor decomposition replaced the heat of sublimation. The simulated collision cascade model agrees with experimental data.

Dubner also developed an alternate model for II-CVD – the thermal spike model. (Figure 1.7.) An instantaneous but short-lived thermal spike causes decomposition when an ion strikes the substrate. This model does not fit the data as well. Dubner's work led to the general acceptance of the collision cascade as the physical model for II-CVD.

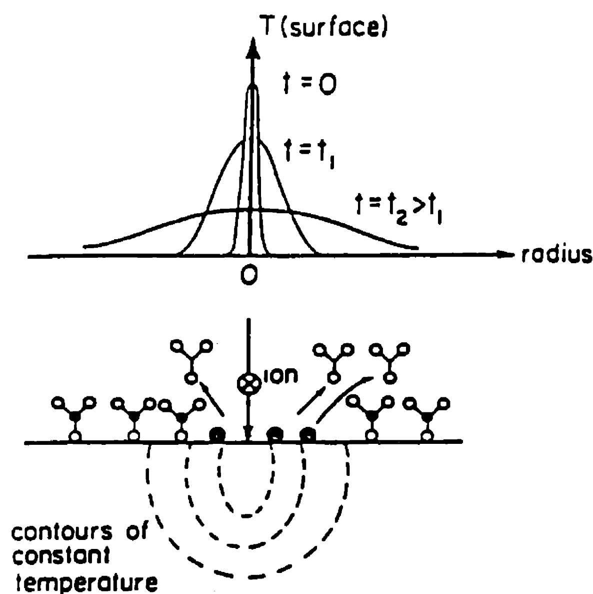

Figure 1.7: Thermal Spike Model. The impinging ion produces an instantaneous thermal spike that decomposes adsorbed precursor molecules.

1.5 Kinetic Model

Dubner had not addressed the kinetics of II-CVD or the associated carbon incorporation problem. Dubner's physical model laid the foundation but could not bring any insight into how this proposed physical mechanism produces a cellular growth mechanism. The next logical step is to understand the kinetics of II-CVD – a quantitative model would yield ratios of deposited metal and carbonaceous impurity. The microstructure model, which is presented in Chapter 4, integrates with this kinetic model. Essentially, the kinetic model provides the ratio of metal and carbon impurity that is being incorporated for given deposition conditions; the microstructure model then predicts how the microstructure evolves.

Chiang carried out a systematic study of II-CVD to develop a phenomenological surface kinetic model that accounts for adsorption (surface coverage); deposition of metal and impurity; byproduct desorption; and sputtering.[12] Chiang rewrote equation [1.1] in terms of rates and also included impurity incorporation :

$$r_{dep}^{net} = r_{dep}^{Cu} + r_{dep}^{C} - r_{rem}^{Cu} - r_{rem}^{C}$$

where the subscripts "*rem* "represent removal and "*dep*" deposition, respectively. He then determined adsorption, deposition and removal (sputtering) rate kinetics in terms of adjustable process parameters: precursor gas pressure, ion current density, substrate temperature, and ion energy. His deposition system also used a broad ion beam, which enabled direct rate measurements with a quartz crystal microbalance (QCM).

Chiang not only formulated a surface kinetic model but also developed relations based on experimental data to determine the kinetic rate coefficients. Figure 1.8 illustrates the fit of the kinetic model to experimental data. The graphs illustrate the two primary kinetic regimes:

- Abundant precursor flux (reported as a pressure) where the deposition rate is close to being linear with respect to ion flux.
- Low precursor flux where the growth rate reaches a maximum at some ion flux.

The kinetic model predictions match the experimental data accurately.

Chiang used the same organometallic gas precursor as in the work that is presented here – Cupraselect® (Cu^{I}(hfac)vtms)[13] precursor was used to deposit copper. (See Chapter 4 for information about the gas precursor.) The kinetic model predicts copper and carbon growth rates, and the ratio thereof translates into film composition. Figure 1.8 compares the kinetic model to composition data obtained by x-ray photolectron spectroscopy (XPS) quantitative analysis. The kinetic model does not predict film composition accurately at low ion fluxes. The source of this error stems from the calculation of one of the rate constants. This is discussed in detail in Chapter 4, which presents a modification to Chiang's surface kinetic model. *The modification to Chiang's model permits seamless integration between the surface kinetic model and the microstructure evolution model.*

An important difference between the physical model (Dubner) and the kinetic model is that the latter accounts for the time averaged surface coverage. As the ion flux increases, the gas precursor is consumed faster so that the average surface coverage is reduced. This leads to an associated increase in sputtering. Chiang not only monitored this surface coverage but also determined the surface species using laser-induced thermal desorption (LITD) where short duration laser pulses rapidly heat the surface to vaporize adsorbed gas molecules. LITD allows real time measurements of the surface chemistry during adsorption and deposition. This technique is much more powerful than the more common temperature programmed desorption (TPD) where the surface is heated

macroscopically at a much slower rate and it is impossible to monitor real time deposition.

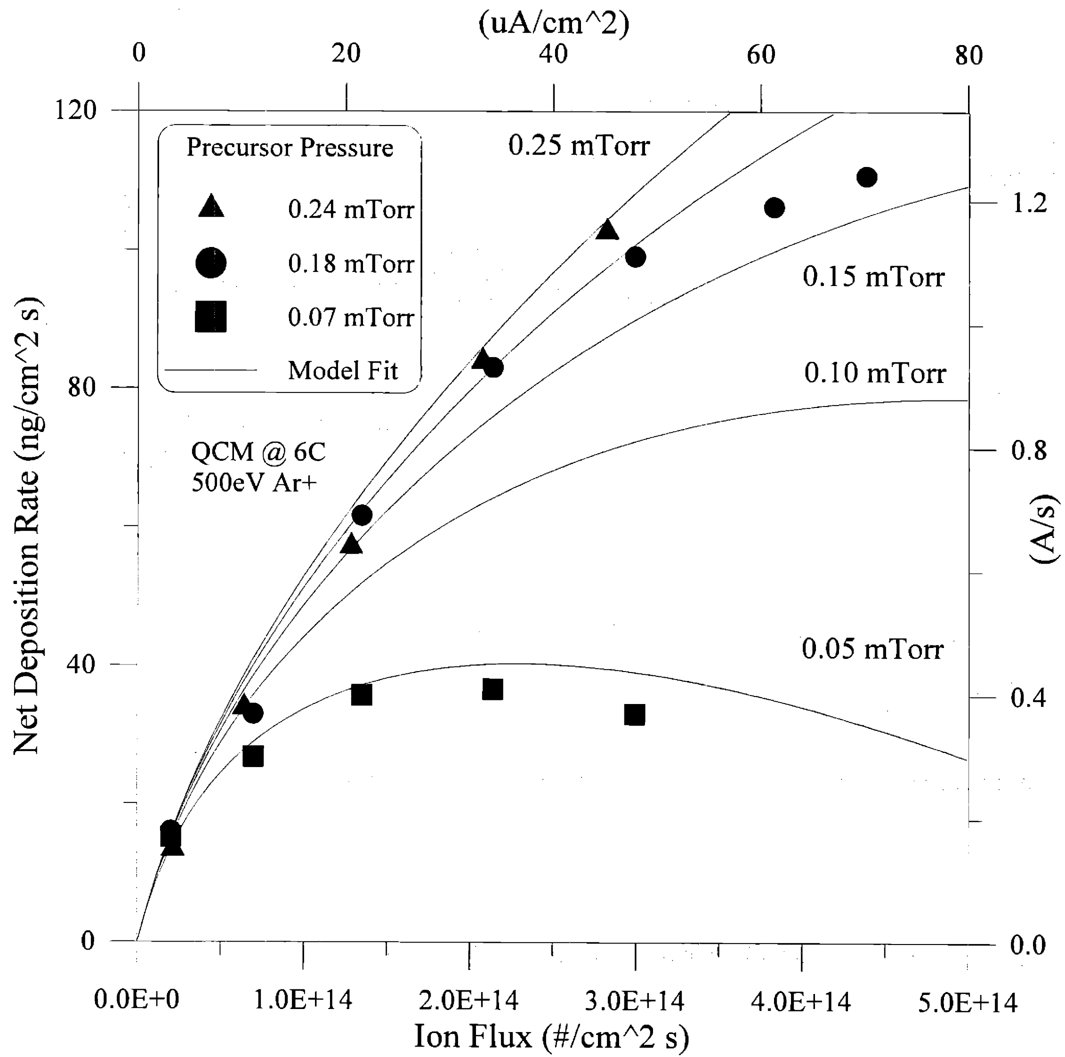

Figure 1.8: Growth rate vs. ion flux: comparison of Chiang's kinetic model to experimental data. From [12].

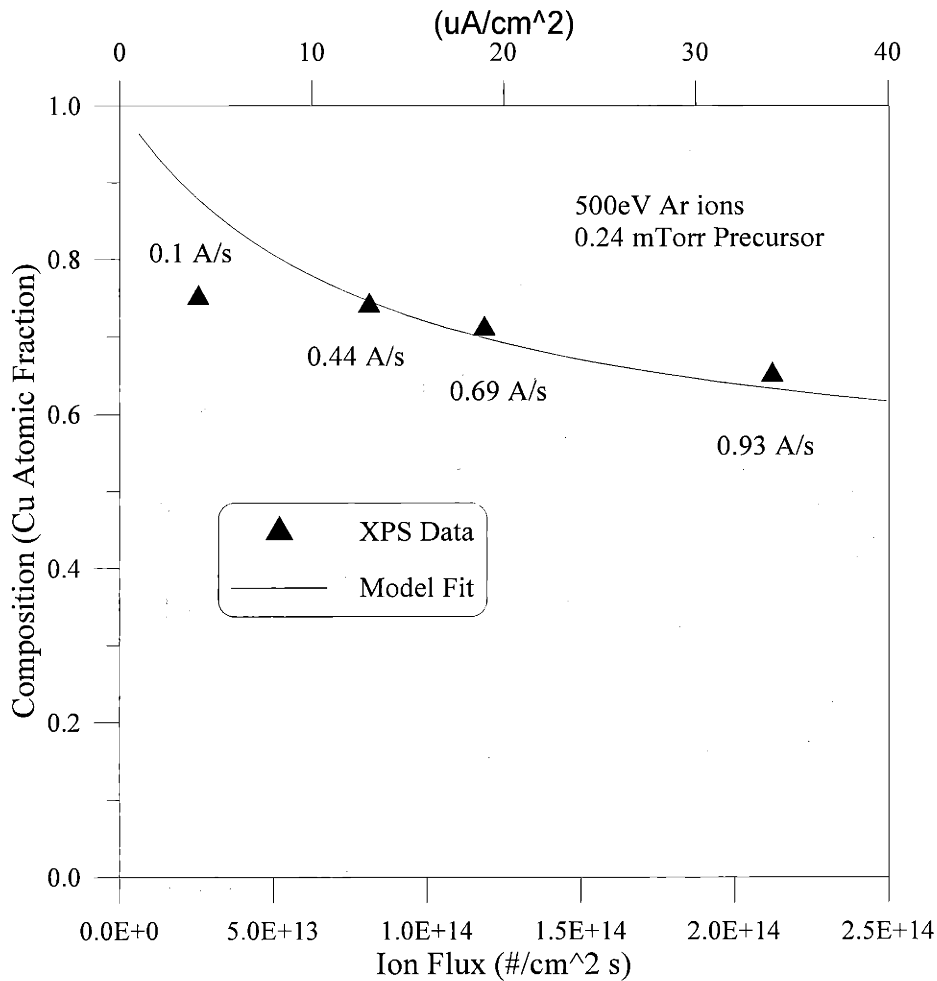

Figure 1.9: Surface kinetic model fit to XPS data for composition vs. ion flux. The model does not predict composition accurately at low growth rates. From [12].

Although the instantaneous vaporization of LITD prevents complete decomposition of the surface species, there is still some cracking of the molecules and the technique involves identification of "tag" species. With reference to thermal CVD of copper, CCO was identified as an intermediate leading to carbon deposition.[14] The tag species for CCO is CO, while Cu(Hfac) is identified by CF_3 and HCCO. Figure 1.10 shows a comparison of the surface kinetic model to the LITD data. Clearly, the kinetic model predicts trends that are substantiated by the LITD data.

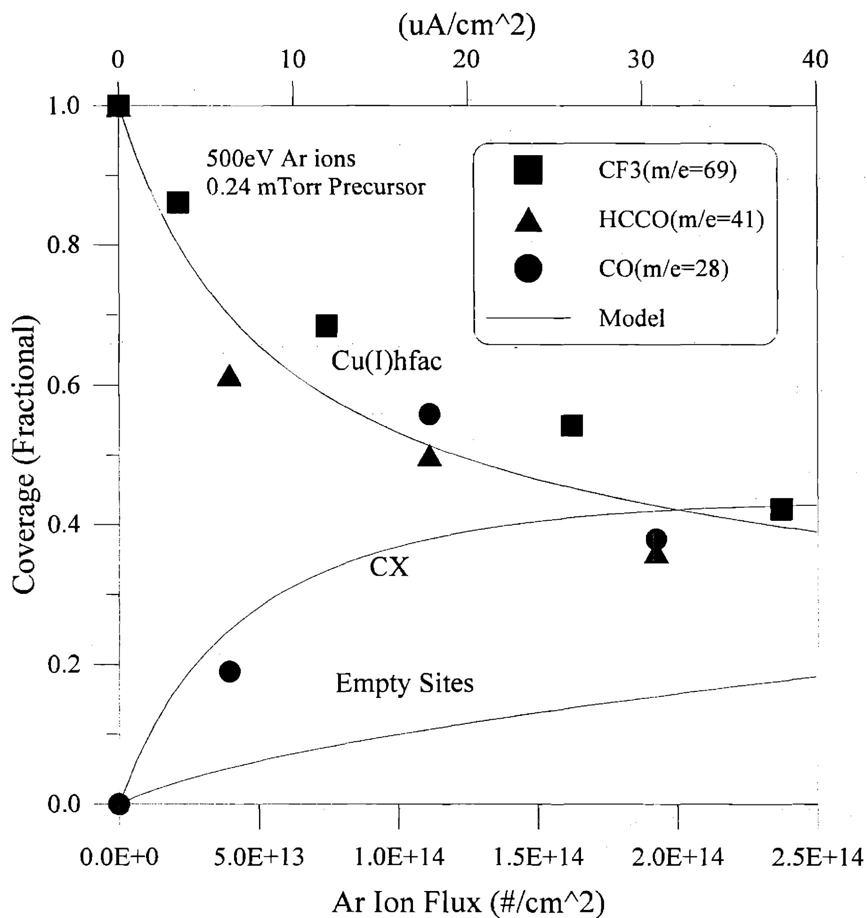

Figure 1.10: LITD coverage data compared to surface kinetic model. Note the increase of empty sites and carbon intermediate (labeled CX with CO as "tag" species) as the ion flux increases. From [12].

1.6 Removal of Carbon Impurity by Hydrogen Atom Beam

The kinetic model verified the qualitative assumptions regarding organic byproduct removal. Having established that substrate heating is not a

satisfactory solution, an alternate method would involve adding a reactant that

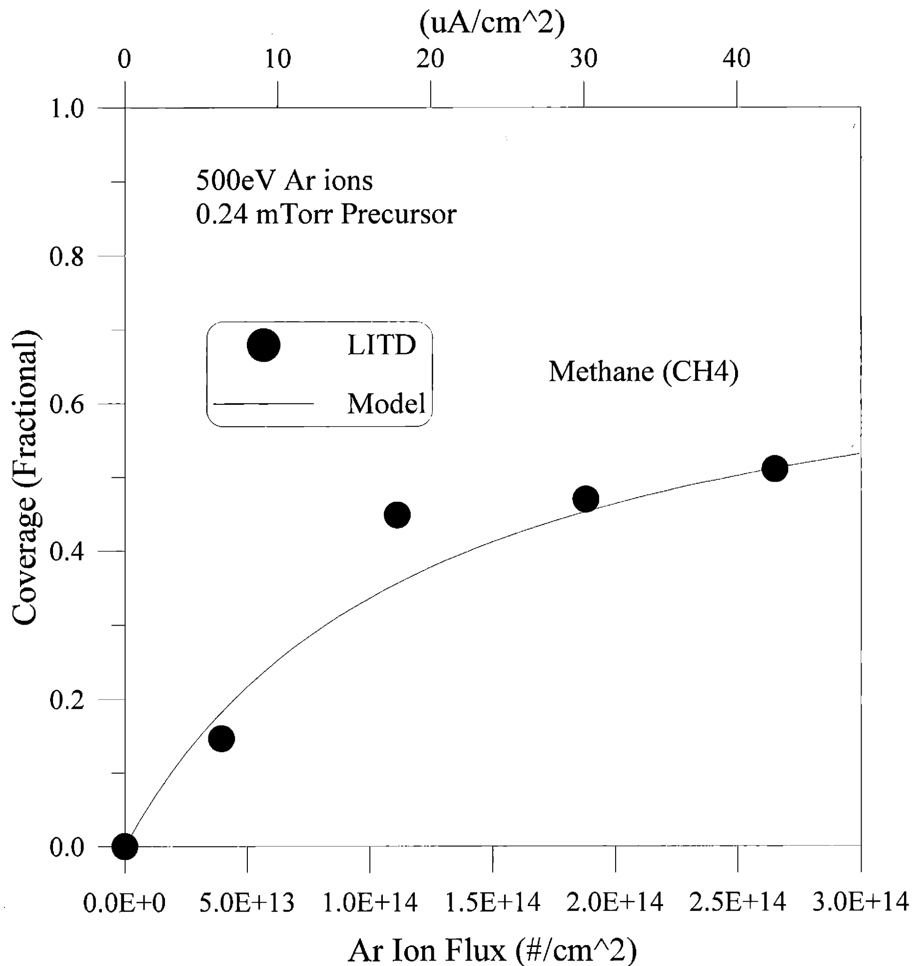

Figure 1.11: Fit of kinetic model to LITD data. From [12].

removes carbon. Hydrogen is added as a reactant with $Cu^{II}(hfac)_2$ – similar chemistry to Cupraselect® – in thermal CVD in order to produce volatile hydrocarbon byproducts and help prevent carbon deposition. However, the reactivity of diatomic hydrogen is much lower than atomic hydrogen. The Materials Etching Technology Laboratory (METL) at MIT offered an excellent opportunity to investigate carbon removal with atomic hydrogen: G. Zau developed a coaxial waveguide microwave cavity atom source for chlorine atom

beam etching experiments.[15] This design overcomes the inherent recombination losses in having to transport an atom beam into a vacuum system. Chapter 2 describes the operation of the hydrogen atom source in detail.

From a kinetic perspective, Chiang found that the H atom beam removes carbon in an ion enhanced etching process and he incorporated this effect into his kinetic model. The hydrogen atoms react with carbon to form CH_X products – primarily methane (CH_4). Figure 1.11 shows an excellent fit of the kinetic model to LITD data. The H atom assisted II-CVD also has a marked effect on the microstructure: the H atom beam prevents the cellular growth process as it completely removes the carbonaceous impurity – to the extent of the detection capability of XPS. However, deposition at high temperature (e.g. 100°C), which yields less than an atomic percent of carbon, retains the cellular growth mechanism of Figure 1.2.

1.7 Microstructure

Although this work represents the first comprehensive examination of microstructure evolution with a view to understand and model the process, J.S. Ro performed an earlier investigation of microstructure evolution.[16] A contemporary of Dubner, he conducted the first microstructure analysis of II-CVD. Gold films were deposited from DMG(hfac) using a high energy (up to 70 keV) implanter with a 3 mm aperture. Ro also prepared the first cross-sectional transmission electron microscopy (XTEM) samples of II-CVD thin films. The microstructure was columnar, but not continuous through the cross-section and the columnar diameter shows some thickness variation. (Figure 1.12.) Contrast this with the uniform, continuous columnar microstructure of copper II-CVD films. (Figure 1.2.) Unlike Ro's work, the cross-sectional microscopy presented here provides ample supporting evidence for a *cellular* growth mechanism.

Ro also demonstrated that columnar microstructure does not develop at high carbon fractions (~50 %). The copper II-CVD system attains higher levels of metal fraction and therefore preserves the columnar microstructure for a wider range of deposition conditions. In fact, virtually all of the deposition conditions examined in the course of this work produced a columnar microstructure. At high levels of impurity the predicted column diameter is so small that capillarity prevents the cellular growth mechanism from proceeding. (See Chapter 4.)

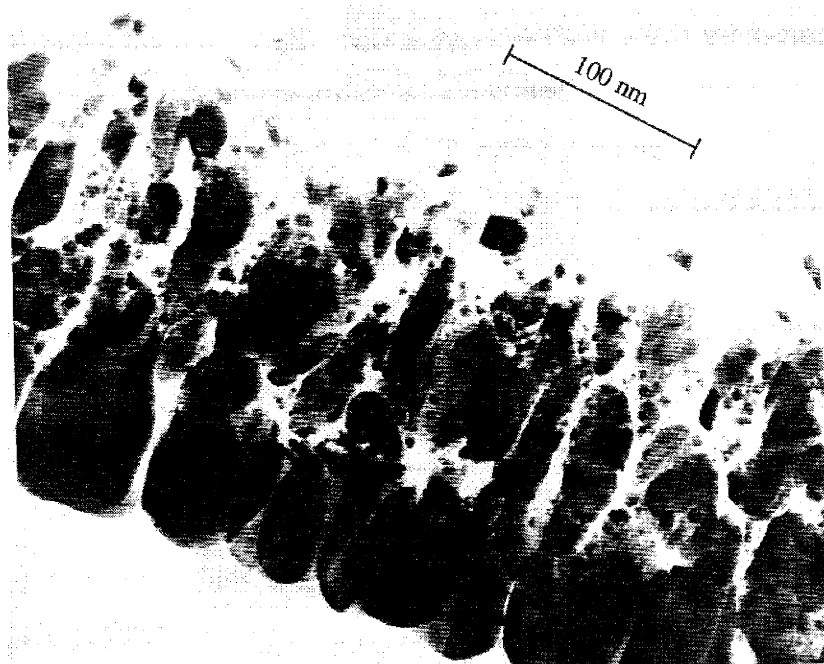

Figure 1.12: XTEM (cross-sectional transmission electron micrograph) of gold II-CVD film deposited by 50 keV Si+ ions. Contrast with microstructure in Figure 1.2. From [16].

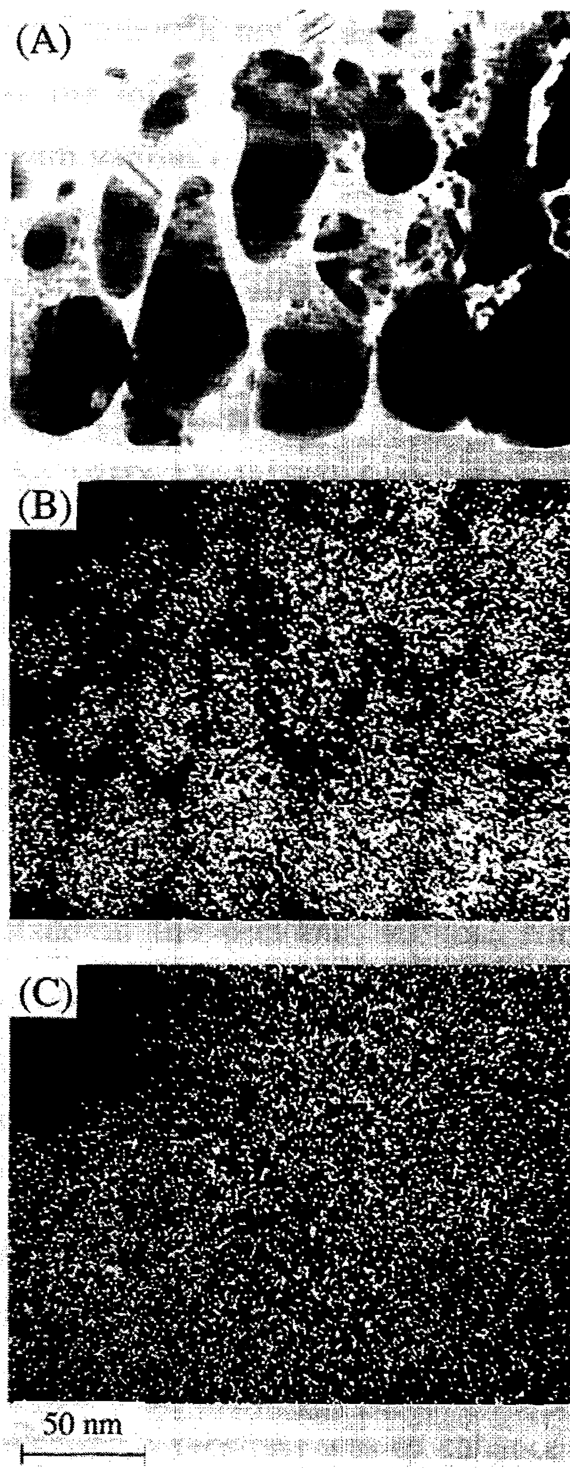

Figure 1.13: (A): STEM image of gold II-CVD film in cross-section. (B): corresponding EDS map of gold. (C): corresponding EDS map of carbon. Note that the carbon EDS map does not convey any information as carbon will appear on any surface that is exposed to the environment. The gold EDS map follows the outline of the STEM image. From [16].

Ro also investigated the distribution of gold and carbon vis-à-vis the microstructure by using energy dispersive x-ray spectroscopy (EDS) scanning transmission electron microscopy (STEM). Figure 1.13 shows EDS maps for gold

and carbon compared to a TEM image. Note that the carbon EDS map does not reveal any useful information because a sample becomes contaminated with organic matter after being exposed to the environment. Nevertheless, he concluded that the microstructure is essentially perfectly segregated with gold columns surrounded by a carbon matrix. This work will show that this is an over-simplification, which is only approximately accurate for certain high growth rate deposition conditions. Close examination of Ro's gold EDS map reveals intercolumnar peaks, which suggests that there is metal (gold) between the columns. The data presented in Chapter 3 will show that very low growth rate conditions lead to significant concentrations of metal outside the columns. The microstructure model will have to require that the matrix can incorporate relatively high fractions of metal since the column diameter is independent of the growth rate (and film purity) at constant temperature.

1.8 Objectives

The primary objectives of this thesis:

- To present a systematic and thorough investigation of microstructure evolution in ion-induced CVD (II-CVD).

- To develop a comprehensive model of the process, which is designed to interface with Chiang's kinetic model.

To achieve the latter, the thesis presents an extension to Chiang's kinetic model. (See Chapter 4.) The nature of the microstructure – columnar or "cellular" structures – brings the study into the realm of morphological instability and growth via cellular segregation.

Cellular growth must be approached in two ways. The first identifies a physical basis for cellular growth in II-CVD. Here, analysis of the microstructure will provide evidence for morphological instability as opposed to classical nucleation and growth. In other words, it is not sufficient to simply postulate cellular growth.

The second aspect involves the mechanics of the growth process in relation to cellular segregation. Morphological instabilities are often diffusion-controlled phenomena. II-CVD is a low temperature film growth process, which permits one to postulate that surface diffusion is the governing process – bulk diffusion is negligible at these temperatures. Thus, the microstructure model hinges upon surface diffusion, which is a function of temperature and ion bombardment. This model is then tested by data derived from II-CVD experiments at varying temperatures and ion beam fluxes. It turns out that it successfully predicts the observed microstructure – the key characteristic is that that the column diameter does not vary with growth rate even though the purity (fraction of copper) is a strong function of the same.

The hydrogen atom beam solves the main practical drawback of II-CVD, inasmuch as it enables deposition of pure copper films at room temperature. The carbon removal mechanism is an aspect of rate kinetics; therefore, Chiang's thesis covered it in much more detail. Columnar growth requires residual impurity so the virtually pure H atom assisted films exhibit equiaxed morphology as expected. Multi-layer samples were examined by XTEM (cross-sectional transmission electron microscopy) and the transitions between different growth conditions are indicative of the cellular growth mechanism. The sharp transition from equiaxed H-atom assisted microstructure to columnar microstructure strongly suggests that the growth mechanism is cellular.

The fundamental accomplishment of this thesis is to bring forth the final component of II-CVD, microstructure evolution, which builds upon Dubner's physical model and Chiang's surface kinetic model. This trio of models provides

a foundation of solid scientific understanding for future researchers who seek to develop II-CVD.

Finally, the thesis touches upon a novel application of II-CVD – to produce nanocellular structures for applications such as magnetic media. The combined understanding of rate kinetics and microstructure evolution allows researchers to develop candidate gas precursors and select optimum process conditions.

Chapter 2: Experimental Hardware and Analytical Techniques

This chapter describes the equipment and analytical measurement techniques used for the experiments in this thesis. This spans details of the II-CVD process as well as ex situ microscopy and analysis of the deposited films. For more information on materials characterization techniques the reader should consult reference [17].

2.1 Multibeam Vacuum Chamber

The "multibeam" vacuum chamber was custom designed and manufactured for the II-CVD process. T.P. Chiang and the author designed the vacuum chamber; we also specified and acquired all of the hardware and components that were added to the vacuum chamber. The chamber was manufactured by Sharon Vacuum Company according to our specifications.[18] The fundamental principle of the design allows three "beam" sources to impinge simultaneously: the gas precursor, the broad ion beam and a "reactive" beam such as a hydrogen atom source. A quartz crystal microbalance (QCM) monitored the instantaneous deposition or sputtering rate. Upon retracting the QCM, a pitot tube/ capacitance manometer and ion probe monitored the local precursor gas flux and the ion flux, respectively. This system offered more flexibility than the commercial FIB system (FEI FIB 500D) that was also available in our laboratories.[19] This commercial system lacked Conflat® ports that are necessary for retrofitting components such as the QCM or an H-atom source. Furthermore, the broad ion beam of the multibeam chamber produced "blanket" films covering up to a square centimeter, which simplified microscopy and compositional analysis. "Film" deposition by a FIB requires prolonged rastering of a substrate, which may still only cover a surface area of 0.01 mm^2.

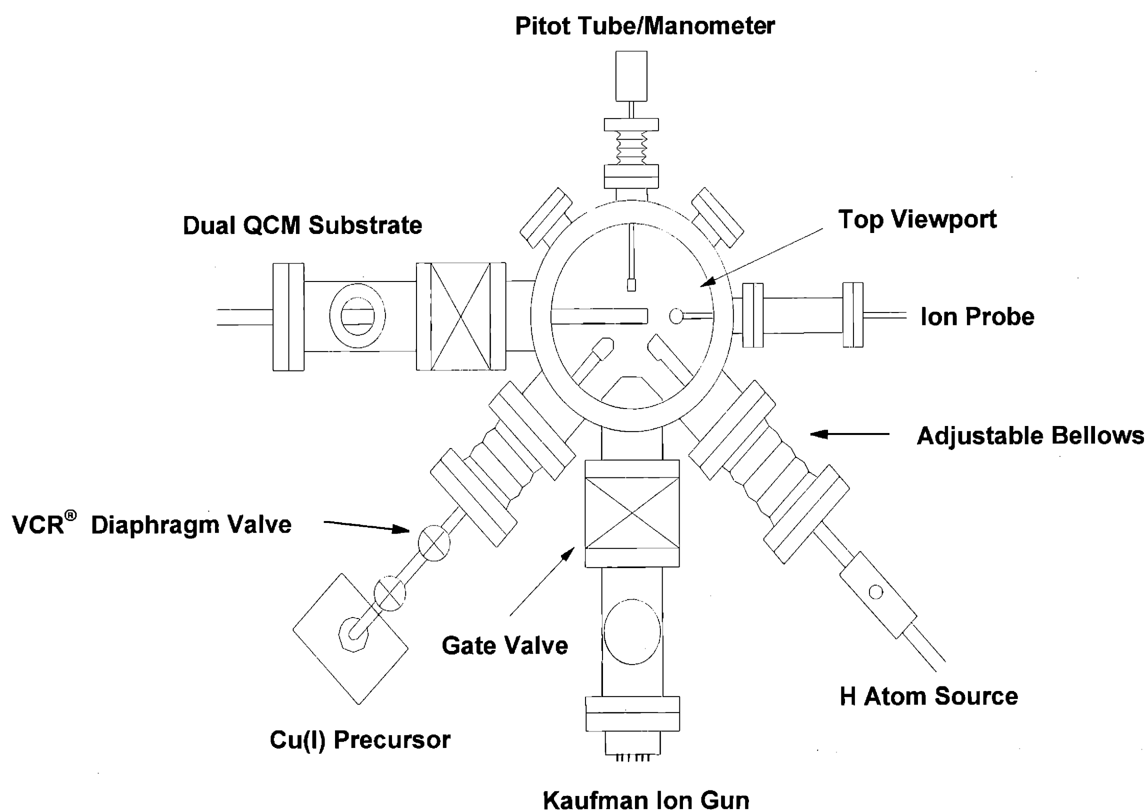

Figure 2.1: The multibeam vacuum system in plan view. A 4000 liter/second CTI-8 cryogenic pump evacuated the main chamber while a 220 liter/second Leybold turbomolecular pump evacuated the Kaufman ion gun.

A CTI-8 4000 liter/second (rated for water vapor) cryogenic pump evacuated the main chamber, which was a 14 inch high stainless cylinder with 10 inch internal diameter.[20] The cryogenic pump was mounted directly below the main chamber to achieve maximum conductance. The base pressure of the system was in the 1 to $2x10^{-8}$ torr range and the system was pumped down as low as $8x10^{-9}$ torr. All experiments were conducted only after achieving base pressure of at least $4x10^{-8}$ torr. A Bayard-Alpert ionization gauge with a thoriated iridium filament monitored the chamber pressure. The hot filament of the gauge slowly coated the glass surface of the gauge with copper due to pyrolysis of trace precursor gas molecules that made their way into the gauge tube. This pyrolysis slowly

through a 1 cm diameter stainless steel collimating cap, which mounted at the chamber inlet. A 220 liter/ second Leybold turbomolecular pump provided differential pumping of the ion gun chamber where Argon entered as a source gas.[21] The B-A gauge reported a typical main chamber pressure of $8x10^{-6}$ torr (not true pressure as discussed above) when the ion gun was operating, and the pressure measured at the ion gun chamber was in the mid 10^{-4} torr range.

2.2 Quartz Crystal Microbalance (QCM) Assembly

The Sycon Instruments QCM assembly served as the sample holder for all experiments.[22] The QCM sample holder was welded onto a half-inch (outer diameter) stainless steel rod that enclosed 3/16" water lines; circulating water maintained the substrate at a fixed temperature. A Cole-Palmer water circulator set the water temperature to better than ±0.5°C accuracy. The unit had both refrigeration and heating capabilities, and optimum setpoints near room temperature often involved balancing heating and cooling. Addition of ethylene glycol extended the possible temperature range: the highest fluid temperature used in these experiments was 125°C. A K-type thermocouple monitored the temperature in the QCM holder. It was attached to the stainless steel back of the QCM holder with vacuum compatible high thermal conductivity cement (Omegabond®). Figure 2.3 illustrates the construction of the feedthrough. Two butt-welded Cajon Ultra-Torr® compression fittings (Viton® O-rings) hold vacuum. The dual construction was a precaution in case the inner fitting leaked. A connection allowed differential pumping of the space between the two fittings.

The quartz crystals were gold coated and "AT-cut" so that the approximate resonant frequency was 6 MHz. They snapped onto the sample body with a stainless steel lock-ring that engaged with the aid of a copper leaf spring in the base of the unit. The lock-ring exposed an 8 mm diameter of a mounted crystal.

degraded the filament. It was possible to turn off the gauge during deposition but it served as a good reference and check on the gas load introduced by the beam sources. Note that a Bayard-Alpert (B-A) gauge is calibrated for nitrogen so any measurement with a beam source turned on was not an accurate measurement of system pressure, but only served as a relative yardstick.

Figure 2.1 shows four 4 5/8" ports and four 2 3/4" ports that are on the same mid-plane of the chamber. Two additional 2 3/4" ports with quartz windows make a 40 degree angle with the horizontal plane. Chiang used these ports for his laser-induced thermal desorption (LITD) experiments.[12] The four 4 5/8" ports were offset by 45 degrees so that the three beam sources could target the same spot simultaneously. Diagnostic tools and the B-A ion gauge mounted on the 2 3/4" ports. A quartz glass viewport on the top of the chamber permitted alignment of the beams and QCM substrate holder.

A load-lock allowed keeping the main chamber evacuated while removing the QCM assembly. This increased throughput significantly. It was not a "true" load-lock inasmuch as it was not isolated from the main chamber after the sample had been reintroduced. The load-lock was a four-way Conflat® cross with two 4 5/8" ports and two 2 3/4" ports and a gate valve isolated if from the main chamber after retraction of the QCM rod. A 2 3/4" viewport aided the operator in verifying that the QCM had been retracted far enough prior to closing the gate valve. The outer 4 5/8" port had a feedthrough for the QCM rod, which unbolted from the load-lock chamber for sample replacement or maintenance. A mechanical roughing pump evacuated the load-lock through a 2 3/4" port. This port also enabled initial rough pumping of the main chamber from atmospheric pressure.

The ion beam source mounted onto a similar 4 5/8"/ 2 3/4" four-way cross. A gate valve isolated the ion gun from the main chamber when the operator had to replace the cathode filament of the ion gun. The ion beam entered the chamber

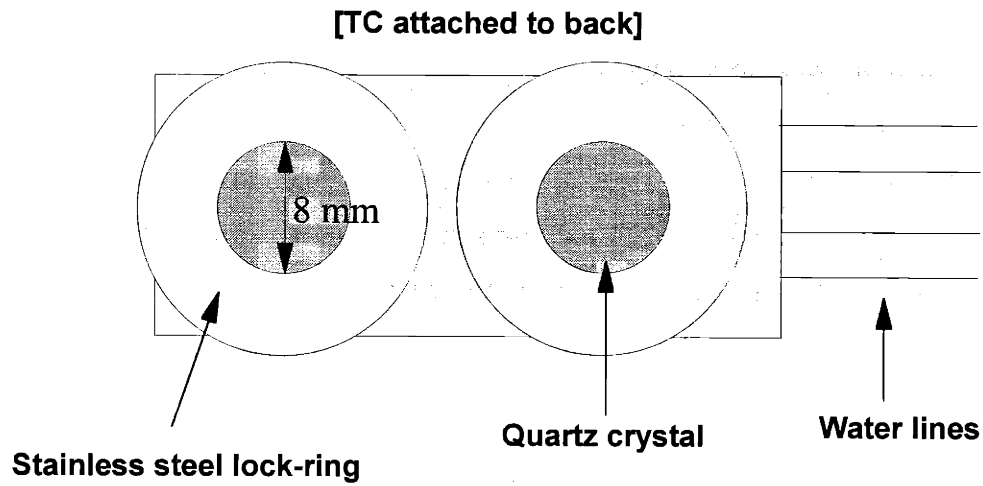

Figure 2.2: QCM sample holder.

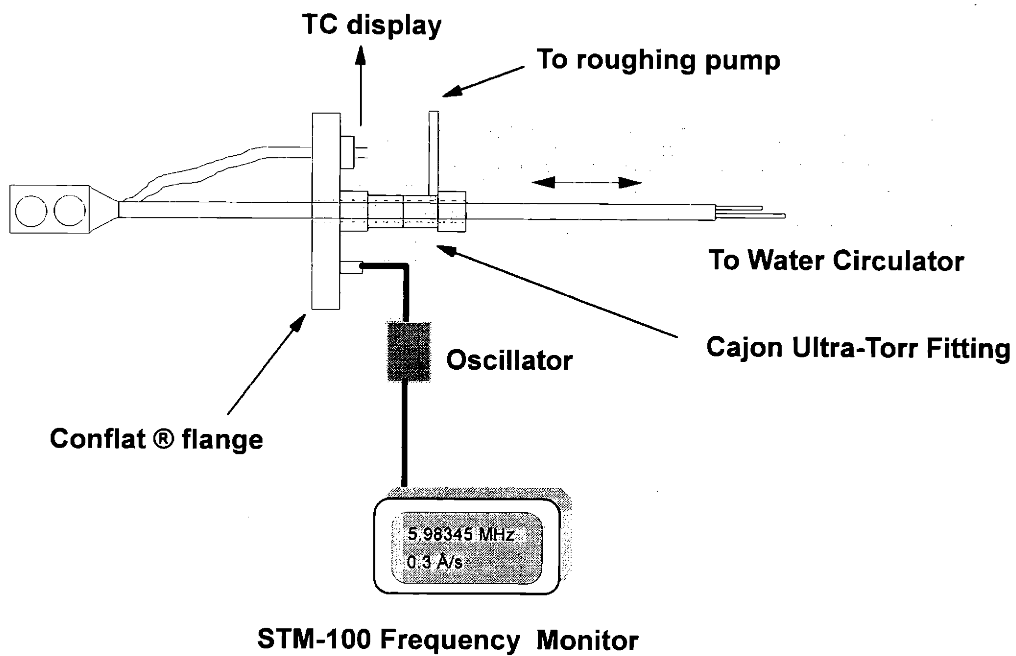

Figure 2.3: QCM feedthrough assembly.

The quartz crystal oscillation is due to the piezoelectric effect. A piezoelectric crystal has a linear relation between an applied electric field and a resulting strain; thus, an applied voltage causes a proportional deformation. Furthermore, specially cut crystals have resonant frequencies. The resonant frequency changes linearly with addition or removal of small amounts of material from the face of the crystal. Consequently, monitoring the resonant frequency of the crystal allows rate measurement of film growth or sputtering. The ratio of areal mass densities (m_f/m_q) is expressed as,

$$\frac{m_f}{m_q} = \frac{\rho_f t_f}{\rho_q t_q} = \frac{(f_q - f_c)}{f_q} \qquad [\,2.1\,]$$

where the subscript (f) denotes a coated crystal while the subscript (q) denotes uncoated quartz. f_c and f_q are frequencies in Hz for coated and uncoated crystals, respectively. The areal mass densities are equal to the product of thickness (t) and density (ρ). Rearranging the equation yields:

$$t_f = \frac{(f_q - f_c) N_q \rho_q}{f_q^2 \rho_f} \qquad [\,2.2\,]$$

where N_q is the product of f_q and t_q, which equals 166.1 kHz·cm for an "AT-cut" quartz crystal. Note that the quartz crystals are pre-coated with gold so the f_q term in the numerator is effectively replaced by an initial frequency measurement. For small changes the expression remains valid after making this substitution. However, the linear relationship expressed in equation [2.1] is not valid for ratios exceeding 0.02. The equation breaks down at approximately 1.5 μm for pure copper films, which is an order of magnitude thicker than any films that were grown for rate measurements in this work.

An oscillator applied the voltage that creates resonance in a quartz crystal. A coupled Sycon Instruments frequency monitor (STM-100) measured the frequency and converted it to an equivalent rate based on pre-programmed data for the deposited film. The frequency-to-rate conversions assume deposition of pure copper even though II-CVD co-deposits carbon impurity. This does not introduce significant error because even relatively impure films contain a predominant weight fraction of copper; e.g., ~20 atomic % carbon films are 93% copper by weight. The data was also sent to a PC via an Iotech IEEE-488 bus.

The Sycon rate monitor measured frequency at a resolution of 1 Hz. Substituting values for density in equation [2.2] yields 0.137 Å/Hz for copper. This provided excellent resolution for both very low deposition rates and adsorption experiments, as long as the frequency measurement did not drift. Temperature induced drift complicates QCM measurements. This led to the selection of a dual QCM assembly where one QCM would monitor any drift over the course of an experiment. However, this proved to be unnecessary because the QCM was remarkably stable: leaving the system overnight at constant temperature only produced a change in frequency of one or two Hz.

On the other hand, the selection of a dual QCM turned out to be invaluable: microscopy samples were attached to one QCM – thus disabling thickness measurement – while the other monitored the growth rate before and after the run. The following delineates the steps involved in an experiment:

- Turn on ion gun, gas source and establish stable deposition conditions at desired temperature and growth rate. QCM measures growth rate.
- Retract QCM. Shut off gas source. Position ion probe and measure ion flux.
- Retract ion probe. Block ion flux with flag. Turn on gas source.
- Reposition and carefully align QCM holder, this time with microscopy sample in position.
- Remove flag from ion source and simultaneously start STM-100 timer.

- Stop run by moving working QCM into position. Measure growth rate.
- Shut off gas source. Position ion probe and measure ion flux.

2.3 Gas Precursor

This section focuses on the delivery of the gas precursor. Refer to Chapter 4 for information about the chemistry of Copper(I)hexafluoroacetylacetonate-vinyltrimetylsilane (Cu(I)hfacVTMS), a.k.a. Cupraselect®.[23]

Gas delivery in II-CVD differs markedly from thermal CVD: in II-CVD the gas load must be minimized in order to prevent gas phase collisions and scattering of the ion beam. Thermal CVD of copper from Cu(I)hfacVTMS typically uses an inert carrier gas bubbler arrangement at 10 torr and a system pressure on the order of 100 mtorr.[24] The system pressure in II-CVD is four orders of magnitude lower at approximately 10^{-5} torr. However, sufficient gas must be delivered to the substrate; therefore, the gas delivery tubing extended to a position adjacent to the substrate. (See Figure 2.1.) We referred to this design as "local dosing".

Schumacher Co., the inventor and supplier of the gas precursor, stressed the importance of not overheating the gas container and delivery lines in order to avoid precursor decomposition, which initially involves dissociation of the stabilizing VTMS ligand. They recommended not heating delivery lines above 60°C or the gas source above 45°C. Exploratory experiments showed that relatively low temperatures supplied adequate gas for the II-CVD process, which led to fixed settings of 30.5°C and 40°C for the gas source and gas lines, respectively. It was important to maintain a positive temperature gradient from the gas source to the gas delivery lines. Otherwise one would get low, erratic gas flux and condensation in the lines, which would lead to very slow pump down after isolating the gas source.

The liquid Cu(I)hfacVTMS was enclosed in a stainless steel 50 ccm cylinder, which was immersed in a water bath at 30.5°C ± 0.5°C. A peristaltic pump circulated the water in the heated bath. As a safety precaution, a ventilated PMMA box enclosed the gas cylinder and water bath. The gas line was a half-inch OD stainless steel tube with a tapered 6061 aluminum cap, which was referred to as the "doser head". The doser head tapered at a 45 degree angle, which permitted it to be positioned as close as possible to the sample without blocking the ion beam. A Conflat® bellows flange adjusted the position of the tube. (See Figure 2.1 where the doser head is retracted.) A 0.08" inch doser head outlet provided beam collimation. The gas line inside the chamber was wrapped in a Kapton® insulated flexible heating strip, which was held in place by Viton® o-rings. A K-type thermocouple monitored the temperature of the gas line and a variac adjusted the current to fix the temperature at 40°C. The same variac supplied current in parallel to heating tape wrapped around the exterior part of the gas line.

A VCR® metal-seal diaphragm valve isolated the gas source from the main chamber. A downstream needle valve constricted gas flow and allowed fine-tuning of the gas flux. The gas pressure on the sample surface – equivalent to a localized gas flux – was measured by the pitot tube assembly. The pitot tube was a 3/8" stainless steel tube capped by a 6061 aluminum cap with a 0.020" inch orifice. The tube mounted on a Conflat® bellows flange, which allowed the pitot tube head to move into position adjacent to the doser. The opposite end connected to a MKS 390H capacitance manometer with "six decade" resolution.

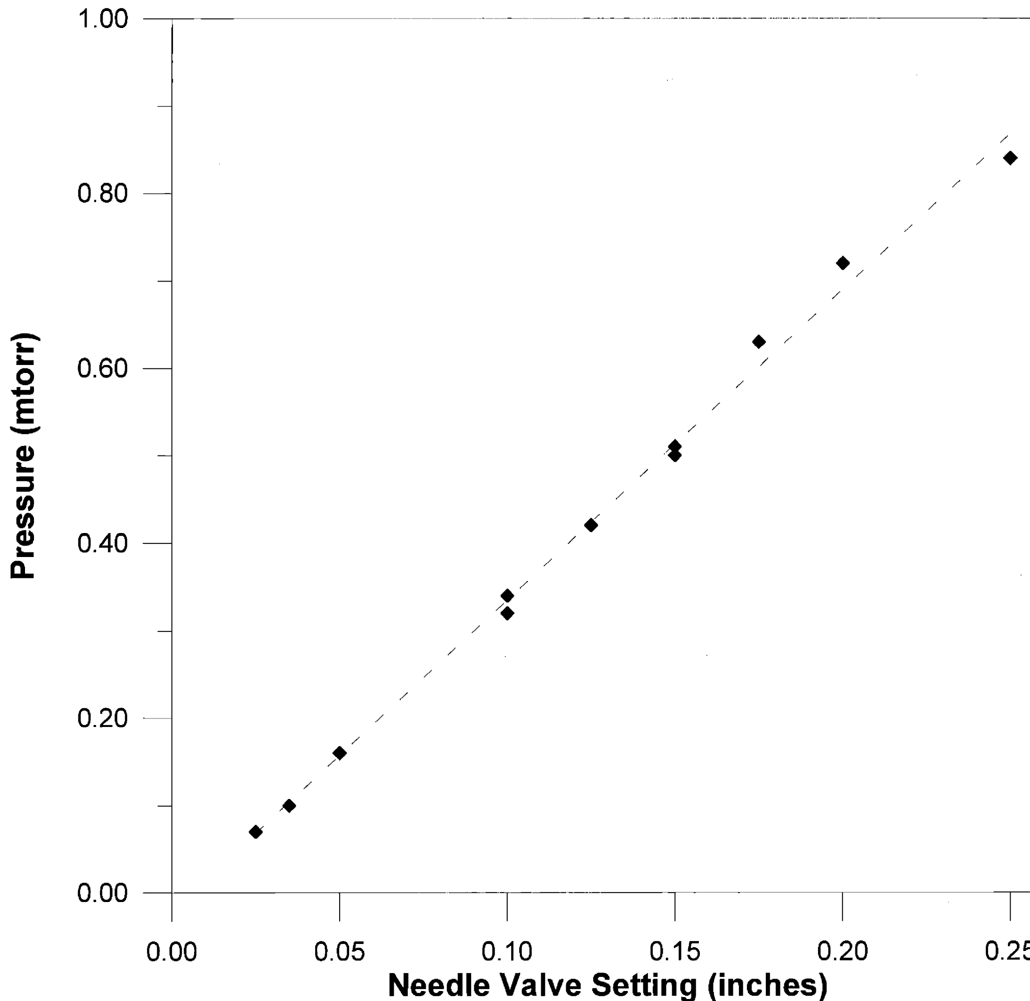

Figure 2.4: Local precursor pressure at sample surface versus needle valve setting. A capacitance manometer attached to a pitot tube assembly measured the pressure. The needle valve setting of 0.15 inches, corresponding to 0.5 mtorr, became the default setting.

(10^{-6} torr to 1 torr.) Before conducting a set of experiments, the pitot tube measurements calibrated the needle valve settings. Figure 2.4 shows the calibration after the gas source was replaced prior to the final set of microstructure experiments. Rate experiments showed that 0.5 mtorr sets the II-CVD process in the "ion-flux-limited regime", so 0.15" became the default needle valve setting for experiments presented in this thesis. (See Chapter 4 for information about process "regimes".)

2.4 Ion Gun

The broad-beam ion beam source was the most important piece of equipment on the apparatus. This thesis will show that ion beam flux (measured as current) is the critical parameter that influences the film growth process in II-CVD. Successful experiments hinged upon maintaining stable ion beam currents for extended periods of time. Whereas rate experiments only require stable beam currents for approximately one minute, a film grown for cross-sectional microanalysis requires deposition for up to several hours; therefore, it was critical that the beam flux was maintained within a reasonable range. The ion gun was a conventional 1 cm (beam diameter) compact Commonwealth Scientific[25] Kaufman gun mounted on a 4.625" flange. The gun was 12.2 cm long with a diameter of 4.5 cm. Unfortunately, maintaining stable ion beam currents with this ion gun was not a trivial task. This section presents the principles of operation and discusses reasons for the observed degradation of ion current over time.

The operation of a Kaufman gun relies on the introduction of an inert (usually) working gas – in this case, Argon. The ion gun was enclosed in a Conflat® 4.625" cross, which was evacuated by a 220 liter/second Leybold turbomolecular pump.[21] A mass flow controller set an Argon flow rate of approximately 2 sccm that entered the gun via a 1/16" stainless steel feed tube in order to establish a pressure in the mid 10^{-4} torr range. The optimum flow rate was determined empirically by measuring the ion beam current versus main chamber pressure. The current density reached a plateau at approximately 7×10^{-6} torr.

A wound tungsten filament served as the cathode, which mounted across two posts above a stainless steel anode. The manufacturer recommends a 0.005" diameter filament. However, cathode replacement was the most frequent maintenance requirement for the system, which involved bringing the ion gun chamber up to atmosphere and disassembling the gun. The filament eroded over

time, and the lifetime scaled approximately with its diameter. Kimball Physics supplied 0.010" tungsten springs, which were easily extended and made in to filaments.[26] If the springs were not over-extended then the resulting filament retained some tension, which resulted in low contact resistance with the mounting posts.

Powering the cathode in this type of ion gun leads to thermionic emission of energetic electrons that collide with and ionize the Argon molecules flowing into the discharge chamber. Some of these ions recombine with electrons at the discharge chamber surface, but others pass through holes in a screen grid to form multiple "beamlets". The ion beam is in fact the sum of these beamlets.

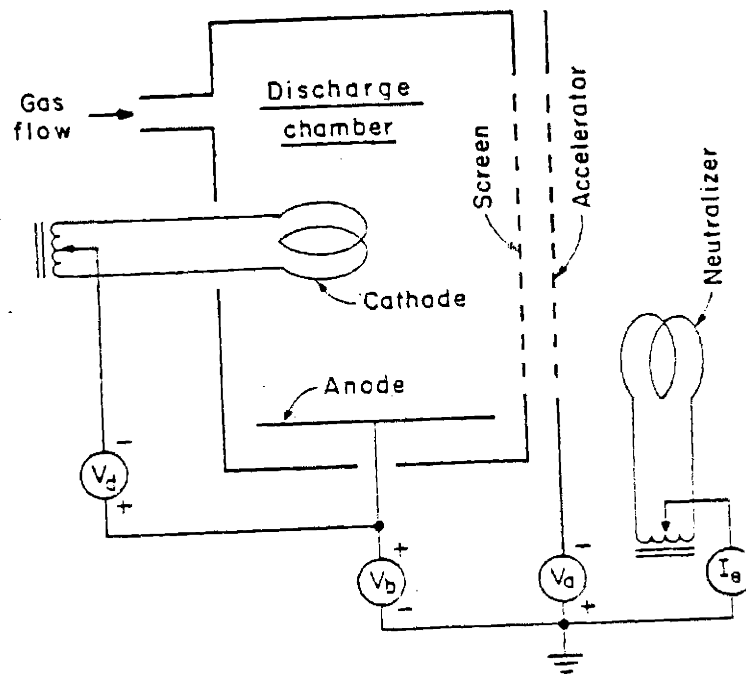

Figure 2.5: Schematic of Kaufman ion gun. The gun also has a magnet, which is typically mounted behind the anode. From [34].

A DC discharge voltage (V_d) of 40 V between cathode and anode creates plasma consisting of neutrals, ions, energetic electrons and low-energy

background electrons. The pressure in the discharge chamber (mid 10^{-4} torr range) was low enough so that the mean free path for a gas molecule was greater than the discharge chamber dimensions. Magnetically confining the plasma increases the ionization probability of an electron leaving the cathode rather than escaping to the anode. A permanent magnet was mounted behind the anode for this purpose. However, low-energy background (secondary) electrons diffuse across the magnetic field with ease and reach the anode. This completes the anode to cathode circuit. The power supply measures a corresponding discharge current (I_d). This current is an important parameter: to avoid over-heating the gun. I_d must be kept below 1 mA – preferably below 0.5 mA according to Commonwealth Scientific.

The V_d setting depends on two effects. Too low voltage produces a cathode space charge limit when electrons near the cathode prevent additional electrons from leaving the cathode and reaching the discharge plasma. Furthermore, Vd must be significantly larger than the first ionization potential for Argon (15.8 eV). On the other hand, a potential above 43.4 eV leads to formation of doubly charged Argon ions. The plasma is roughly equipotential with the anode so any ion that strikes the cathode falls through the full V_d potential – doubly charged ions gain twice the energy and many times the sputtering of yield a singly charged ion. This leads to contamination of the growing film through sputtering of the cathode surface; in this case, the tungsten filament and its stainless steel supports. Therefore, V_d was set at 40 V. In practice, striking the plasma discharge requires a higher discharge voltage so an ion gun power supply automatically applies a preset higher voltage until it detects a discharge current.

The beam voltage supply (V_b) connects the anode to ground; this sets the potential drop of the ion beam at the grounded substrate. As mentioned earlier, multiple beamlets pass through the first grid of the ion optics. The second grid – known as the accelerator grid – is electrically isolated from and perfectly aligned with the first grid. The accelerator grid is negatively biased (V_a) with respect to

ground and serves to extract and focus the ions. Under normal operating conditions the ion beam should not strike this grid. Ions that do strike the accelerator fall through the full potential of the beam voltage plus the accelerator voltage and cause significant sputter damage. Therefore, the ion grids are made out of graphite, which has a very low sputtering yield. Figure 2.6 shows the potential variation across the grids. The default V_a setting is 10% of V_b; our power supply automatically fixed this ratio.

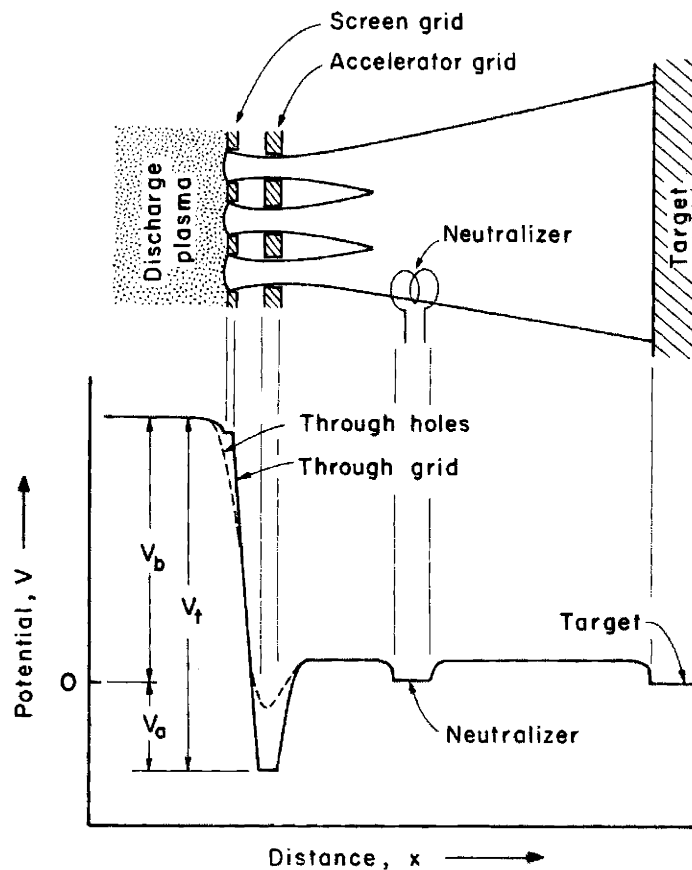

Figure 2.6: Potential across grids of a Kaufman Ion gun. From [34].

The accelerator current (I_a) is an important parameter that was used to monitor the conditions in the ion optics. I_a is due to two distinct effects: charge exchange and direct impingement of ions on the accelerator grid. The former arises when an energetic ion near the accelerator grid passes close to a thermal-velocity (slow) neutral. An electron passing from the neutral to the ion produces a

thermal-velocity ion and an energetic neutral, which continues on its path towards the substrate. The accelerator grid attracts the thermal-velocity ion but it does not do much damage because it only falls through a potential equal to V_a (~50 V). This process dominates at low to moderate ion beam currents (I_b) and does not cause significant damage to the optics. I_a increases linearly with I_b in this regime.

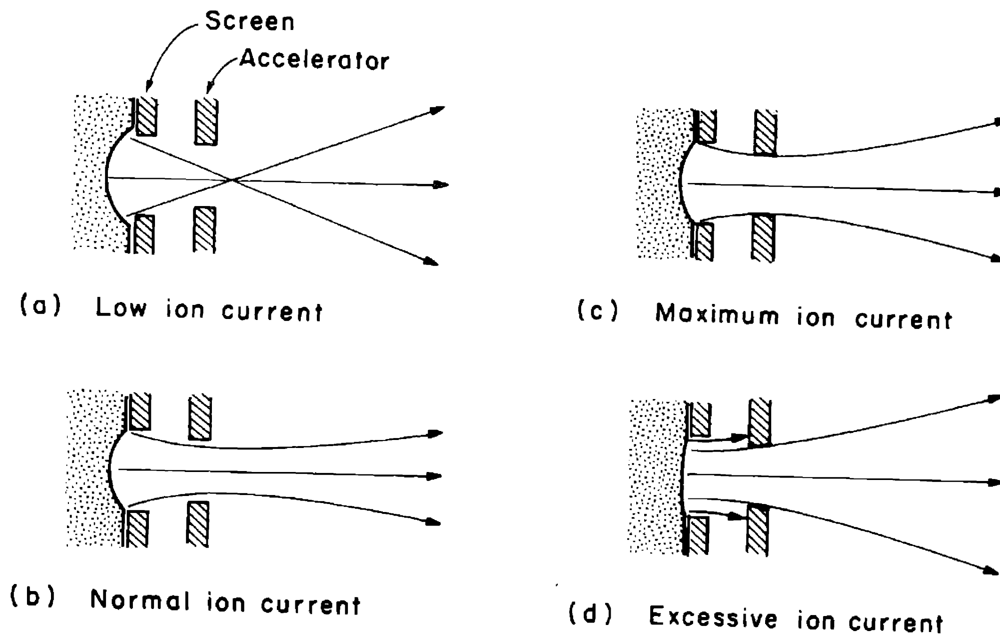

Figure 2.7: Ion beam trajectories through the Kaufman ion gun grids at various ion currents. From [34].

Direct impingement occurs at higher beam currents. I_b reaches a limit where the ion beam trajectories completely fill the accelerator grid holes. (Figure 2.7 c.) Currents above this level lead to direct impingement and severe sputter damage since the ions fall through the full beam voltage potential. Unfortunately, high ion flux experiments had to operate close to this limit. Large I_a does not necessarily imply direct impingement because it could also be due to charge exchange. Only a rapid increase in I_a for a small increase in I_b provides evidence for direct impingement. The picture is further complicated by possible grid misalignment, which leads to direct impingement at even lower beam currents.

The Child-Langmuir law governs the maximum ion beam flux:

$$i \propto \frac{V_t^{3/2}}{d^2}$$

where V_t is the sum of the beam and accelerator voltages and d is the spacing between the two grids. The beam current density is space charge limited: repulsion between ions leaving the plasma discharge and the ions in between the grids becomes the limiting factor. The Kaufman gun was rated up to 1000V, but it performed better at mid-range voltages. 500V was the default setting for all experiments apart from those investigating the effect of voltage on film microstructure.

Another function of the accelerator grid is to prevent electron back streaming from a neutralizer. The neutralizing filaments serve to reduce ion beam "blooming" and prevent surface charging. The latter only applies to insulating films, so it was not a concern for II-CVD of metal (copper) films. The neutralizer was not used in these experiments because of problems with the gun to power supply interface and prematurely failing filaments. Neutralization certainly produces better beam stability but the collimator at the main chamber port alleviated the "blooming" to some extent.

An Ion Tech MPS-3000 ion gun power supply controlled the ion gun in these experiments.[27] It replaced an earlier laboratory built power supply, which lacked feedback control and used a DC supply to heat the filament. AC heating extended the filament lifetime: in a DC supply the emission and heating currents add in the negative end and cause non-uniform heating. The MPS-3000 operated in a number of modes including remote interface with a computer. The unit either controlled or monitored I_c, I_d, V_d, V_a, I_a, I_b, and V_b. One mode of operation set I_b, which controlled the ion flux. Unfortunately, the resolution of I_b was only 1 mA, which allowed considerable drift of the ion flux at the sample.

Therefore, the unit was operated in manual mode where cathode current and beam voltage were dialed in directly.

The problems associated with ion gun operation should also be discussed. It was very difficult to maintain stable ion current with this gun. The overlying symptom was that the ion flux at the substrate decayed as the gun heated up. At high beam currents, the discharge current increased steadily as the gun heated up while the measured ion flux decreased. (Note that the discharge current measures the electron flux to the anode.) This suggests that the magnetic field was weakening. The Kaufman gun used a cylindrical permanent magnet mounted directly behind the anode, which became very hot due to radiative heating from the adjacent cathode filament. (The Curie temperature of a ferromagnet is roughly 800 K.) Improved ion guns use electromagnets to manipulate the magnetic field. On the other hand, the increasing discharge current could also have been due to erosion of the filament, which would have led to higher resistance, increased heating and increased electron emission.

Meanwhile, the accelerator current was increasing both in magnitude and relative to the beam current. The measured beam current was also increasing even though the measured ion flux at the surface either remained the same or decayed slowly. These symptoms also arose at lower beam currents where the discharge current did not drift upwards. Clearly, this effect must relate to direct impingement on the accelerator grid, which is also associated with over-heating. As further ion impingement built up heat, it is possible that the misalignment worsened, which in turn led to higher accelerator currents and further over-heating.

Films deposited for plan view TEM (transmission electron microscopy) were 500 Å thick. A high ion beam flux corresponded to a growth rate of 1 Å/s, so the operator had to find a 500 second window of opportunity. The ion flux decreased steadily for approximately twenty minutes after the gun was first turned on. The

beam flux reached a plateau where the current decayed slowly. It was important to not wait too long because prolonged operation led to high accelerator currents. A successful experiment maintained the current decay around 5% so the starting growth rate was set slightly above target. Thicker cross-sectional samples required stability over 1500 to 2500 seconds. This took the gun to high temperatures and high accelerator currents. The only way to minimize beam current decay was to extend the warm-up period.

Medium current operation (typically 0.3 or 0.5 Å/s) also followed a warm-up period. This current range permitted stable operation. The discharge current would not drift upwards significantly over the course of a 500 Å deposition. Low beam current operation (0.1 Å/s) was very stable: a 250 minute run (1500 Å) had no measurable drift in beam current or deposition rate at the end of the run. The operator kept the discharge current constant throughout the run by turning down the cathode current. This reflected real increases in ion flux at a fixed cathode current since cathode erosion leads to increased resistance and higher thermionic emission.

2.5 Hydrogen atom beam source

This section describes the design considerations and operation principles of the hydrogen atom beam source. The reader should refer to Zau[15] or Chiang[12] for more detailed descriptions.

As the design rule of future semiconductor processes decreases the industry is moving away from wet cleaning to adopt dry cleaning processes. Generation of reactive atom beams provides surface cleaning without the substrate damage associated with, for example, ion etching. However, the engineering issues of generating and delivering atoms beams are very challenging. The standard

process for generating an H atom beam involves passing hydrogen gas across a high temperature filament. An improved method uses a microwave discharge to dissociate the hydrogen, which allows higher gas fluxes at low temperature. Still, the delivery remains as the main obstacle – surface recombination reduces yield dramatically as the atomic beam travels to the reactor. Therefore, Zau designed a beam source that strikes the discharge adjacent to the sample in vacuum.

Zau's design was based on an extended "Evenson microwave cavity" where microwaves are coupled into a coaxial waveguide. Resonance occurs when,

$$\frac{2\pi l}{\lambda} = \tan^{-1}\left(\frac{L}{Z_0 \omega C_0}\right)$$

where L is the microwave cavity length, λ the wavelength, Z_0 the cavity impedance, ω the microwave frequency (2.45 GHz), and C_0 the capacitance of the plasma discharge. When $Z_0 \omega C_0$ is much smaller than one then the resonant length of the cavity is equal to $\lambda/4$ plus any n/2 multiple of λ:

$$l = \frac{1}{4}\lambda + \frac{1}{2}n\lambda,\ n = 0, 1, 2, \ldots$$

This enables the discharge to be struck inside the vacuum system adjacent to the sample substrate. Figure 2.8 shows a schematic of Zau's design. A tuning slug adjusts the cavity length to a resonant condition.

The practical aspects of the design relate to vacuum compatibility and heat generation by the microwave input. A 0.25" silver plated stainless steel center tube enclosed by a 0.625" stainless steel outer tube forms the coaxial waveguide. Teflon® bushings hold the inner tube in place and also provide fair vacuum seal. A Teflon® bushing does not provide high vacuum seal so the space

between bushings is differentially pumped as shown in Figure 2.8. Teflon® is both vacuum compatible and unaffected by microwaves.

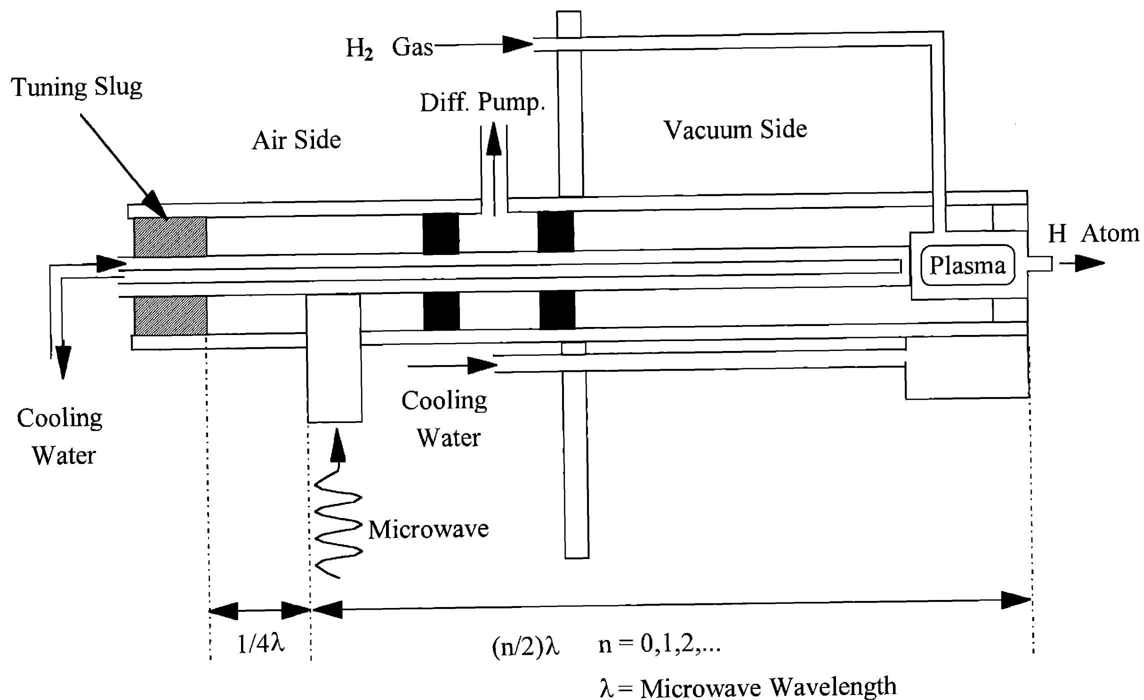

Figure 2.8: Schematic drawing of coaxial waveguide microwave cavity atom source.

An AsTEX 250W 2.45 GHz microwave power generator[28] couples through an N-type Huber-Suhner connector, which contacts the inner silver-plated tube. The microwaves travel inside the annular gap between the two tubes and this generates a discharge in a quartz ampoule at the end of the center tube. Hydrogen gas feeds directly into the ampoule and a hydrogen atom beam exits a short collimating nozzle. A Tesla coil initially ignites the plasma discharge through a high voltage feedthrough on the vacuum flange (not shown on Figure 2.8) that terminates in a 0.010" tungsten wire wrapped around the gas supply

arm of the ampoule. The microwave supply sustains the plasma assuming correctly adjusted gas flow and tuning of the waveguide. The default microwave power setting for the experiments was 100 W and roughly 80% of it was reflected. Water cooling through the center tube dissipated heat generated by these microwave energy losses. Adequate cooling prevented deformation or melting of the Teflon® bushings that hold vacuum.

Zau's design had originally been developed for chlorine atom beams used in plasma etch simulations. The nature of a hydrogen atom beam discharge led to two major modifications. Wood and Wise demonstrated that H atom surface recombination on quartz increases rapidly with temperature.[29] Therefore, the H atom beam source had additional water-cooling piped directly underneath the stainless steel "head" that enclosed the ampoule. Clamping the ampoule and wrapping it in indium foil improved the thermal contact, which was especially important under vacuum conditions. The ampoule design also affected the dissociation yield: data from Geddes showed that dissociation of hydrogen peaks in the 0.2 to 0.4 torr range.[30] Zau's original design maintained several torr of pressure in the ampoule even with minimal hydrogen supply rates. The ampoule's nozzle was redesigned with a wider nozzle diameter (1 mm) compared to the original 0.25 mm. Figure 2.9 shows the estimated pressures for the old and new nozzle designs. All hydrogen atom assisted experiments reported here used the 1 mm ampoule.

The gas flow setting also affects the total gas load in the main chamber. This was minimized while supplying sufficient hydrogen atom flux to remove the carbon impurity. Recall that a cryogenic pump evacuated the main chamber, which posed a problem given the low freezing point of hydrogen. This was a major concern, but the experiments did not suffer form any premature saturation of the cryo-adsorbers because the hydrogen flow rates were very low. Still, it was a good idea to increase the pump regeneration frequency after conducting a series of hydrogen assisted II-CVD experiments.

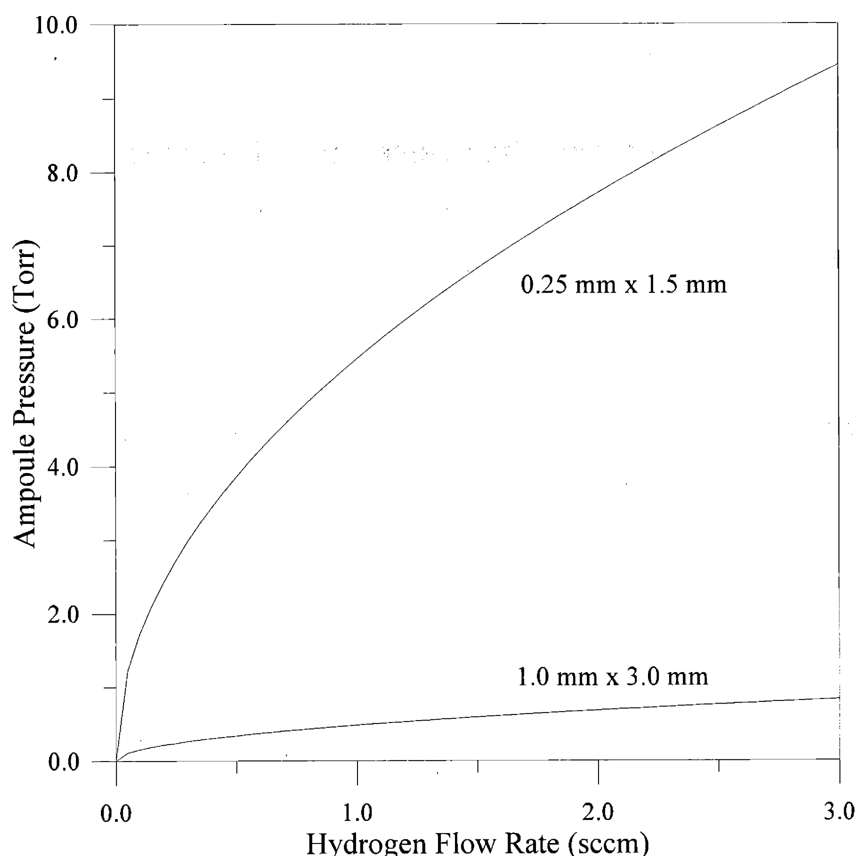

Figure 2.9: Estimated pressure in hydrogen atom beam source's quartz ampoule based on viscous flow of hydrogen through a conduit. The labels refer to the nozzle dimensions: diameter x length. From [12].

The low pressure in the 1 mm ampoule made it difficult to maintain the plasma discharge. Therefore, approximately 0.25 sccm argon was mixed with the hydrogen feed gas, which also enhanced hydrogen dissociation. In practice the goal was to keep the main chamber pressure (as measured) below 1.3×10^{-5} torr. The default hydrogen flow rate was 0.30 sccm, which was accurately controlled by a MFC (mass flow controller). The color of the plasma discharge served as an indicator of the operating conditions: a deep fuchsia verified hydrogen dissociation in the plasma. Initially, the plasma was indigo, which is characteristic of argon plasma.

It usually took approximately twenty minutes before the plasma turned fuchsia (signifying a hydrogen plasma) because air and water vapor leaked into the delivery lines while the gas supply was valved off. Water vapor constituted a significant fraction of the initial gas flow and it took a long time to pump it out of the lines at such low gas flow rates. Heating the stainless steel delivery lines with a heat gun helped to drive out the water vapor.

The hydrogen dissociation fraction was difficult to measure by mass spectrometry because of the difficulty in resolving the adjacent mass peaks of H (1) and H_2 (2). A mass spectrometer was mounted on the 2 3/4" flange opposite the atom source. (See Figure 2.1.) However, estimates did suggest a dissociation fraction of 85% using the 1 mm nozzle.

2.6 Ion Probe

The ion probe monitored the ion flux at the substrate before and after an II-CVD run. The probe mounted on the end of a 0.25" stainless steel rod, which moved freely through an Ultratorr® compression seal on a 2.75" Conflat® flange. The probe was retracted as far as possible when not in use in order to prevent adsorption of precursor gas or reaction byproducts.

The probe (Figure 2.10) was built on a 4-40 stainless steel screw, which threaded into a stainless steel rod. Ions enter through a 0.040" diameter aperture and pass through a 2000 lpi nickel mesh with 8 μm holes. The mesh was biased to -50 V and repelled electrons, which would otherwise reach the collector plate and contribute to the measured current. The mesh also repelled secondary electrons emitted from the stainless steel foil collector surface. The collector connected to a Keithley 485 picoammeter.

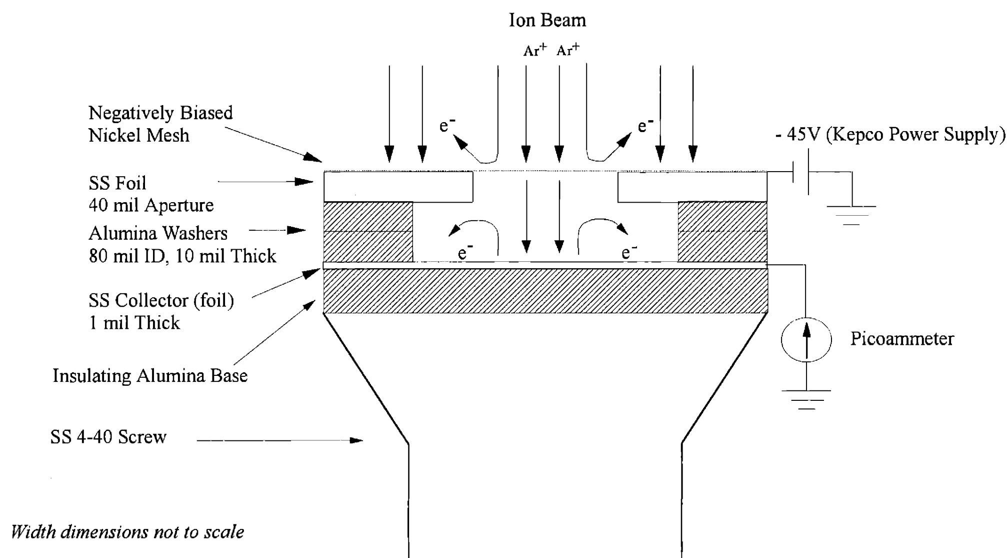

Figure 2.10. Schematic of ion probe built up on 4-40 stainless steel screw. The width dimensions are not to scale.

The following expression calculates the ion flux (*j*) from the collected ion current (*I*):

$$j = \frac{I}{\pi r^2 t}$$

where *r* is the radius of the aperture and *t* is the transmission of the grid. This grid transmitted 36% of the ions. Thus, the multiplier to convert ion current to ion flux ($\mu A/cm^2$) for this probe design was 346.6. For these experiments the range of currents measured by the picoammeter was 0.004 μA to 0.1 μA.

2.7 Transmission Electron Microscopy (TEM)

The scale of the II-CVD microstructure called for the high-resolution capability of transmission electron microscopy (TEM). The high operating voltage of a TEM instrument translates into very small wavelength and high lateral resolution. The use of very thin samples maintains the resolution: electrons undergo few scattering events as they traverse the sample. Sample preparation for TEM is typically slow and difficult, which would be a major concern when investigating an extensive matrix of experimental conditions. However, plan view samples did not require preparation because the II-CVD films of optimal thickness (500 Å) were grown on commercial TEM substrates.

The micrographs were taken on either of two JEOL 200CX microscopes at MIT's Center for Materials Science and Engineering (CMSE).[31] Contrast in bright-field imaging was due to differences in scattering between relatively high Z (mass number) copper and low Z of amorphous carbon. The crystalline copper also produced diffraction contrast when grains were aligned for Bragg diffraction. Most micrographs were imaged using small objective apertures. This enhanced the overall contrast as well as the contrast between individual copper grains (columns). Dark-field imaging used the objective aperture to select the diffracted rather than the transmitted beam. This produced high intensity illumination of grains in a particular crystal orientation while the background remained dark. Tilting of the sample led to preferred orientation of a particular grain with respect to the electron beam.

Coherent diffraction of electrons by crystalline material yields characteristic diffraction patterns from a selected area – selected area diffraction (SAD). In SAD, defocusing the condenser lens produces parallel illumination at the specimen while a selected-area aperture limits the diffracting volume. Polycrystalline materials have ring patterns composed of spots (reflections) where each ring corresponds to a family of planes that is randomly oriented

about the same azimuthal direction. The position of atoms in a unit cell affects the intensity but not the direction of a diffracted beam. Depending on the crystal structure, reflections from certain planes are annihilated. A "structure factor calculation" determines how the atom arrangement affects a scattered beam. For example, FCC diffraction only occurs for (hkl) planes with unmixed integers. Furthermore, the rings can be indexed to determine the lattice parameter and identity of the crystalline material.

The default magnification for micrographs was 100,000 X magnification, which were enlarged to 300,000 X after developing the negatives and producing 8" by 10" prints. This magnification yielded optimal detail, resolution and surface area for inspection and quantitative analysis.

Ted Pella, Inc. manufactures a variety of substrates for TEM.[32] Exploratory experiments investigated the suitability of six different substrates. The Pelco® Carbon Type-A substrate exhibited the best performance. The Type-A substrate has an approximately 35 nm thick layer of Formvar on one side of a 3 mm TEM grid, and 20 to 30 nm of amorphous carbon on the other side; the Formvar served as a substrate for the evaporated carbon. Other types of substrates would have required thin film deposition onto the Formvar. Unfortunately, the Formvar film tended to drift and even buckle due to heating under a focused electron beam of a TEM. Therefore, the II-CVD films were deposited onto the carbon side of the type-A substrate. The Formvar film could be removed from the type-A substrates by immersion in chloroform. Experiments did not show significant difference in the number of defects on substrates with or without Formvar remaining. The unsupported carbon films were brittle, so the removal process was abandoned. The substrates were also examined without any film deposit. The transmitted beam appeared to undergo virtually no scattering and there was no discernible diffraction.

In one sense, an amorphous substrate was ideal because it did not impart any preferred crystal orientation at the initial stage of film growth. However there was some concern about using a substrate that corresponded to the primary impurity (carbon), and earlier II-CVD researchers had deposited films on silicon nitride substrates.[33] Here, a HNO_3:HF:$COOH_3$ mixture back-etched a silicon wafer with a 100 nm layer of silicon nitride. The sample mounted on a glass slide and black wax masked it so that the acid etched a 1 mm^2 central area. The process had to be monitored carefully by removing, rinsing and inspecting the sample under a microscope since the acid mixture also etched the silicon nitride, albeit at a slower rate. Two samples prepared by this technique exhibited identical microstructures compared to the corresponding films on amorphous carbon substrates.

Hydrogen atom beam assisted II-CVD etched away the type-A substrates, as expected, since the atomic hydrogen beam reacts with carbon, so these films were grown on silicon monoxide/ Formvar substrates. These substrates exhibited considerable surface topography and damage as received from the supplier because the underlying Formvar deformed during deposition of the silicon monoxide. The evaporation of silicon monoxide uses a tungsten basket, which radiates sufficient heat to bring the Formvar film close to its melting point.

2.8 Cross-sectional Transmission Electron Microsocpy (XTEM)

Cross-sectional transmission electron microscopy (XTEM) was very important because it verified that the process of continuous columnar growth took place, which otherwise could only be inferred from the plan view microstructure. The sample preparation was very difficult as it involved sectioning a sample and thinning an area with a width of only a few thousand Ångström.

The first issue that the author faced in XTEM was substrate selection. The final sample preparation step involved ion milling, so the relative sputtering rates of the film and its substrate had to be taken into account. The first attempts at XTEM used copper films deposited on etched polysilicon features. (The decision to use a substrate with features was motivated by increasing the effective width and surface area of the interface that was going to be thinned.) Unfortunately, the sputtering rate of silicon is approximately three times that of copper.[34] Consequently, the copper film etched away before the substrate and it was very difficult to find the endpoint where the copper had been thinned sufficiently for electron transmission.

The optimal substrate is, of course, copper. There was some concern about how a copper substrate would affect the growth process given the possibility that the II-CVD film could grow preferentially on certain crystallographic orientations of copper grains on the substrate. Therefore, placing them on a hot plate for several hours oxidized the copper substrates. The substrates were in fact OFHC (oxygen free high conductivity) copper VCR® gasket "blanks". This substrate proved to be an ideal choice because its 0.47 inch diameter happened to fit the QCM sample holder without modification.

XTEM sample preparation was a complex and delicate process. After film deposition, the circular sample was bond waxed to a glass slide and an approximately 2.5 mm wide strip was cut from its center with a slow speed diamond saw. This strip was remounted on the slide and cut in half across the width. Then the two pieces were glued together so that the II-CVD films faced each other. It was important to preserve the orientation of the rectangular pieces so that one end had two facing layers of II-CVD film. The adhesive was M-bond 610, which is designed for attaching leads to strain gauges; consequently, it stood up to the mechanical abuse of XTEM sample preparation.[35] M-bond 610 uses tetrahydrofuran (THF) as a solvent; therefore, it does not dissolve in acetone. Acetone cleaned the sample and dissolved bond wax throughout the

XTEM sample fabrication process. The curing took place at 100°C for four hours under pressure applied in a special vice with Teflon® clamping surfaces. The diamond slow speed saw sectioned the resulting sandwich into approximately 600 μm thick slices. This was the most critical juncture of the fabrication: the diamond saw had to cut at minimum speed when it traversed the bonded interface. The slices were 2.5 mm long and twice the copper substrate thickness in width (1.75 mm) with face-to-face II-CVD films separated by M-bond 610 down the middle.

The remainder of the process involved thinning the sample until some part of the II-CVD film transmitted an electron beam. The 600 μm thick sample was ground from both sides in order to flatten it, using alumna grit paper with particle size ranging from 20 μm to 1 μm. After thinning it to approximately 150 μm, the sample moved on to a closed-loop electronic feedback controlled VCR Group Model D500i dimpler, which monitors thickness to within 1 μm.[36] The first thinning step actually used a wide flattening tool on both sides to bring the thickness down to approximately 70 μm. Normally the thinning/ polishing process uses 3 μm diamond particles that embed into a stainless steel tool. Unfortunately, the diamond tends to embed into a softer sample like copper and the stainless steel tool abrades instead. Therefore a "soft" tool wrapped in polishing cloth – normally a polishing tool – was used in this process. This introduced some inaccuracy in the sample thickness monitoring. After flattening, a narrow dimpling tool brought the center down to an ultimate thickness of approximately 10 μm. The final dimpling step used 1 μm diamond slurry. As he gained more experience, the author pushed the limit in bringing samples to lower thickness, but it did increase the risk of having the sample split at the center interface where it was glued. After bonding the sample to a slotted TEM sample holder, it moved on to a Gatan ion miller.[37] This ion miller employs endpoint detection: a laser beam strikes the sample during milling and triggers a photodetector once a pinhole forms in the center of the sample. A 10 μm sample

required approximately ninety minutes of milling followed by a few minutes of fine-tuning after inspecting it in a TEM instrument.

The XTEM samples actually had several layers of II-CVD films. In other words, a number of thin films deposited under different conditions were layered on top of each other. This was not only efficient, but also conveyed information about the effect of changing deposition parameters. For example, is there an abrupt interface between two II-CVD layers deposited at different temperatures?

2.9 Atomic Force Microscopy & Scanning Electron Microscopy

Plan view TEM has very limited depth resolution, so it does not convey any information about film topography. It is important to establish if there is any roughening of the surface associated with the columnar growth process.

Atomic force microscopy (AFM) is a real-space imaging technique that produces high-resolution topographic images in all three dimensions. The AFM instrument uses a sharp tip mounted on a flexible cantilever. When the tip comes to within a few Å of a surface, repulsive van der Waals forces cause the cantilever to deflect. To monitor this deflection light a laser diode reflects from the back of the cantilever into a position-sensitive photodiode. Therefore, a given cantilever deflection corresponds to a specific position on the highly sensitive position-sensitive photodiode. This gives the instrument sub-Å resolution. AFM employs a piezoelectric transducer to scan the tip across the sample, and a feedback loop operates on the scanner to maintain constant separation between the tip and the sample. This constant separation is, of course, essential for accurate deflection measurements.

The lateral resolution of AFM is not as good. The cantilever deflection due to van der Waal forces involves interaction between a number of atoms on the tip and on the surface; therefore, atomic resolution is generally not possible. The effective resolution of the Topometrix TMX-2000 instrument used in this work was 10 nm.[38] Conventional AFM tips are square pyramids formed by CVD of silicon nitride on a (100) etch pit in silicon. This pyramid limits profiling across steep features, so modern Topometrix tips are in fact 10:1 aspect ratio carbon filaments grown on top of the silicon nitride. One advantage of AFM is that it operates under ambient conditions. However, vacuum is necessary for high-resolution work because airborne adsorbates and contaminants will affect the measurement.

Unfortunately 10 nm resolution limit is close to the column diameter of II-CVD and considerably larger than their separation. Assuming that the II-CVD film surface has nanoscale roughness due to the columns, it would be impossible to measure with the available AFM instrument. However, the AFM does retain sub-Å vertical resolution, so it was possible to determine overall roughness. Measurements for varying deposition conditions were compared to the RMS roughness of an uncoated sample. One cm square dies of low-stress silicon nitride (5000 Å) deposited on silicon served as substrates for AFM samples. The same samples were also used for four-point probe resistivity measurements and XPS analysis.

2.10 X-ray Photoelectron Spectroscopy

X-ray photoelectron spectroscopy (XPS) provided quantitative analysis of the copper to carbon ratio in II-CVD films. In XPS, monoenergetic soft X-rays eject photoelectrons from the sample. The kinetic energy (*KE*) of an ejected electron

depends on the photon energy ($h\nu$) and the binding energy (BE) as expressed by Einstein's photoelectric law:

$$KE = h\nu - BE$$

The photon energy is known, so measuring the kinetic energy determines the characteristic binding energy of an inner core electron. The identification of core-level binding energies provides unique signatures of the elements in the sample. The actual kinetic energy measurement is offset by a work function for the spectrometer. Spectrometers usually use either Mg (1256.6 eV) or Al (1486.6 eV) Kα X-rays.

Quantitative analysis requires measuring the relative peak intensities for the identified elements. The measurement unit for the peak area of an element is counts-eV per second. The relative sensitivity of two elements depends on their respective photoelectric cross-section and photoelectron mean free path, so the peaks have to be normalized. Furthermore, electrons of different kinetic energy do not transmit with equal efficiency through the electron energy analyzer. This requires the use of standards to calibrate an instrument. The Perkin Elmer 5100 system at MIT's CMSE (Center for Materials Science and Engineering) had a relative sensitivity of 0.296 to 5.321 for carbon and copper, respectively.[39] Comparison to a standard with a known of ratio of copper and carbon is preferable. However, there is no bonding between the copper and carbon so the standard system calibration proved to be quite accurate. The absolute sensitivity of XPS is 0.01-0.3 atomic % depending on the element, so it is not suitable for trace analysis.[40] Apart from the hydrogen assisted II-CVD films, the carbon fraction is much larger than the aforementioned range.

XPS also provides chemical state analysis. Although binding energy gives positive identification of an element, it is only approximately constant and shifts up to several eV for varying bonding conditions. The binding energy of the

carbon provides information about the chemical state of the presumably amorphous carbon in the II-CVD films. Copper undergoes spin-orbit splitting, which results from a coupling of the spin of the unpaired electron left behind after its partner has been photoejected with the angular momentum of the orbital. This produces two possible final energy states: spin up or spin down. For example, $2p_{3/2}$ and $2p_{1/2}$ for copper. Beyond these two peaks, copper produces very strong "shake-up satellites" when it is oxidized. When a core electron ejects, a valence electron may also be simultaneously excited to an empty orbital level during the relaxation process. This "shake-up" process leads to lower energy photoelectrons, which correspond to higher binding energy and appear in the spectrum as satellite peaks. Cu(II)O distinguishes itself from Cu^0 and Cu^+ by having very strong satellite peaks.

The XPS analysis was not *in situ* so the surface layer oxidized and also became contaminated by organic matter. Only photoelectrons ejected from atoms in the top few surface layers appear in XPS spectra. This surface spectrum was not characteristic of the film: it had a majority fraction of carbon from organic contamination as well as oxygen and showed the copper "shake-up" satellite peaks of Cu(II)O. Therefore, the surface layers were sputtered away using an argon ion gun that was attached to the XPS system. The oxygen peak and copper satellites disappeared immediately while the carbon fraction dropped to lower levels as the depth profiling progressed. The depth profiling continued in six-second increments until the carbon fraction reached a plateau. Further sputtering would actually increase the carbon fraction since carbon has a smaller sputtering yield compared to copper. It was very important to align the X-ray source with the ion gun so that they struck the same area.

The Perkin Elmer 5100 XPS is designed for small samples. Both II-CVD films on 3 mm TEM grids and 1 cm square silicon dies were examined by XPS. One of the drawbacks associated with XPS is the relatively large spot size but this was not an issue for these samples. An aperture leading to the photoelectron

analyzer defines the effective spot size for this instrument. In fact, analyzing a larger area is desirable for average composition data of a blanket thin film compared to, for example, auger electron spectroscopy (AES) used by past researchers.[33] In general, XPS produces better quantitative data than AES.[40] The fragile TEM grids were difficult to analyze if damaged because it would lead to exposure of the amorphous carbon substrate. However, data from II-CVD films on intact TEM grids and silicon dies proved to be consistent for identical deposition conditions.

2.11 Scanning Transmission Electron Microscopy (STEM) & Energy-Dispersive X-ray Spectroscopy (EDS)

XPS quantitative analysis generated average film composition data. STEM-EDS, on the other hand, enabled composition analysis with direct reference to the microstructure. The STEM system at MIT was a Fisons VG-H603[41] coupled with a Link/ Oxford[42] EDS system.

In a STEM system an electron gun produces and accelerates the high-energy electron beam, which is demagnified by an array of electromagnetic lenses. Electromagnetic lenses raster the focused electron beam – also referred to as the "probe" – across the sample. The VG-H603 uses a field emission electron gun, which produces 0.1 nA of current for an electron probe diameter of 1 nm or approximately 10^{23} electrons/cm^2. This allows both high-resolution imaging and sufficient beam current for high-resolution microanalysis.

Bright-field image formation is similar to TEM. The beam rasters the surface and an aperture selects the transmitted beam, which then passes through to a solid-state electron multiplier. An annular dark-field collector (ADF) collects scattered

and diffracted electrons beyond a certain minimum angle to produce a complementary high-contrast, high-resolution dark-field image.

The electron beam interacts with surface atoms to produce characteristic X-rays. High-energy radiation ionizes an atom by removing inner shell electrons. To return the atom to its ground state, an electron from an outer shell fills the vacant inner shell, which releases energy that is characteristic of the potential difference between the two shells. This excess energy leads to either Auger electron emission or X-ray photon emission. An example of characteristic X-ray emission is Cu-Kα for ejection of a K-shell electron that is replaced by an electron from the L_3 shell. The Link/Oxford system uses a windowless detector that subtends a solid angle of 0.3 Sr at the sample. The windowless detector aids detection of low-energy, low Z materials like carbon. Qualitative analysis involves comparing detected X-ray energy peaks to tabulated data.

STEM-EDS microanalysis has two modes of operation. The first, compositional mapping, involves rastering the surface with the electron probe to detect X-ray peaks of interest. The maps compare directly to an equivalent STEM image. The elemental image is a 128 x 128 pixel digital image with eight levels of gray scaled to the intensity of the X-ray peak. The high current density of the VG-H603 allows fast sampling at very high resolution with the 1 nm probe. Carbon maps, however, do not provide any useful information since organic contaminants cover the sample. Hydrocarbon contamination is a major artifact in STEM imaging as the high-density field emission beam effectively cracks organic contaminants on the sample surface.

The second mode of microanalysis takes a spectrum from a single point. The 1 nm probe allows sampling between columns in the II-CVD microstructure. *This provided the answer to the question whether there was any copper between the columns in the II-CVD microstructure.* Unfortunately, the environmental carbon

contamination prevented any attempt at quantitative analysis. The basic equation for quantitative analysis is:[43]

$$C_i = \left(I_i / I_{(i)}\right) ZAF_i$$

where C_i is the fraction of element, I_i is the intensity of the sample peak, $I_{(i)}$ is the intensity of a standard, ZAF_i is the product of correction factors for the atomic number (Z), X-ray adsorption (A) and fluorescence (F). However, the quantitative analysis provided some guidelines for a qualitative analysis of the X-ray peaks. The X-ray peak intensity is directly proportional to the fraction of the element in the sample. Carbon has a relatively large ZAF correction due to X-ray absorption, which produces relatively low intensity peaks unless there is heavy organic contamination. Therefore, the primary focus of the qualitative analysis was the ratio of copper peak intensity from sampling on copper columns versus that in between the columns in the II-CVD microstructure.

2.12 Resistivity

The resistivity of the II-CVD films for various depositions was measured using a four-point probe technique. A small current passes through two outer probes while two inner probes measure the voltage drop. (See Figure 2.11.) The resistivity (ρ; $\mu\Omega$-cm) derives from Valdes' equation:[44]

$$\rho = F\frac{V}{I}t$$

where V is the measured voltage, I is the applied current, t is the film thickness, and F is a geometric factor that depends on the ratio of probe spacing to sample diameter. The applied current is adjusted to avoid erroneous readings due to I^2R

heating. The setting depends on the resistivity and thickness of the film. In practice, the current is reduced until the voltage reading changes linearly with current.

The four-point probe instrument used an Alessi C4S-54/5S probe head with osmium probe tips, which had 0.005" tip radii and 1 mm probe spacing.[45] The probe head mounted on a structure built from spare laser table hardware and other parts machined by the author. One cm silicon dies with 5000 Å of silicon nitride on served as substrates for resistivity samples. The geometric factor (F) for this probe spacing and sample diameter was approximately 3.9. The II-CVD film thickness was, of course, carefully monitored during deposition, but it was also verified by profilometry. The mean free path for scattering of electrons in copper is approximately 800 Å, so it was important to grow relatively thick films in order to avoid contribution from electron surface scattering. The typical thickness for resitivity samples was 2000 Å.

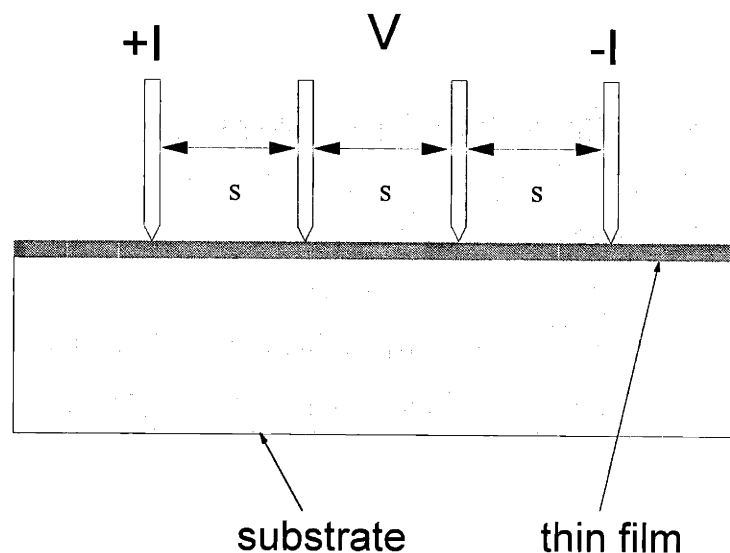

Figure 2.11: Schematic of 4 point probe measurement. The probes are separated by spacing "s" (1 mm). Current is forced between the two outer probes and a voltmeter measures the potential drop across the inner probes.

Chapter 3: Experimental Results

This chapter presents qualitative observations of the II-CVD microstructure evolution for various deposition conditions; quantitative analysis of the TEM micrographs; and data from XPS, STEM-EDS and AFM analysis.

3.1 Chemistry and Adsorption of Cu(I)hfac(vtms) Precursor

A characteristic columnar microstructure, which will be demonstrated throughout this chapter, requires an Ion-induced CVD process that yields relatively high fractions of copper. Ro's analysis showed that columnar microstructure does not evolve at high carbon fractions with the DMGhfac (Gold) precursor.[16]

Della Ratta originally adopted the Cu(I)hfac(vtms) precursor for II-CVD because it had shown great promise in thermal CVD.[33] Schumacher Co. synthesized the chemical for an early 1990s development program of precursors for copper metallization in integrated circuits. The motivation for developing copper metallization was that transistor switching speed was projected to no longer be the performance bottleneck of integrated circuits; instead, the RC delay of the interconnection lines determined propagation delay. Given copper's lower resistivity (1.67 μΩcm) than conventional aluminum interconnects (2.65 μΩcm) it became the target for future metallization schemes. Unfortunately, a number of obstacles prevented the adoption of copper. A major problem was that copper halide byproducts of plasma etching do not have sufficient vapor pressure. The Cu(I)hfac(vtms) system circumvented this problem by depositing Cu selectively on conducting surfaces. Therefore, a proposed metallization scheme involved selective deposition of copper from Cu(I)hfac(vtms) on conductive seed material.[46]

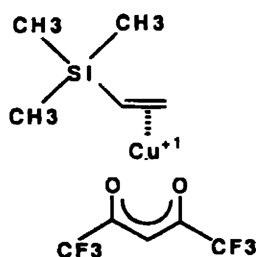

Figure 3.12: Cu(I)hfac(vtms).

The high purity, selective CVD of copper from Cu(I)hfac(vtms) suggests that the process requires electron transfer at the substrate. Norman et al. postulated a bimolecular disproportionation process, which does not decompose the precursor and avoids carbon incorporation: [47,48]

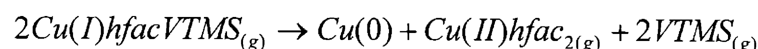

$$2Cu(I)hfacVTMS_{(g)} \rightarrow Cu(0) + Cu(II)hfac_{2(g)} + 2VTMS_{(g)}$$

Gross and Donnelly investigated the deposition reactions and discovered that Cu(I)hfac(vtms) deposited by way of decomposition at ultra-high vacuum (UHV).[49,50] They concluded that the disproportionation reaction requires relatively high pressures (hundreds of mtorr) found in typical CVD reactors. The bimolecular disproportionation process relies on two precursor molecules coming together. Gross and Donnelly speculated that additional molecules physisorb and interact with a monolayer of chemisorbed molecules.

II-CVD also follows a *decomposition* reaction, which leads to the associated carbon incorporation. The purity of an II-CVD process depends on the relative rate of copper decomposition to the rate of carbon incorporation from organic byproduct molecules. The rate of byproduct desorption helps to counteract the latter. On the other hand, Gross and Donnelly showed that copper-bearing species do not desorb below 250°C. The activation energy for thermal CVD of copper from Cu(I)hfac(vtms) is only 13 kcal/mol (1.8 eV),[51] so ion-induced decomposition does not require very energetic ESAs. This in turn predicts

relatively high decomposition yield (copper atoms per ion); Chiang calculated a gross deposition yield of nine atoms per molecule with 500 eV ions.[12]

The adsorption behavior also dictates the viability of the precursor since the II-CVD process relies on high surface coverage. The QCM permitted easy measurement of adsorption kinetics. Figure 3.1 shows adsorption as a function of time at three temperatures and three different gas fluxes. The gas flux corresponds to a local pressure at the surface as measured by the capacitance manometer.

Adsorption experiments require low base pressure ($1x10^{-8}$ torr) and pre-sputtering of the QCM substrates to remove surface contaminants. The QCM substrates had predeposited copper II-CVD films in order to simulate conditions during II-CVD. The needle valve on the gas delivery system controlled the precursor flux. The experiment started when the valve to the gas source opened. The QCM frequency data converts to a number of molecules per unit area with the assumption that the vtms ligand desorbs as soon as the Cu(I)hfac(vtms) adsorbs on the surface.[49] The precursor gas flow was turned off after 500 seconds, but the frequency monitoring continued for several hours to determine whether anything desorbed from the surface. This distinguished between chemisorption and physisorption.

Figure 3.1 shows that surface coverage saturated at $2x10^{14}$ molecules per cm^2 at 6°C and 27°C. However, at 0.07 mtorr (very low gas flux) the adsorbate coverage did not quite reach this level because the gas flux has a gradient across the substrate under these conditions. The gas flux at the point on the substrate farthest away from the gas supply may be so low that it is close to the vacuum system's background pressure. The adsorbate did not desorb after several hours. This indicates that Cu(I)hfac(vtms) chemisorbs on the substrate.

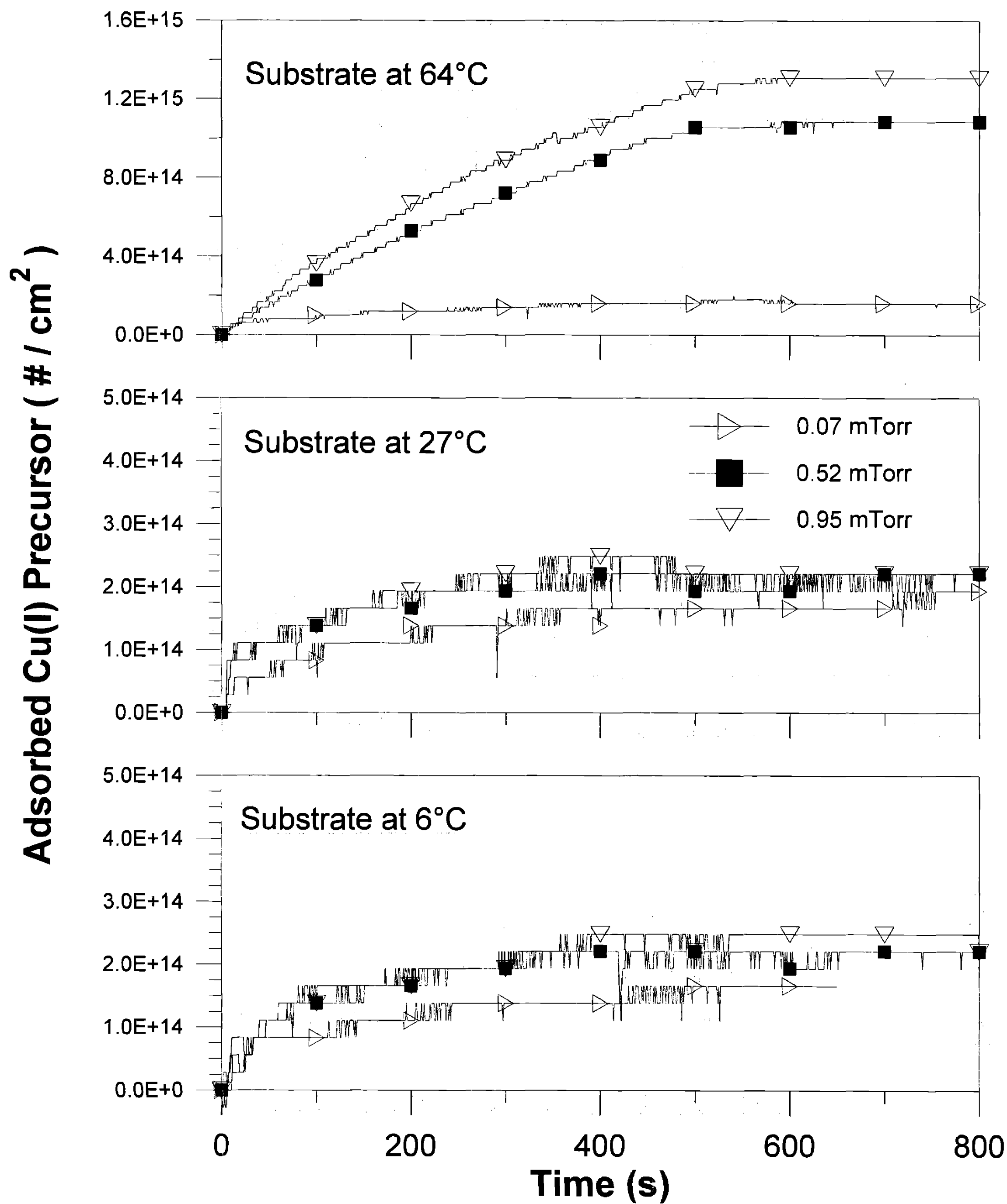

Figure 3.1: Cu(I) precursor adsorbed versus time at three temperatures and three different gas fluxes (measured as pressure at the substrate). The steps in the curves are due to the resolution limit (1 Hz), which corresponds to 3E+13 molecules.

The number of molecules on the surface did not saturate at 64°C but continued to increase steadily until the precursor gas flow was shut off. Clearly, this was due to decomposition (effectively thermal CVD) of the precursor at elevated temperature. The slope of the plot translates to an effective deposition rate of 0.01 Å/s. This is going to affect II-CVD at higher temperatures. The II-CVD microstructure above ~60°C starts to reflect a synergistic effect of ion- induced and thermal CVD. Chapter 4.4 examines this effect in detail.

3.2 Rate Experiments

Before devising a set of experiments for microstructure analysis it is necessary to determine how rate kinetics affect the growth process. The rate experiments provide information about interaction between process variables. For example, the growth rate may depend on substrate temperature, precursor gas flux, and ion flux. If the growth rate were a strong function of all three variables then it would be necessary to perform a full factorial design of experiment (DOE).

Figure 3.2 shows the effect of gas and ion flux on the growth rate with 500 eV ions at 6°C. The substrate had predeposited II-CVD copper on a QCM substrate. This simulated continuous growth and negated any potential contribution from the surface. The deposition proceeded for thirty seconds and the slope of a plot of area mass density versus time determined the growth rate. The conversion from grams/second to Å/s assumes deposition of pure copper. As discussed in Chapter 2, this approximation retains accuracy due to the low weight fraction of carbon in most II-CVD films.

The graph delineates two distinct growth regimes: (a) *ion-flux-limited*, and (b) *gas-flux-limited.* The growth rate is approximately linear at higher precursor gas pressures. At lower gas fluxes the curve is parabolic as the growth rate reaches

a maximum. Clearly, there is insufficient gas flux to maintain high surface coverage with adsorbed precursor. The II-CVD process is a competition between deposition and sputtering. When the gas flux is low, the ion beam sputters the empty surface sites. As the ion flux increases, the adsorbed surface coverage decreases further and the sputtering rate increases; consequently, the deposition rate decreases. The surface coverage at very low ion flux is close to 100%, so there is essentially no contribution from sputtering.

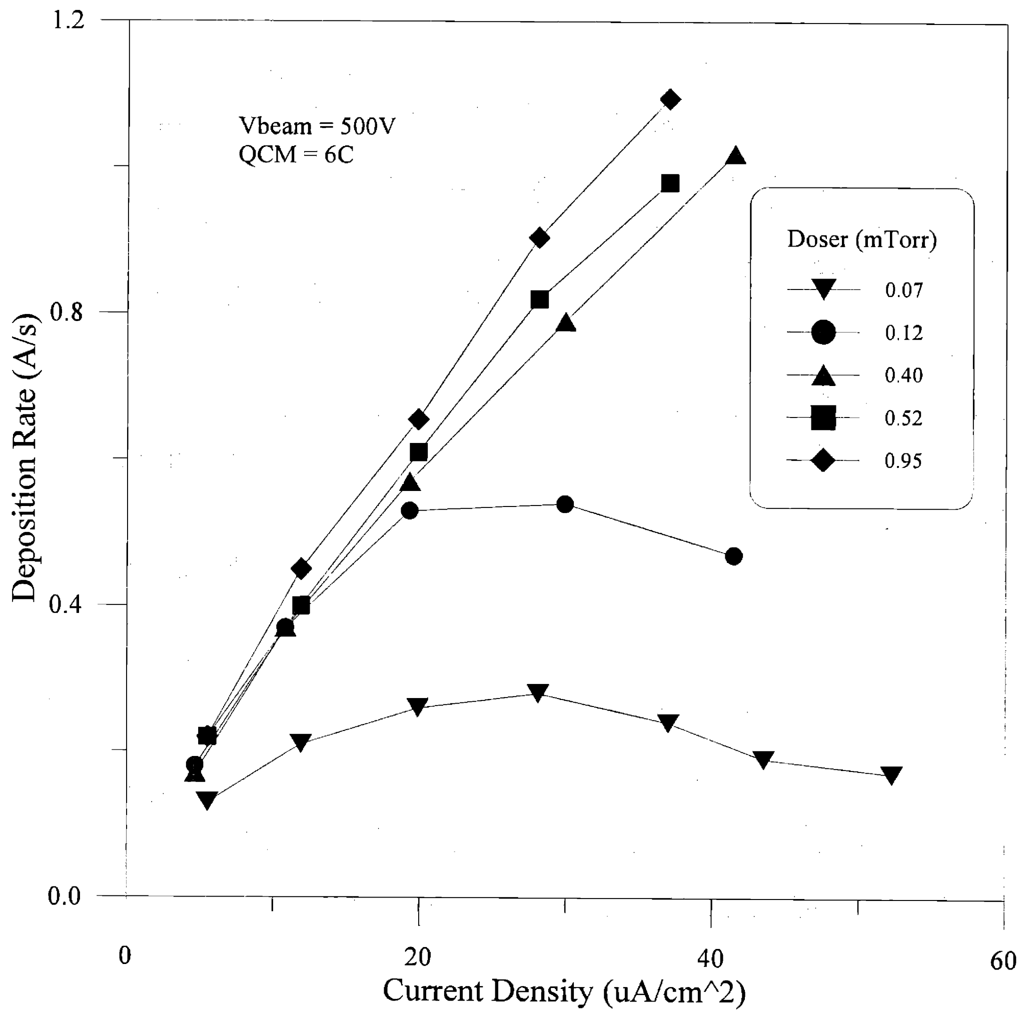

Figure 3.2: Deposition rate versus current density (ion flux) for various precursor gas pressures at the substrate surface. 500 eV ion beam and 6°C substrate temperature.

Figure 3.3 shows the effect of temperature. The graph plots growth rate versus ion beam flux for three temperatures at three different gas pressures. Higher temperature should increase organic byproduct desorption and reduce carbon incorporation. The ion-flux-limited regime sees a small reduction in growth rate with increased temperature. This is due to a reduction of carbon incorporation at higher temperatures – the QCM measures the sum of copper and carbon deposition. Temperatures above the range represented on this graph will bring about an increased growth rate due to contribution from thermal CVD. At low gas pressure (0.07 mtorr) there is a marked reduction in deposition rate with increasing temperature. This is because a film deposited at low temperature and low gas flux contains a large fraction of carbon. Note that the conversion to deposition rate is no longer accurate under these conditions, but the scaling remains constant since the QCM measures the actual mass of the deposited film.

The gas flux limited regime should be avoided for a number of reasons. The lower surface coverage by adsorbed gas molecules leads to increased sputtering by the ion beam. The sputtering yield of copper by weight is approximately twenty times higher than carbon, which leads to increasing carbon fractions as the surface coverage decreases. The growth process is also very sensitive to changes in the gas flux, which is measured as a local gas pressure. There is a gradient of gas pressure across the sample; therefore; the thickness and composition is not constant across the sample in this regime. Also, the experimental set-up is not designed for accurate control of the gas flow since the alignment of the QCM substrate holder with the beam sources involves visual inspection. Finally, it is difficult to extract information about the II-CVD mechanism from films grown in this gas-flux-limited regime because of the strong dependence on three variables: temperature, gas flux and ion flux.

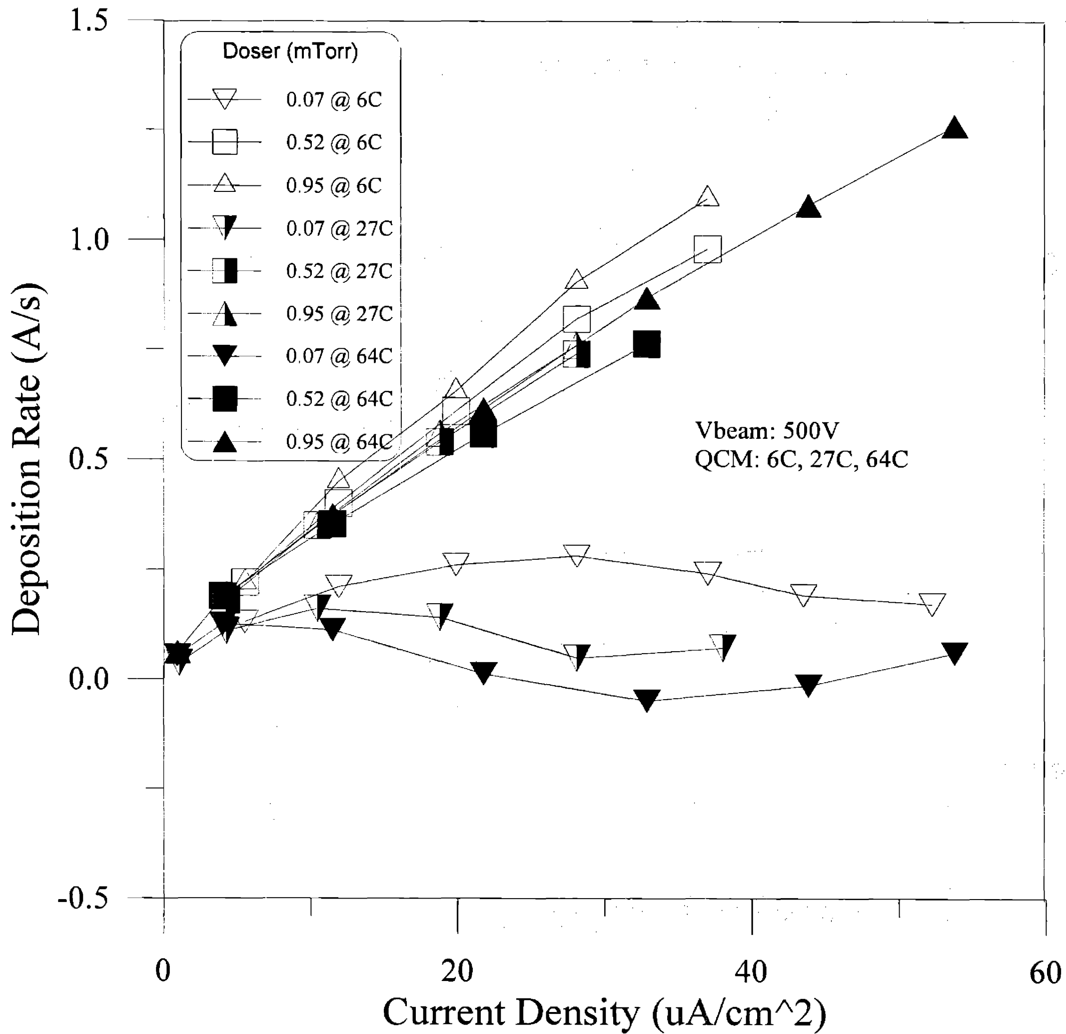

Figure 3.3: Deposition rate versus current density (ion flux) at various substrate temperatures and precursor gas pressure settings.

The ion beam voltage is the final variable that has to be considered. Increased beam voltage will increase the deposition rate at a given ion flux because of the increased deposition yield for both carbon and copper. A more energetic ion will create more excited surface atoms with sufficient energy to decompose the adsorbed precursor molecules. The sputtering yield, of course, also scales with beam voltage. Sputtering of pure copper and carbon samples provide information about how the relative sputtering yields are affected, and determines the respective threshold voltages for sputtering. Carbon has a relatively high

threshold voltage for sputtering; operation below a threshold voltage leads to higher levels of carbon incorporation.

3.3 Quantitative Microscopy

It is essential to go beyond qualitative observations and acquire quantitative metrics from the TEM plan view micrographs. The quantitative data are building blocks for developing a model of II-CVD. Quantitative analysis overcomes any bias introduced by earlier work; for example, the assumption that the microstructure represents a complete segregation into two phases[16] (copper columns surrounded by amorphous carbon), which this thesis will show to be incorrect. The two critical metrics of the II-CVD microstructure are: (a) the average column diameter; and (b) the atomic fraction of copper.

3.3.1 Column Diameter

R.L. Fullman established quantitative measurement techniques for determining particle size and volume fraction of various particle geometries in metallographic samples.[52] He developed quantitative relationships between various mean dimensions on a polished cross section and the actual dimensions of particles.

Fullman's analysis considered a sample containing a phase in the form of randomly oriented rods of length H and radius r, where $H >> r$. He defined a cube of unit dimension where straight lines pass throughout the unit cube parallel to a cube edge. The number of lines intersected per unit length (N_L) along the line is equal to the number per unit volume (N_V) multiplied by the probability that a line hits a single rod. This probability is in turn equal to the average area ($\bar{a}$) projected in the imaged plane by randomly oriented rods:

$$N_L = \bar{a}\, N_V$$

If ϕ is the angle between axis of the rod and the normal to the plane then,

$$a = 2rH \sin\phi$$

Now, let $p_a da$ be the probability that the projected area is between a and $a + da$. The probability is expressed in terms of ϕ in order to get workable units:

$$p_a = p_\phi \left|\frac{d\phi}{da}\right| = \frac{\tan\phi}{2rH}$$

Evaluating average area ($\bar{a}$):

$$\bar{a} = \int_0^{2rH} a p_a da = 2rH \int_0^{\pi/2} \sin^2\phi \, d\phi = \frac{\pi r H}{2}$$

However, the II-CVD microstructure is not random: the columns grow perpendicular to the substrate so it is <u>not</u> necessary to account for the projection of a rod/column in the plane. Therefore, Fullman's treatment is adapted for this special case where ϕ = 90° and $\bar{a}$ = $2rH$. Thus,

$$N_L = \bar{a}\, N_V = 2rH\, N_V \qquad [3.1]$$

This corresponds to a lengthwise projection of the column in a volume partly defined by length H. Clearly, H must be re-expressed in terms of a parameter that is independent of volume. (Note that this analysis implies that it is impossible to determine the average length (H) of randomly distributed rods from two-dimensional micrographs.) The goal is to express $H\ N_V$ in terms of a suitable metric, namely N_A (number of columns per unit area).

For the II-CVD geometry, $H\,N_V$ is simply equal to N_A since the cross-section is constant throughout the thickness (H) of the sample. It is also instructive to review Fullman's analysis for the general case with randomly oriented columns. Here, J is the component of rod length perpendicular to the sample plane and θ is the angle with respect to the column axis:

$$J = H\cos\theta$$

Now, the number of rods per unit area (N_A) on the cross-section is equal to the number of rods per unit volume (N_V) multiplied by the probability that a single randomly positioned and oriented rod is cut by the plane. In other words, N_A is equal to N_V times the mean value of J, averaged over all possible rod orientations. But the columns in the II-CVD microstructure are perpendicular to the plane and θ is equal to zero. Hence,

$$H N_V = N_A$$

Therefore, by substitution:

$$r = \frac{1}{2}\frac{N_L}{N_A} \qquad [3.2]$$

Thus, the average radius is expressed in terms of two metrics derived from plan view sections of the microstructure.

3.3.2 Volume fraction

A function of N_L and N_A also determines the volume fraction of (copper) columns in the microstructure. The volume fraction is equal to the number per unit volume (N_V) times the average volume of a column (V), and the number per unit (N_A) area times the average area in cross-section (A):

$$N_V V = N_A A$$

Employing the appropriate substitutions from equations [3.1] and [3.2] yields the following expression for volume fraction (f):

$$f = \frac{\pi N_L^2}{4N_A} \quad [3.3]$$

3.3.3 Interface Area per Unit Volume and Mean Free Path

N_L and N_A yield additional information about the microstructure. Smith and Guttman derived a simple relationship between the interface are per unit area (S_V) and N_L, which is independent of geometry and distribution of the phase:[53]

$$S_V = 2N_L$$

Similarly, the mean free path (λ) is independent of shape and distribution of the phase:

$$\lambda = \frac{1-f}{N_L}$$

3.3.4 Validity of Quantitative Analysis

The quantitative analysis used ten by eight inch prints of TEM plan view micrographs at 300,000 X magnification. Manual point counting determined N_A. Columns that intersected the edge of the photograph were treated according to standard practice in quantitative metallography: any column that intersected an edge was counted as one half.[54] This minimized any bias towards either large or small columns. A field represented an area of only 0.549 μm^2 even though it

contained over 2000 columns, so it was important to maintain accuracy while minimizing the tedium of counting columns.

An experiment determined that the 95 % confidence limit (reported as % relative accuracy) of four measurements on one field due to human error (±0.8%) was slightly higher than that of the average measurements on four different micrographs (±0.5 %). This is unusual for metallographic samples; it reflects the high degree of uniformity of the microstructure and the large number of columns contained in one field. The 95% confidence limit of sampling the same field three times was ±1%. Therefore, an average of three measurements on one field was sufficient to determine N_A while taking great care in selecting fields that did not contain any artifacts. Ideally, software could have automated the counting process but available software packages did not have adequate artificial intelligence to determine boundaries of columns. Diffraction contrast in the TEM micrographs yields an extended range of grayscale levels in a digitized image.

Overlaying a transparency grid with 14 gridlines on the eight by ten inch photograph and measuring the number of intersections along the length of a gridline determined N_L. The process also counted columns that intersected the edge of the photograph as one half. The photograph was viewed at 10 X magnification using a magnifying eyepiece in order to accurately determine the number of intersections. Tangential intersections with the gridlines counted as one half.[54] The 95% confidence limit for N_L was ±1 to 3% with the smaller diameter columns and uniform distribution of room temperature II-CVD being represented in the lower half of this range.

The accuracy of the analysis relies on how closely the II-CVD microstructure resembles idealized columns. At relatively low temperatures (below 61°C) the microstructure is very uniform and the columns have approximately circular cross-sections in plan view TEM. (Figure 3.4.) Closer inspection reveals that there are pairs of columns that appear to have grown together forming either

oval or "dumbbell" cross-sections. (For example, Figure 3.12.) These structures were counted as two columns. From the perspective of trying to explain the microstructure evolution it behooves one to preserve the "identity" of two columns that formed at the start of the growth process. Merging of two columns was an exception rather than the rule: it represents a case where the center-to-center distance between two evolving columns is less than the characteristic diameter for the columnar microstructure.

At 61°C the microstructure enters a transition regime where the regular arrays of columns appear to be breaking down. With reference to the microstructure at slightly higher temperatures, it is clear that this is a transition regime where columns are starting to merge. (Figure 3.12.) Again, the counting (N_A and N_L) still accounts for "original" columns but it is clear that the quantitative analysis is going to be more inaccurate at higher temperatures.

At higher temperatures, the microstructure regains uniformity but the columns are not only larger but they are also closer packed. From simple geometry, a close packed array of columns of uniform radius has a volume fraction of 0.906. (See Appendix A.) The volume fraction of copper columns exceeds this value at higher deposition temperatures. Another weakness of the volume fraction analysis is having N_L to the second power, which increases the sensitivity to error.

3.3.5 Volume Fraction by Point Counting

Conventional point counting (ASTM specification E562) was adopted as an alternate technique in determining volume fraction.[54] The process used a transparency grid with 270 intersections (points) and counted the number of points that did not lie on a column. The fraction of points translates directly to a volume fraction. The number of points on the grid was greater than standard practice; this choice was due to the relatively low concentration of the minor

phase and a desire to minimize the number of fields.[54] An important metallographic counting rule is to make the grid size large enough to avoid multiple points on a single feature. In this case, it was a one-half inch grid spacing (42 nm at 300,000X magnification), which was larger than the average column diameter for all samples. It is very important not to shift the grid during counting because systematic spacing of grid points has been shown to be more effective statistically than random sampling.[54]

In order to maintain a high level of accuracy, the number of repetitions was not fixed but depended on achieving a 95% confidence limit below 2%. However, the minimum number of repetitions was set at four, which usually brought the 95% confidence limit below 1% for uniform, low temperature microstructures.

3.4 Microstructure Evolution: Ion-Flux-Limited Regime

The work presented in this section focuses on the *ion-flux-limited regime*. With reference to Figure 3.2, 0.5 mtorr was chosen as the default precursor pressure, which corresponds to an equivalent gas flux of 5.5×10^{16} molecules/second. Exploratory experiments showed that doubling the precursor flow did not affect the microstructure. Experiments investigated the effect for a range of growth rates – determined by the ion flux – at various temperatures between 25°C and 100°C. The default ion beam voltage was 500V and the plan view transmission electron micrographs (TEM) were 500 Å thick.

Figure 3.4 and Figure 3.5 show the characteristic microstructure of II-CVD at 25°C and 500V for a range of growth rates. The XTEM (cross-section transmission electron micrograph) shows that the microstructure is in fact columnar. (Figure 3.6.) Note that the density of the columns appears to be higher in cross-section; this is because the image typically represents a projection of a

few layers of columns. There is not any discernible difference in diameter associated with a change in growth rate. Quantitative analysis verifies that the diameter remains constant at approximately 14.5 nm. However, the microstructure at high growth rate (1 Å/s) has what appears to be "channels", and certain junctions stand out as being lighter than other regions. There is also some elongation of the columns adjacent to the light regions in plan view, which suggests that the columns are not perpendicular to the plane. The XTEM (Figure 3.6) shows how these features arise: notice how the columns grow perpendicular to the substrate, but imperfections will give rise to columns that do not grow exactly parallel to the others. As discussed earlier, the time averaged precursor surface coverage is lower at higher growth rates. This increases the probability of surface sputtering at the initial growth stage, which roughens the substrate and columns start to grow at an angle to the plane. The microstructure in Figure 3.7 is from a high growth rate experiment that was aborted due to a problem with the ion gun. Clearly, the surface coverage is incomplete, as the film has not started to grow in some spots. The characteristic microstructure will quickly cover the entire substrate, but this initial structure introduces additional boundaries that stand out as channels through the fully developed plan view microstructure.

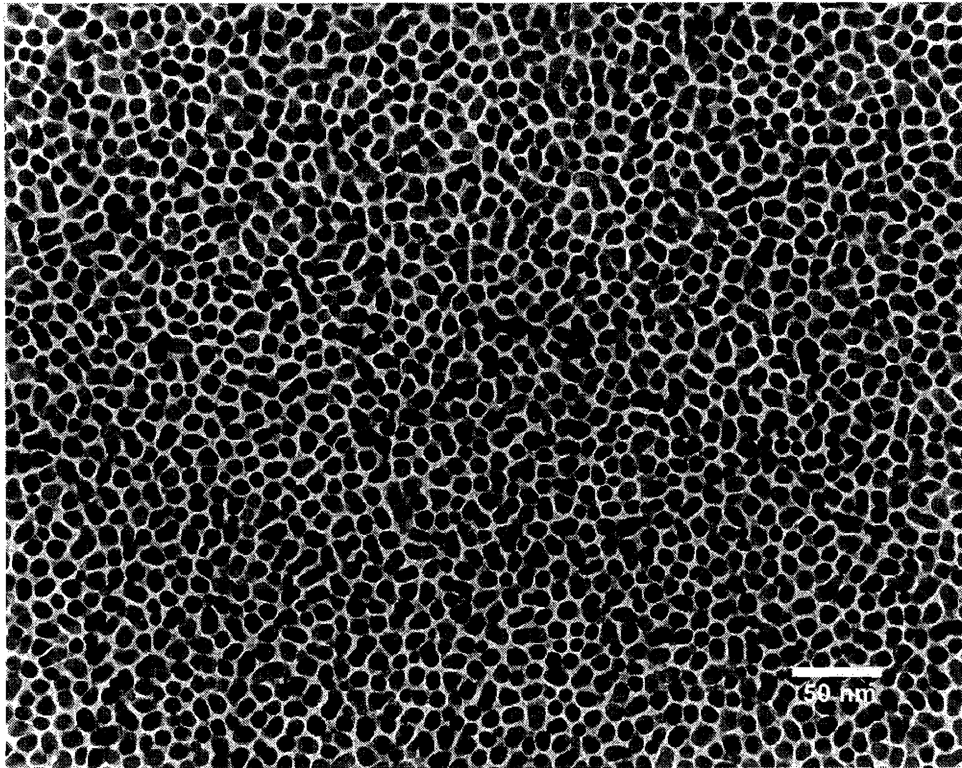

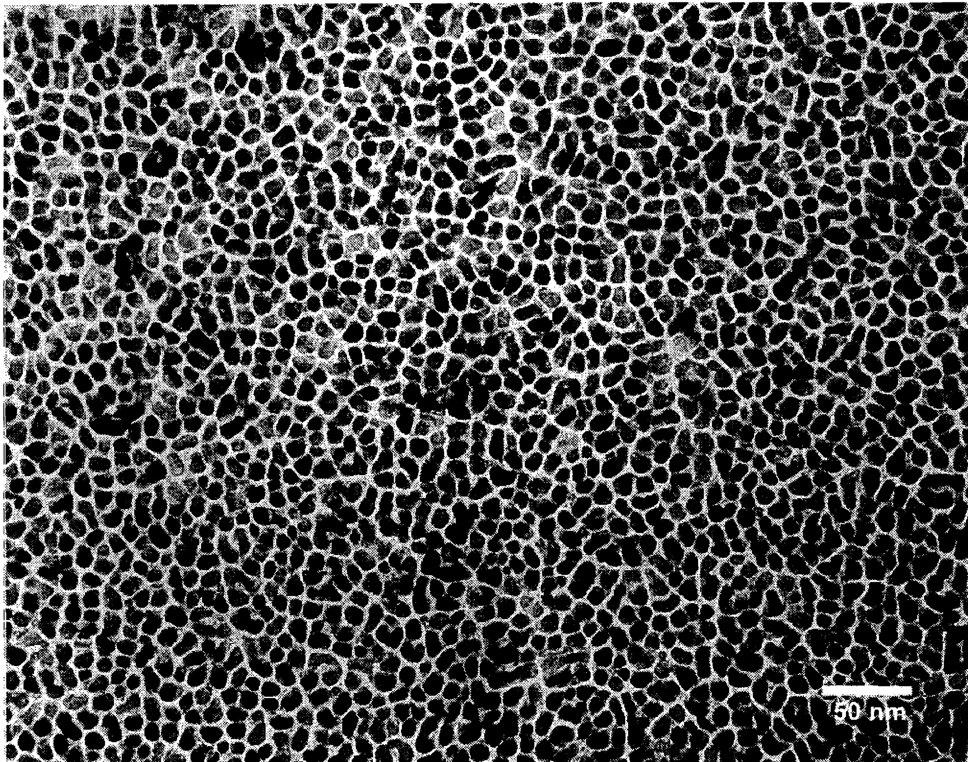

Figure 3.4: Microstructure at 25°C, 500V and 0.5 mtorr precursor gas pressure. Top: 0.1 Å/s. Bottom: 0.3 Å/s.

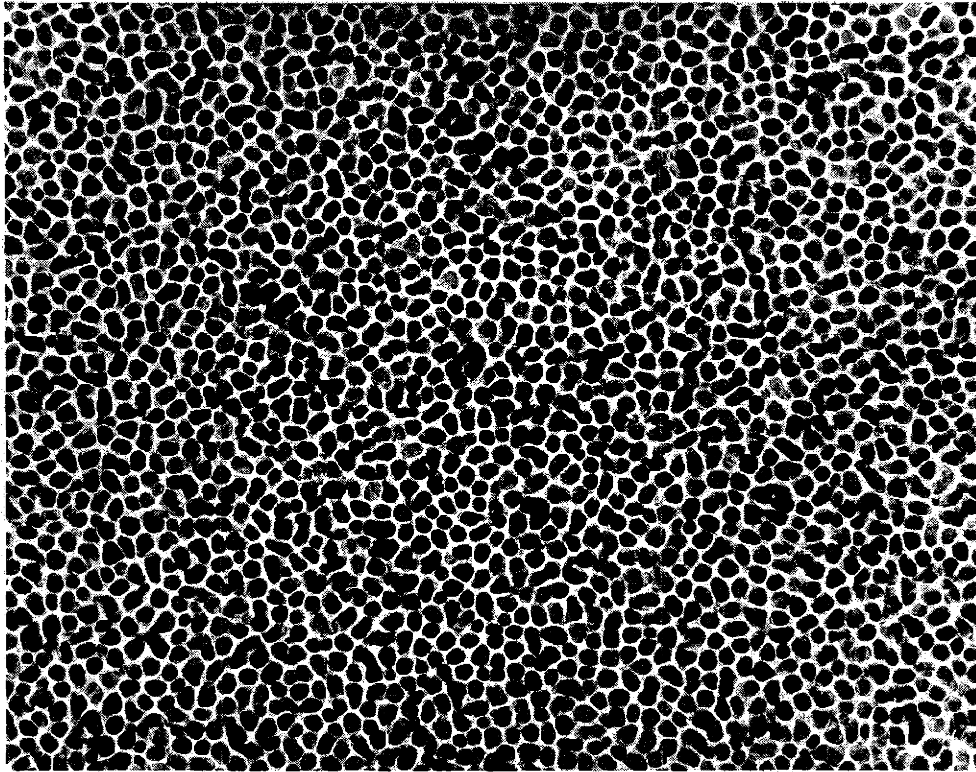

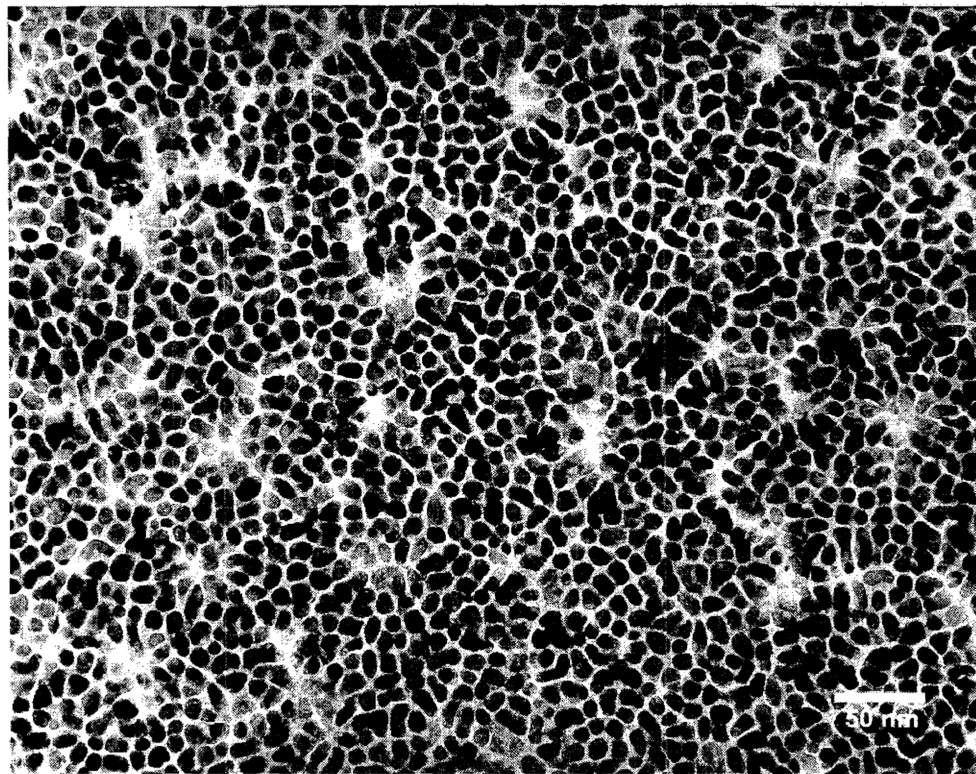

Figure 3.5: Microstructure at 25°C, 500V and 0.5 mtorr precursor gas pressure. Top: 0.5Å/s. Bottom: 1 Å/s.

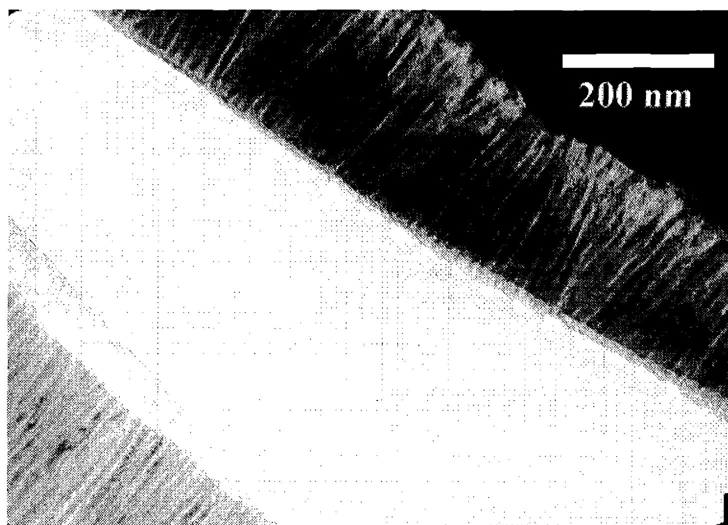

Figure 3.6: XTEM at 25°C, 500V and 1 Å/s. 2500 Å thick. Two films are glued together; the white region in the center of the micrograph is where the epoxy used to be. The light gray film on top of the columnar II-CVD film in the left bottom corner is an epoxy remnant. The II-CVD film is lighter in this region because it is thinner than the opposing film.

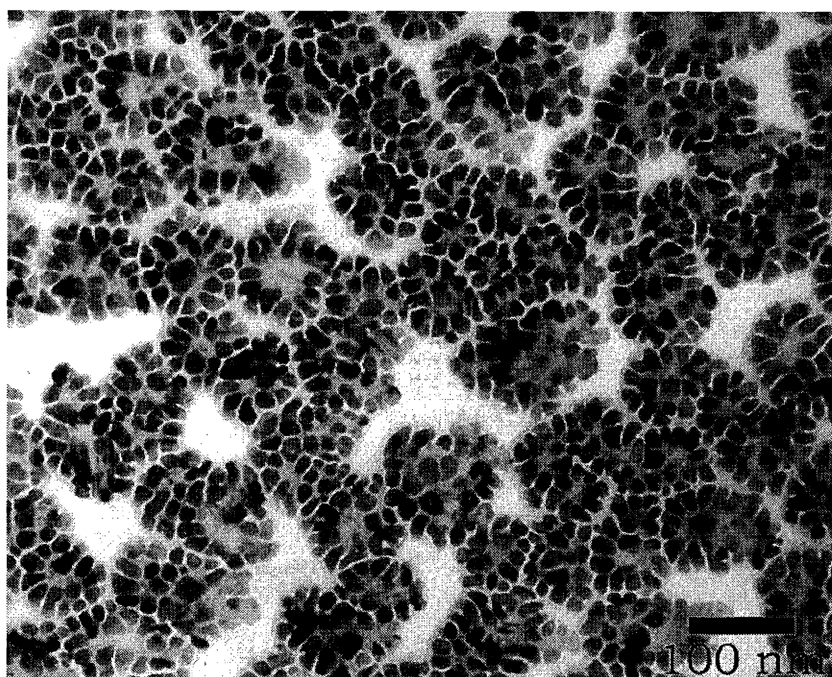

Figure 3.7: Incomplete substrate coverage. Experiment was terminated due to problem with ion gun. Deposition at 25°C, 500V, and nominally 1 Å/s.

The same pattern develops at 43°C (Figure 3.8 and Figure 3.9) and 51°C. The column diameter increases with the substrate temperature but, again, quantitative analysis verifies that the growth rate has no effect on the column diameter. However, the "channeling" and "light spots" appear already at 0.5 Å/s at these temperatures. At 61°C the trend continues for the range between 0.2 and 1 Å/s, although it is now apparent that the volume fraction of copper columns also increases with temperature – compare Figure 3.10 with the microstructure at 25°C. The columns also appear to fuse at, for example 1 Å/s, and form "dumbbells" or elongated structures. However, the microstructure at 0.1 Å/s and 61°C appears to be quite different. The column diameter is no longer as uniform; the large columns are in fact products of several columns merging. Quantitiative analysis indicates that the average column diameter is slightly larger than the higher growth rate conditions at this temperature.

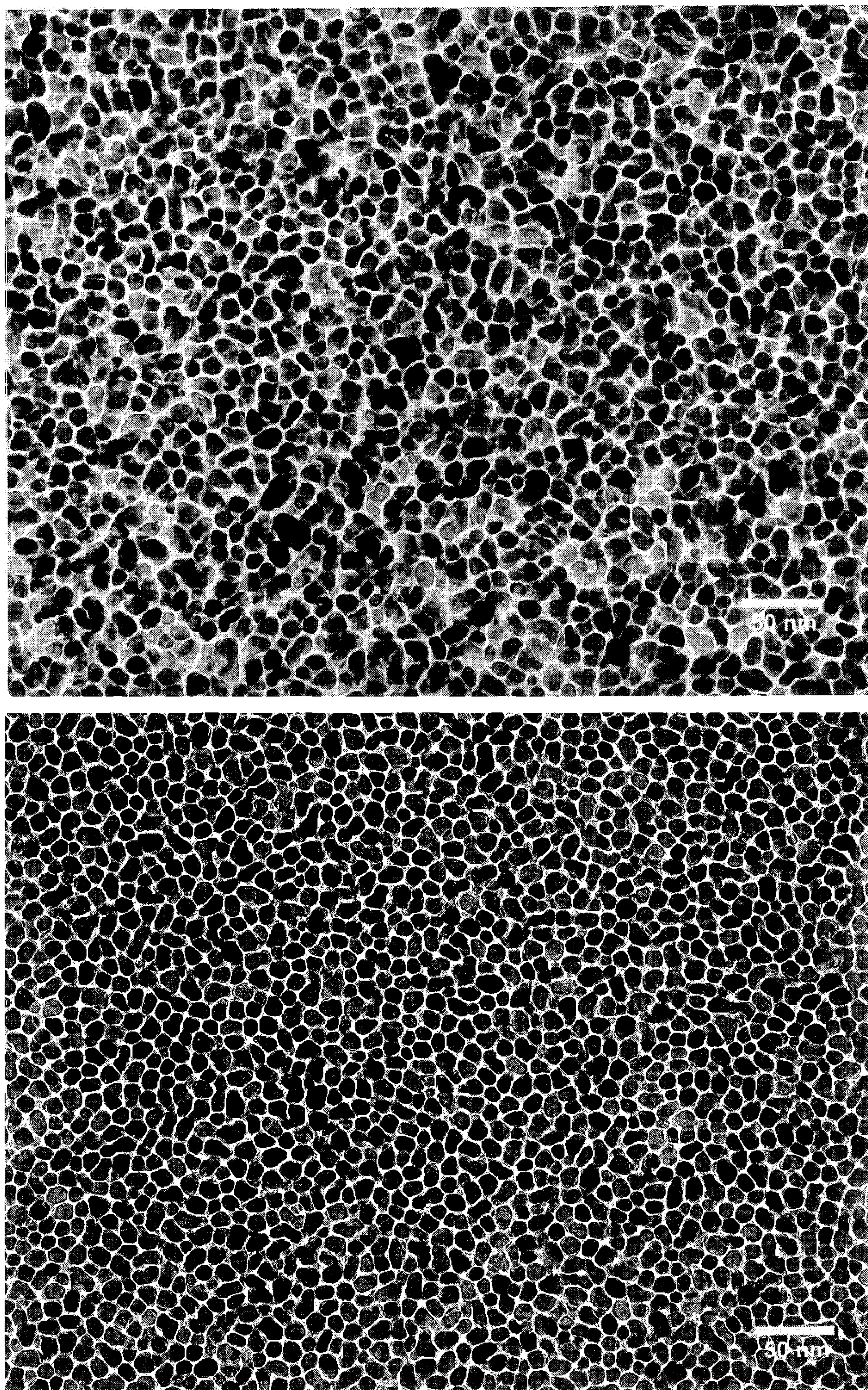

Figure 3.8: Microstructure at 43°C, 500V and 0.5 mtorr precursor gas pressure. Top: 0.1Å/s. Bottom: 0.3 Å/s. The micrograph at 0.3 Å/s has lower contrast because the imaging used a larger SAD aperture.

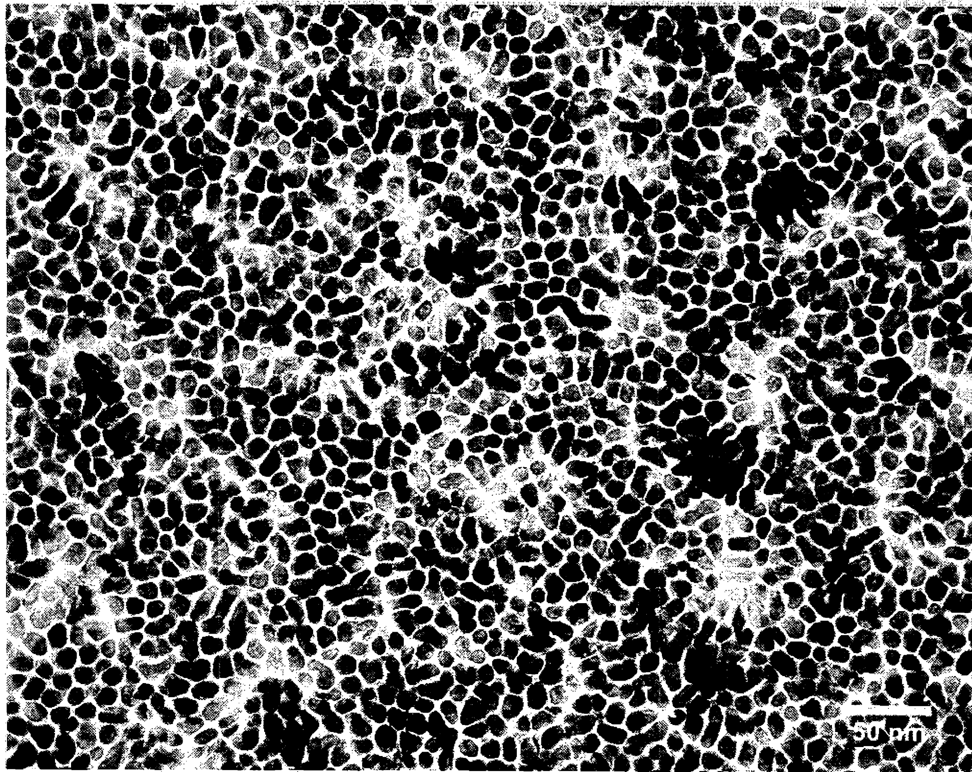

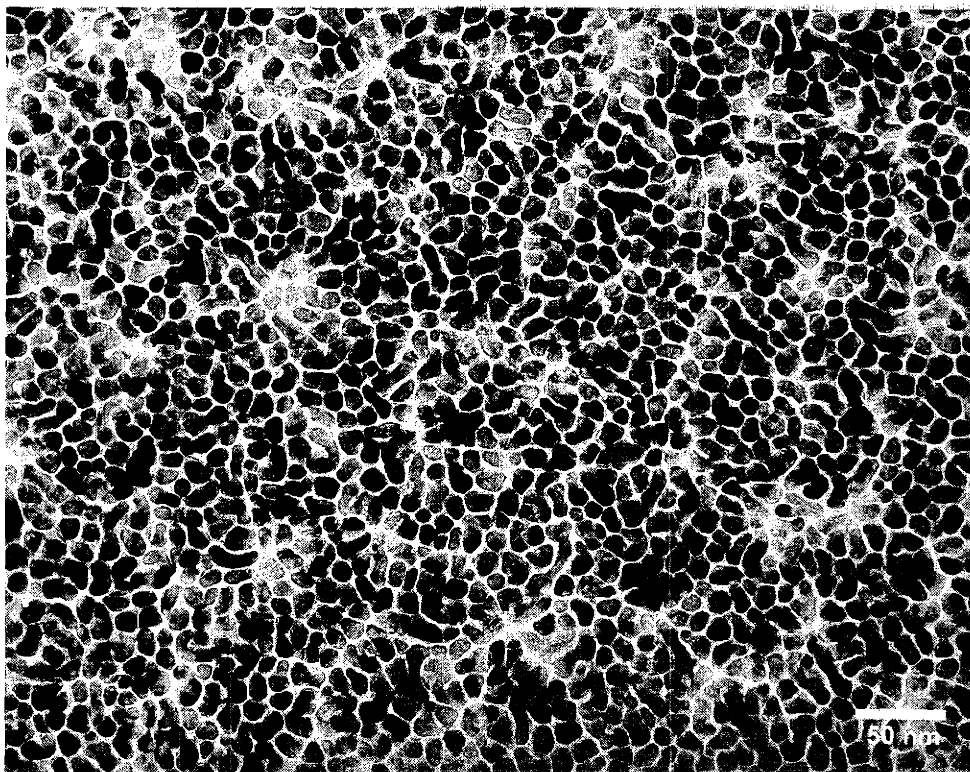

Figure 3.9: Microstructure at 43°C, 500V and 0.5 mtorr precursor gas pressure. Top: 0.5Å/s. Bottom: 1 Å/s.

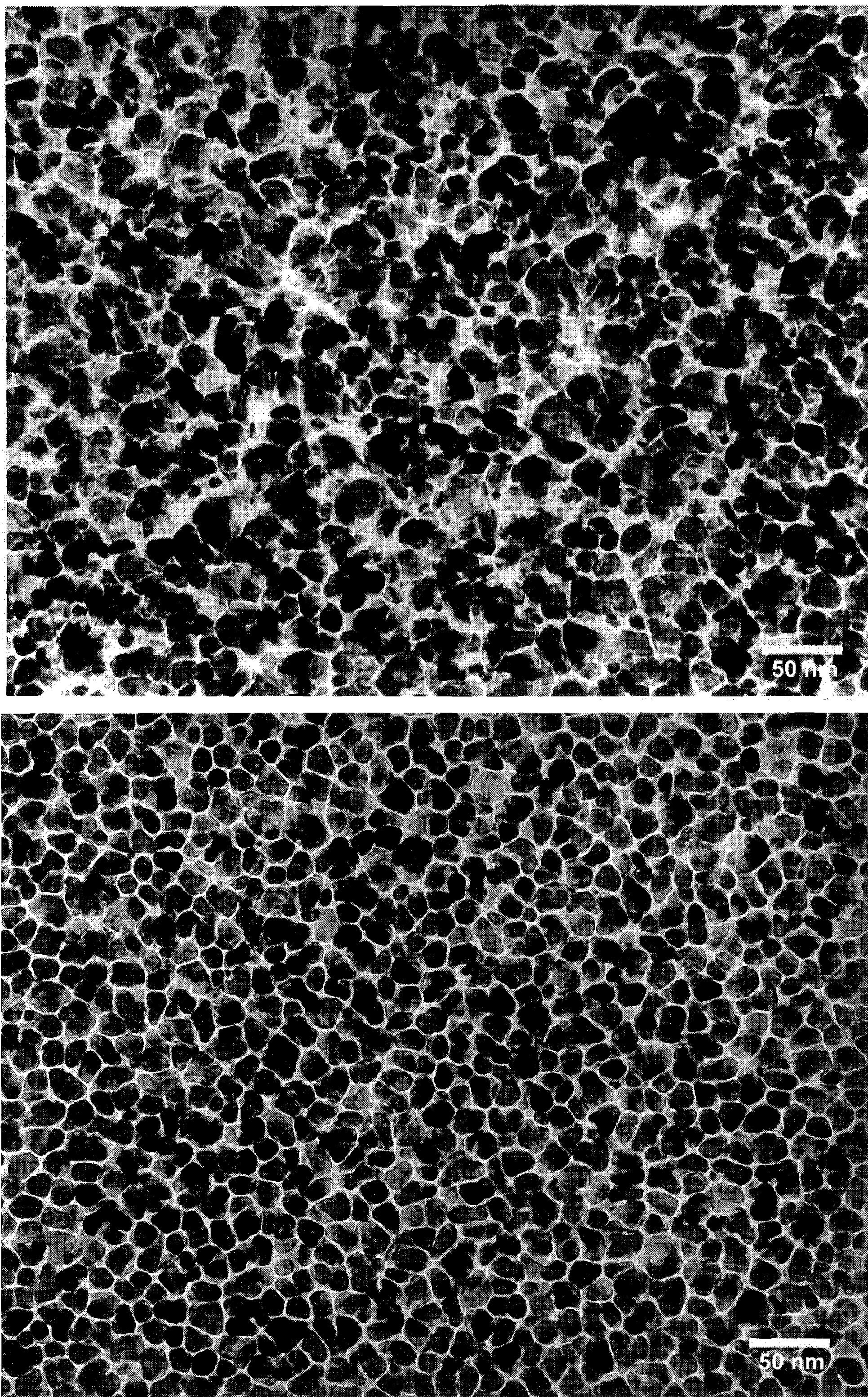

Figure 3.10: Microstructure at 61°C, 500V and 0.5 mtorr precursor gas pressure. Top: 0.1Å/s. Bottom: 0.2 Å/s.

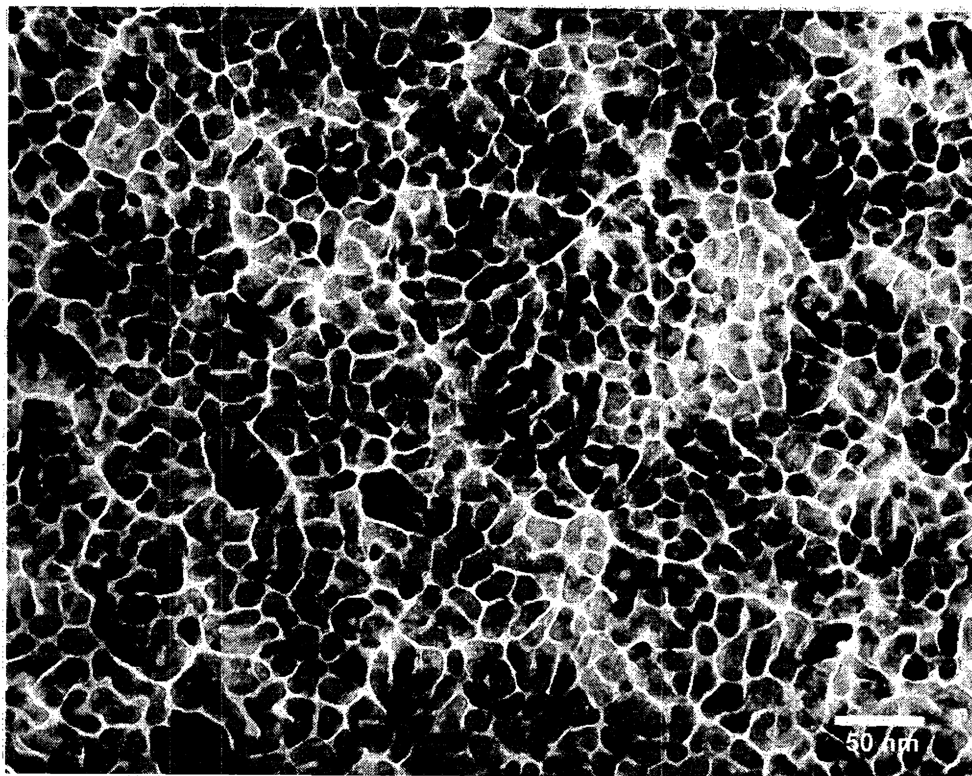

Figure 3.11: Microstructure at 61°C, 1 Å/s, 500V and 0.5 mtorr precursor gas pressure.

At 71°C and high growth rate (Figure 3.12, bottom) the "dumbbells" and elongated structures also appear. The low growth rate (0.13 Å/s) has much larger columns that now appear to be more polygonal than round in cross-section. Even though the beam current (0.9 $\mu A/cm^2$) is *lower* than what is required for 0.1 Å/s growth at 25°C (1.3 $\mu A/cm^2$), the minimum growth rate at 71°C is 0.13 Å/s. This is because the growth process is no longer purely ion driven – pyrolysis or thermal CVD starts to operate at this temperature. The ion gun will not operate at an ion beam current lower than ~1 $\mu A/cm^2$ because the discharge in the ion gun becomes unstable and extinguishes.

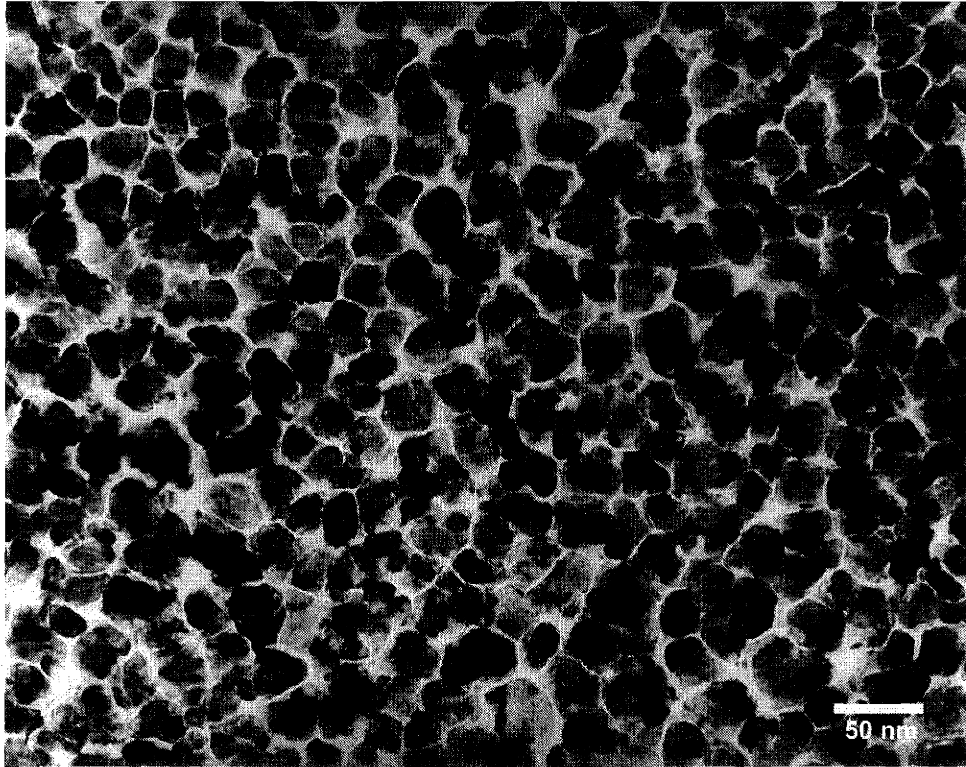

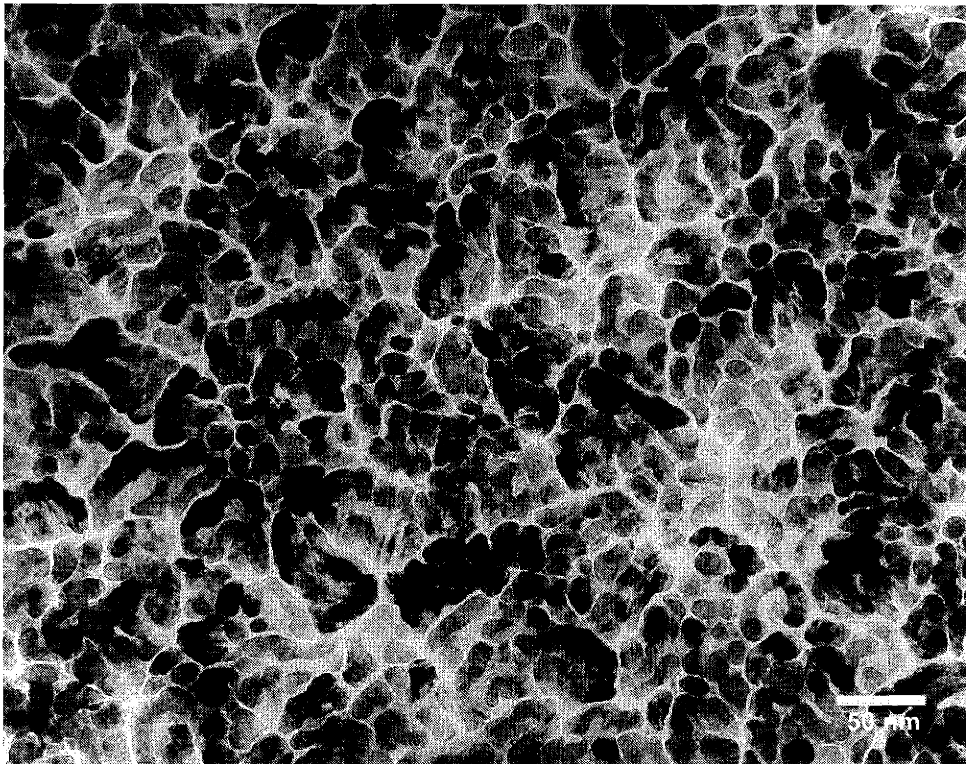

Figure 3.12: Microstructure at 71°C, 500V and 0.5 mtorr precursor gas pressure. Top: 0.13 Å/s. Bottom: 1 Å/s.

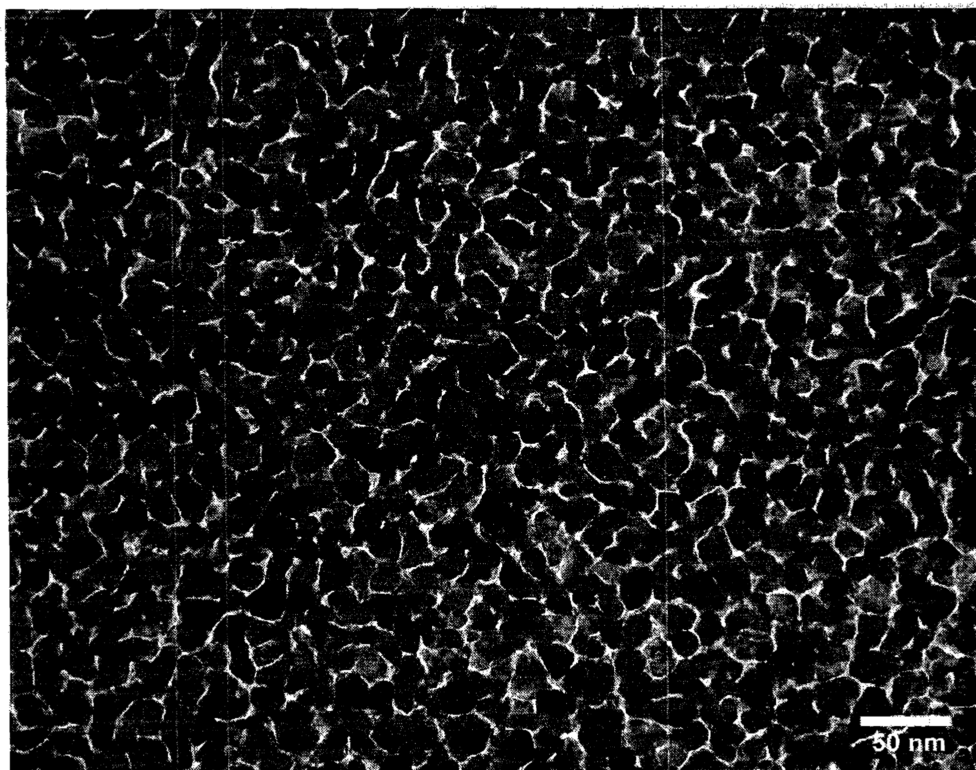

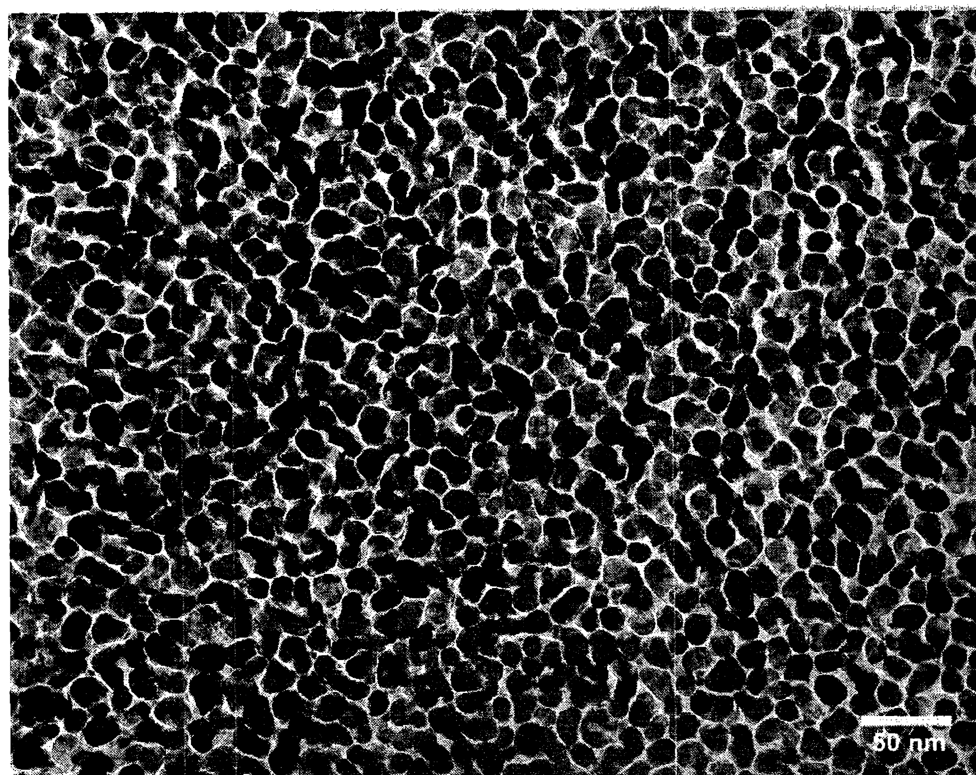

Figure 3.13: Microstructure at 79°C, 500V and 0.5 mtorr precursor gas pressure. Top: 0.2 Å/s. Bottom: 1 Å/s.

At 79°C the minimum growth rate has increased to 0.2 Å/s at 1 $\mu A/cm^2$. The microstructure (Figure 3.13, top) is considerably denser compared to the higher growth rate (Figure 3.13, bottom) and most columns impinge on their neighbors. The column diameter also appears to be slightly larger. Again, this is ascribed to a thermal CVD component. XTEM verifies that the microstructure is still columnar at this temperature and growth rate. Then the minimum deposition rate reaches 0.8 Å/s at 100°C. (Figure 3.14.) A continuous microstructure is starting to form. Some boundaries even resemble equilibrium triple junctions; residual carbon is found at – without misusing the term – the grain boundaries. However, the XTEM (Figure 3.15) shows that the microstructure remains columnar. Detailed discussion of the synergism between thermal CVD and II-CVD is deferred until Chapter 4.4.

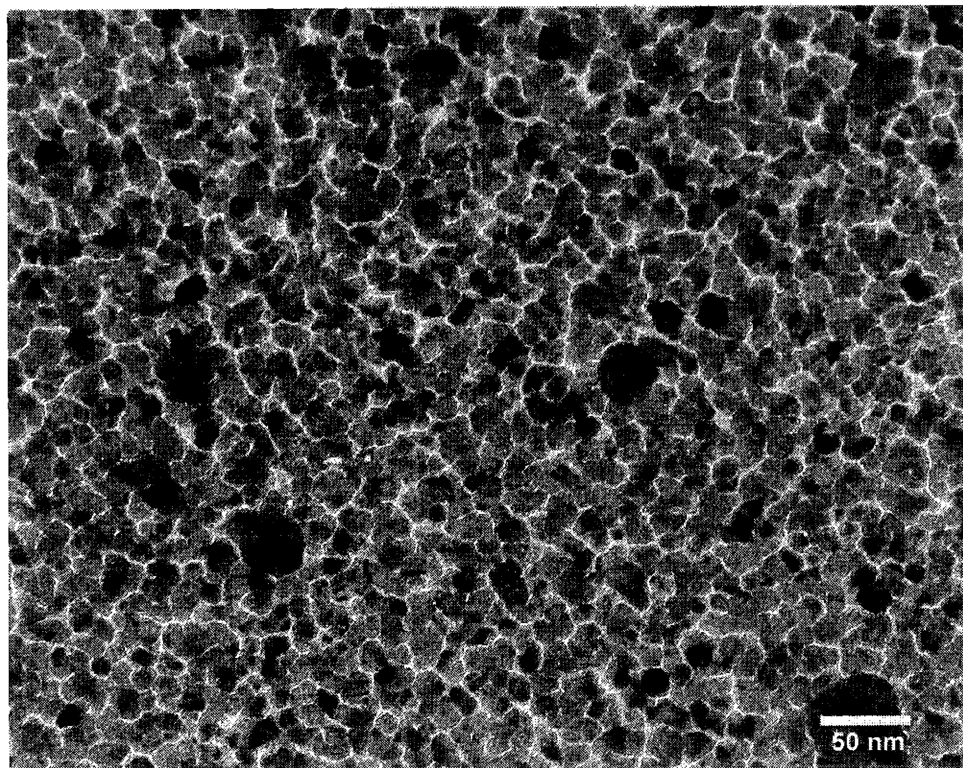

Figure 3.14: Microstructure at 100°C, 0.8 Å/s, 500V and 0.5 mtorr precursor gas pressure.

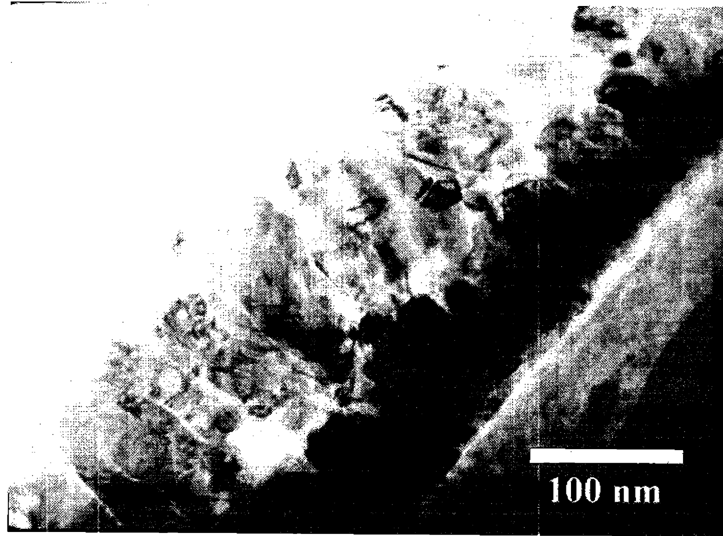

Figure 3.15: XTEM. Top layer deposited at 93°C; bottom layer deposted at 100°C. Ion beam voltage of 500V and deposition rate of 0.8 Å/s for both runs.

Figure 3.16 summarizes the data from quantitative analysis of the ion-flux-limited regime where there is no contribution from thermal CVD. 61°C defines the boundary where thermal CVD is just starting to play a role in the deposition process. At this temperature, 0.1 Å/s has a larger column diameter than higher growth rates, but the qualitative impression of the magnitude deceives the eye. Remember that the quantitative analysis accounts for columns that appear to have merged.

Overall, the quantitative analysis verifies that the column diameters at a fixed deposition temperature are independent of growth rate. (Figure 3.16.) On the other hand, higher temperatures produce significantly larger column diameters at low growth rates; here, II-CVD no longer dominates the deposition process. (Figure 3.17.) The quantitative analysis becomes very difficult at 71°C because the microstructure is quite irregular, as it appears to be in a transition state; hence, the larger error bars. As discussed earlier, the quantitative analysis is also inaccurate at 79°C and 100°C as the microstructure becomes more polygonal and continuous. However, the error is systematic. For example, the 0.5

Å/s and 1.0 Å/s microstructures at 79°C appear to be identical and the quantitative analysis also show this; however, the absolute measurement is probably not accurate.

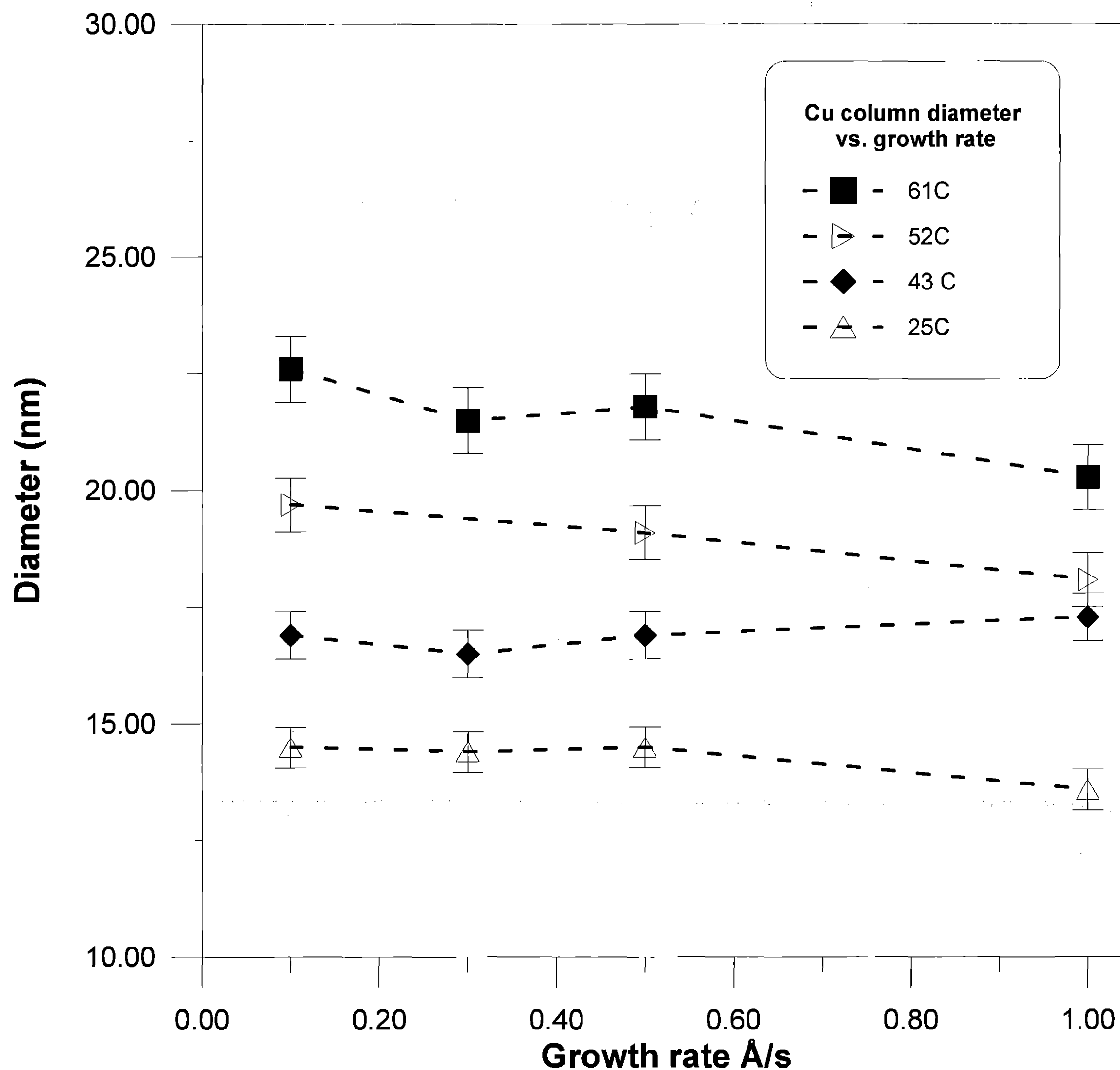

Figure 3.16: Column diameter versus growth rate in the ion flux limited regime. This range of temperatures corresponds to exclusively ion-induced CVD.

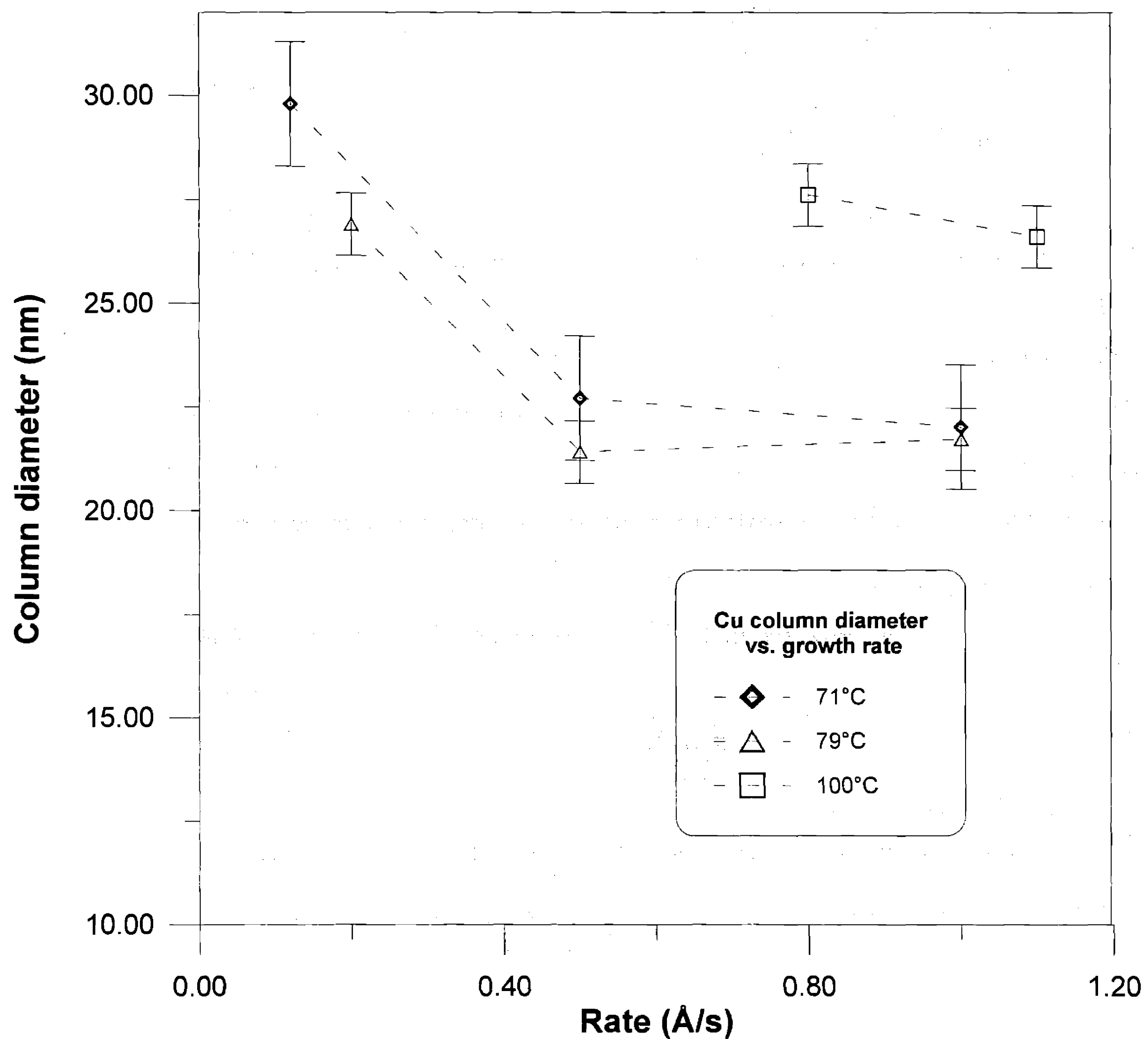

Figure 3.17: Column diameter vs. growth rate in the ion flux limited regime at higher temperatures.

3.5 Microstructure Evolution: Gas Flux Limited Regime

The experiments examined the gas-flux-limited microstructure evolution at 27°C, 43°C and 79°C. Figure 3.18 is an example of a rate experiment that serves as a guideline for determining appropriate conditions for microstructure analysis in the gas flux limited regime. The X's correspond to the actual growth rate and ion flux of the microstructure runs at 43°C. Unlike the ion flux limited regime, the column diameters vary with ion flux.

At 43°C and 7 $\mu A/cm^2$, the column diameter (19.8 nm) is significantly greater than the ~17 nm average of ion flux limited microstructures at the same temperature. (Figure 3.19.) This experiment's ion flux is relatively low so the deposition rate has not reached the limit determined by the gas flux. (See Figure 3.18.) The gas flux limited regime tends toward higher carbon incorporation but this deposition condition retains a relatively low carbon fraction. On the other hand, the ion flux to growth rate ratio is two or three times greater as compared to the ion flux limited regime. *This suggests that an ion-enhanced surface diffusion process influences the characteristic copper column diameter.* Chapter 4 explores this phenomenon in detail.

The column diameter decreases with increasing flux. Evidently, the increasing carbon incorporation negates any ion-enhanced surface diffusion. Consider the microstructure at 43°C and 29.1 $\mu A/cm^2$. (Figure 3.19.) The poor image quality is due to the high sputtering rate and the associated substrate damage. Even though the surface coverage of the columns does not appear to be particularly dense, many columns appear to be merging with their neighbors. The average has dropped to 14.4 nm. Figure 3.20 shows that other temperatures exhibit a similar trend.

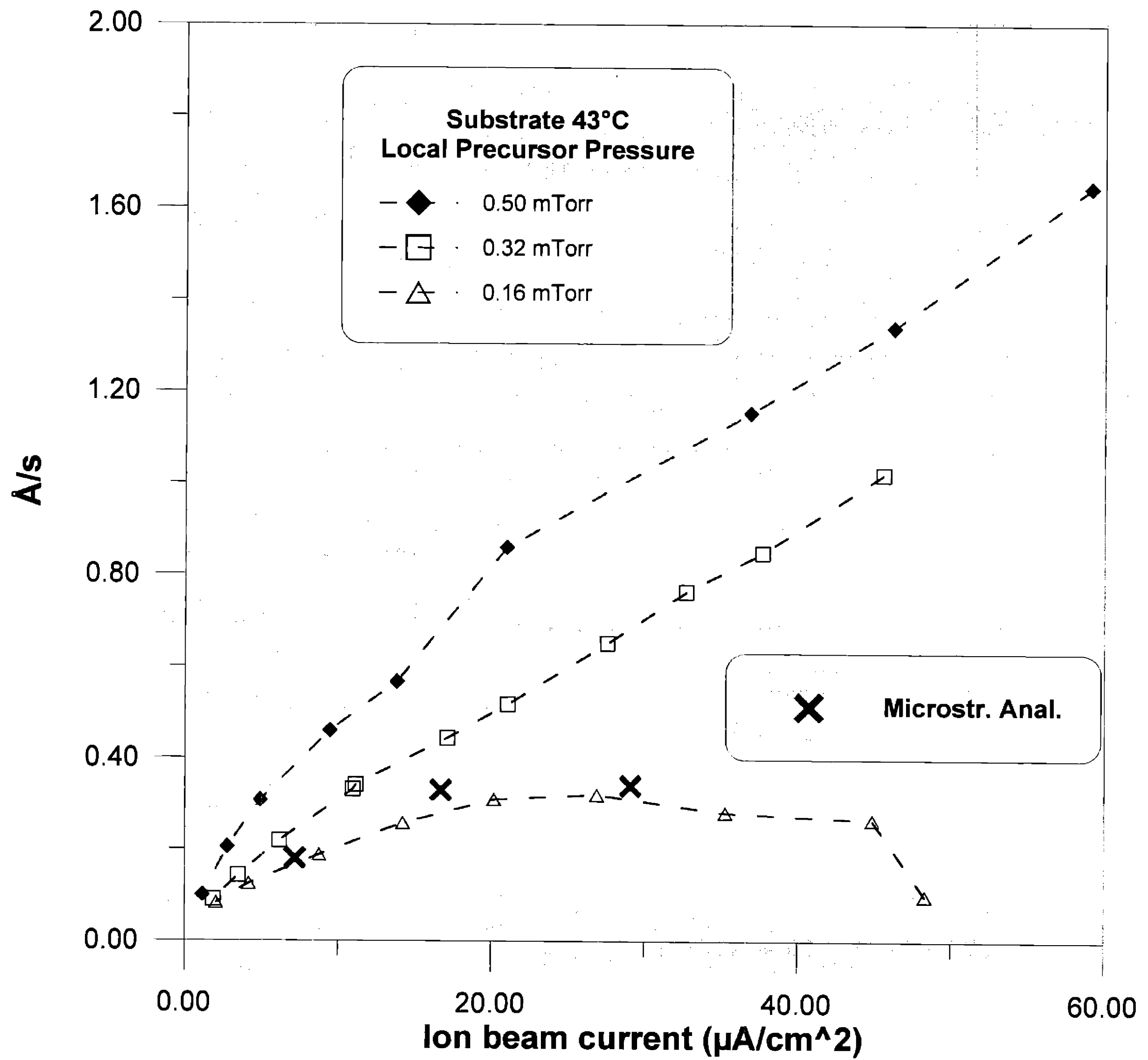

Figure 3.18: Rate experiments performed to pinpoint the gas-flux-limited regime. The X's indicate the rate and ion flux used in three "gas-flux-limited" microstructure analysis experiments.

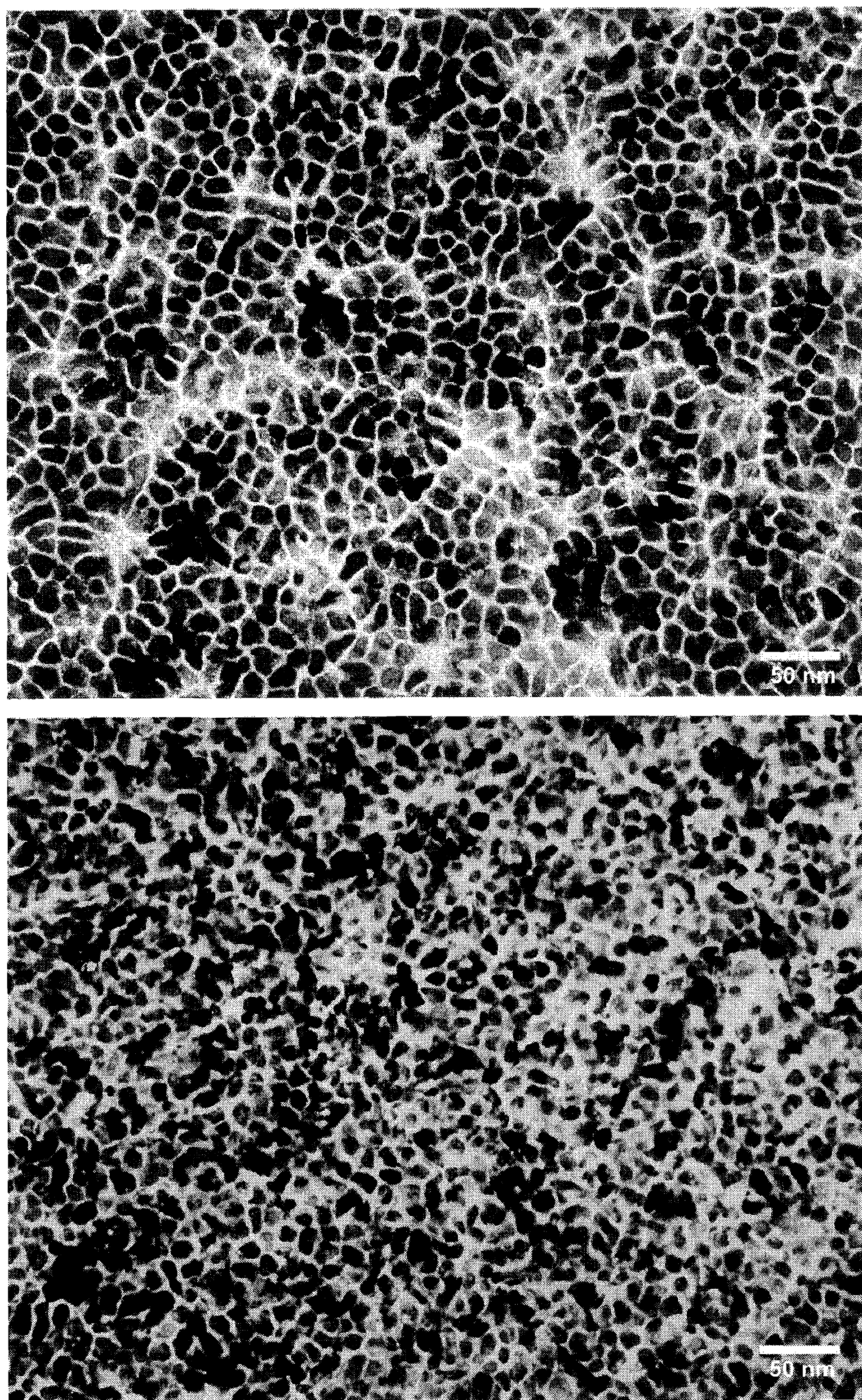

Figure 3.19: Microstructures in the gas flux limited regime at 500V, ~0.15 mtorr local gas precursor pressure. Top: 7 μA/cm2 ion flux and 0.18 Å/s. Bottom: 29 μA/cm2 ion flux and 0.34 Å/s.

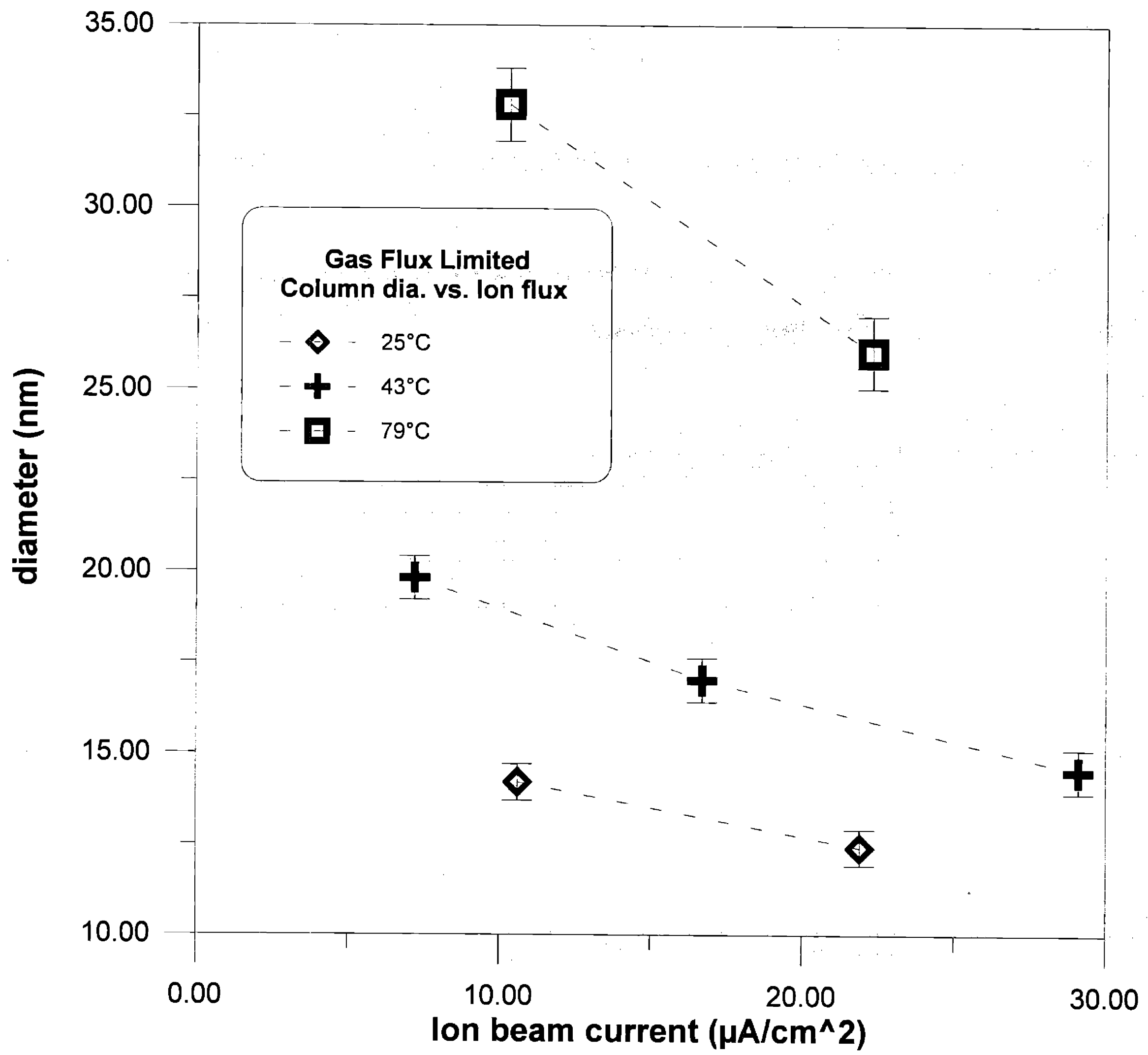

Figure 3.20: Column diameter versus ion flux in the gas flux limited regime.

3.6 TEM Diffraction

Indexing the selected area diffraction (SAD) pattern (Figure 3.21) verifies that the films do in fact contain FCC copper. The ratio of ring radii scale as $3^{1/2}:4^{1/2}:8^{1/2}:11^{1/2}:12^{1/2}:16^{1/2}$, etc., which is the characteristic sequence for FCC where the rings correspond to the {111}, {200}, {220}, {311}, {222}, {400} families of planes, respectively. The lattice spacing (*d*) is determined from $Rd = L\lambda$, where R is a ring diameter and $L\lambda$ is the product of the camera length and electron wavelength, also known as the camera constant. The lattice parameter is determined by multiplying *d* by $(h^2+k^2+l^2)^{1/2}$ where (hkl) corresponds to the chosen ring. The lattice parameter of this SAD pattern is 3.6 nm, which confirms that the FCC element is copper.

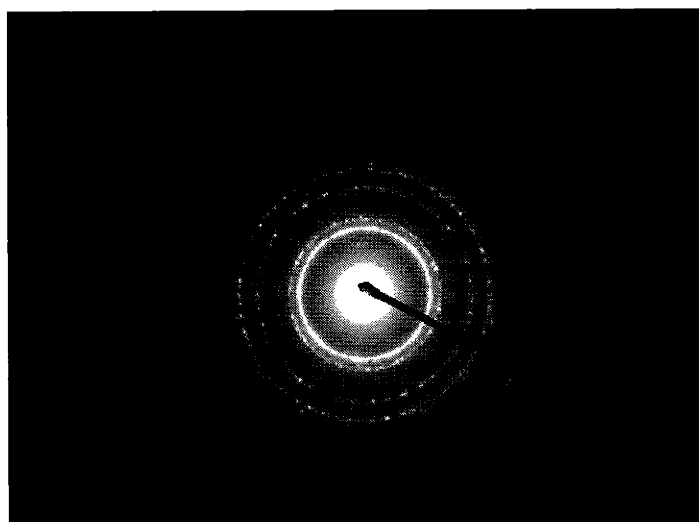

Figure 3.21: Diffraction pattern. 500V, 25°C and 0.5 Å/s deposition.

Columnar thin film structures usually exhibit preferred orientation with the most densely packed planes parallel to the substrate surface. Surface energy minimization probably accounts for this texture.[55] However, here the columns orient themselves randomly about the azimuthal direction, so SAD forms continuous rings if there are sufficient columns within the selected area. Figure 3.21 suggests that there is some degree of texture because the innermost {111}

ring appears to be much brighter than the outer rings. The {111} family of planes have maximum packing density for FCC symmetry. The diffraction patterns of the II-CVD films do not change significantly with deposition conditions, although the diffraction rings for films grown at high temperature are slightly more "grainy" due to the larger column/ grain size. XTEM diffraction patterns also contain fewer spots because a cross-section images fewer columns. The SAD aperture was at its minimum setting (approximately 1 μm), which obviously requires very fine microstructure to produce continuous diffraction rings. The carbon in the II-CVD films does not produce any diffraction pattern, which suggests that it is in fact amorphous. However, some XTEM samples do have weak additional rings in their diffraction patterns that index as graphitic carbon. This is ascribed to contamination from the ion milling process since it is not observed in plan view samples, which are not ion milled. A diffusion pump evacuates the Gatan ion miller that is used for sample preparation, and graphitic lubricants may be present in the system. Other users of the same ion milling equipment reported similar problems with carbon contamination.[56]

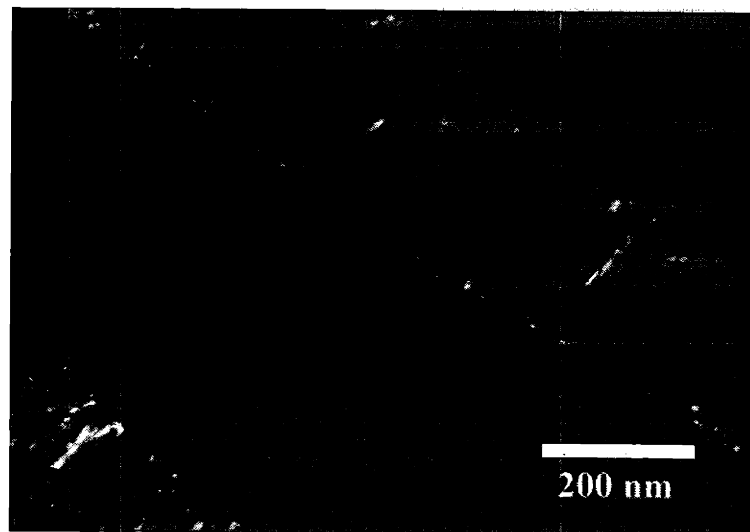

Figure 3.22: Dark field XTEM. 2500 Å thick at 25°C, 500V and 1 Å/s growth rate. The XTEM has two films face-to-face, separated by an epoxy layer.

Dark field imaging captures the diffracted beams that pass through the objective aperture. Tilting the sample or ion gun illuminates columns as the diffracted

electron passes through the objective aperture. Dark-field XTEM examines the continuity of crystal orientation. Figure 3.22 illustrates that some columns that do maintain the same orientation for extended lengths over the cross-section but this is an exception rather than the rule. Figure 3.23 shows the microstructure of a ~3200 Å thick film grown at 71°C and 1.0 Å/s. It is hard to determine if the columns are single crystal. In any case, the columnar growth appears to be quite faulted. This could be due to a combination of the low temperature, sputtering effects, and the carbon rejection process.

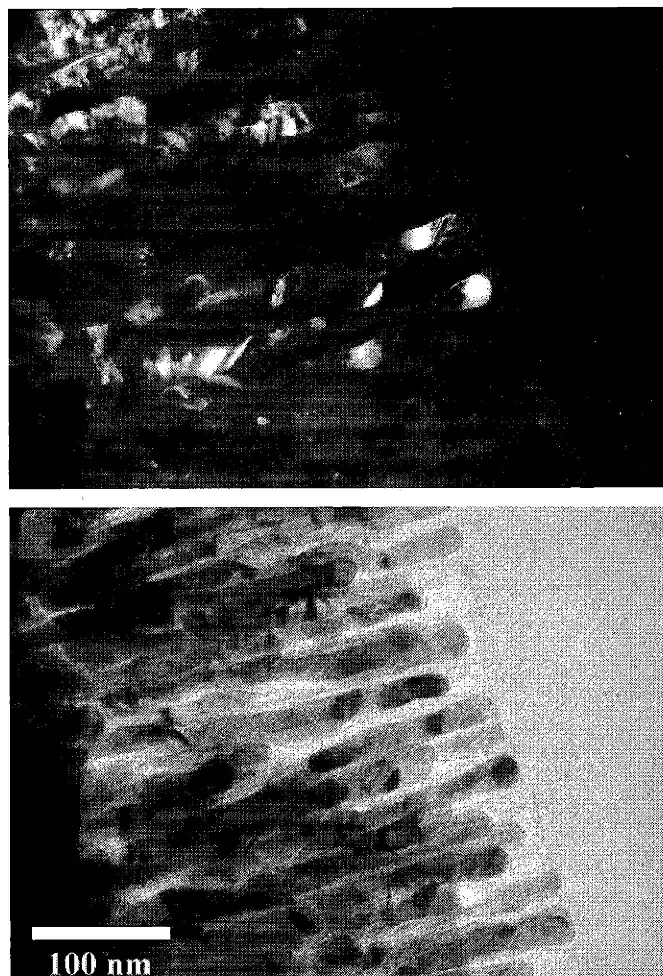

Figure 3.23: Dark field (top) and bright field (bottom) XTEM: 3200 Å thick at 71°C, 1.0 Å/s and 500 eV. The objective aperture selects a portion of the {111} ring.

3.7 H-atom assisted II-CVD

H-atom beam assisted II-CVD effectively removes the carbon and produces the equiaxed microstructure shown in Figure 3.24. XPS analysis did not detect a carbon peak, so 99.9 atomic % copper represents a conservative estimate of minimum purity. Trace analysis would require secondary ion mass spectroscopy (SIMS). The top micrograph in Figure 3.24 is difficult to interpret because the TEM images through multiple layers of crystallites as the electron beam passes through 500 Å of film. The other micrograph shows the microstructure at only 200 Å thickness. The light circles in the 500 Å micrograph are spots where the film is thinner than the surrounding area; the same spots appear as white "bubbles" in the 200 Å film, which suggests that the surface coverage is incomplete. Typically, thin film growth achieves full surface coverage at lower thickness. However, with reference to Chiang's kinetic mechanism for H-atom assisted II-CVD, the carbon removal occurs on the surface. With this mechanism in mind, the H-atom removal effectively etches carbon from the surface as the copper film grows.

The plan view micrographs do not offer the same contrast as the standard II-CVD films because of the cessation of columnar growth, so there is no carbon rich area to produce Z contrast with copper. The dark crystallites are due to diffraction contrast. Figure 3.24 (bottom) shows that triple points are starting to form between some of the discernible crystallites – a trend toward conventional equiaxed microstructure. Note that some of the crystallites are not discernible because of the diffraction conditions. The microstructure evolves independently of growth rate (0.1 to 1.0 Å/s) and temperature (25°C to 71°C) for the indicated ranges. The electrical resistivities of the H-atom films are also independent of temperature. Clearly, the carbon removal mechanism dominates the microstructure evolution. As carbon forms on the surface – in an instant prior to

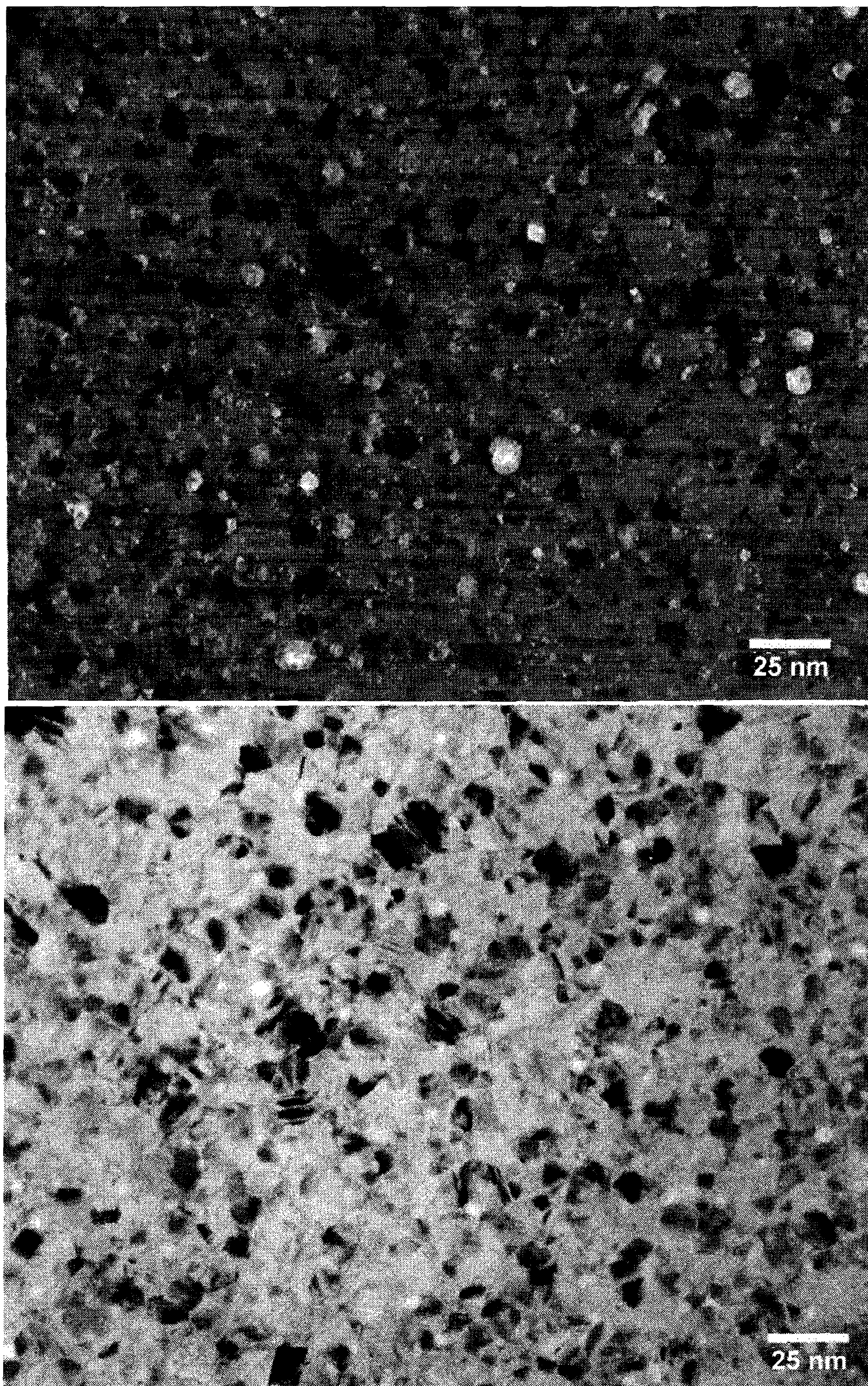

Figure 3.24: H-atom assisted II-CVD at 25°C, 500V and 0.7 Å/s from two different runs. Hydrogen flow set at 0.36 sccm. Top: 500 Å thick. Bottom: 200 Å thick. Notice that the magnification is twice that of the columnar micrographs,

being etched by the H-atom beam – it may interrupt growth and induce nucleation events.

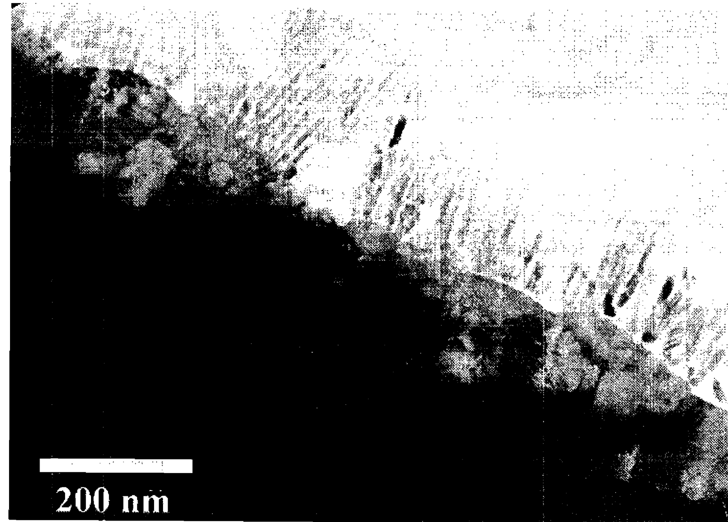

Figure 3.25: XTEM sample with two layers. Bottom layer: H atom assisted with 0.36 sccm H_2, 25°C, 500V and 0.75 Å/s. Top layer shows remnants (due to ion milling) of columnar II-CVD film shown in Figure 3.22.

XTEM (Figure 3.25) illustrates the distinct difference between normal and H-atom assisted II-CVD. It is difficult to discern the interface between an H-atom copper film and the copper substrate. However, the diffraction pattern produces a distinct demarcation due to the micron scale microstructure of the annealed OFHC copper substrate and the nanoscale microstructure of the II-CVD film. Figure 3.26 shows a transition where the H-atom source accidentally extinguished. Note that the microstructure appears columnar, albeit dense, when the H-atom assisted growth resumes. The H-atom beam source had to be retuned; the micrograph illustrates that the source did not provide sufficient hydrogen dissociation to completely etch the carbon. The cessation of columnar growth requires complete removal of carbon. Another interesting phenomenon is the preservation of crystal orientation across the different layers in the XTEM sandwich. (Figure 3.26.)

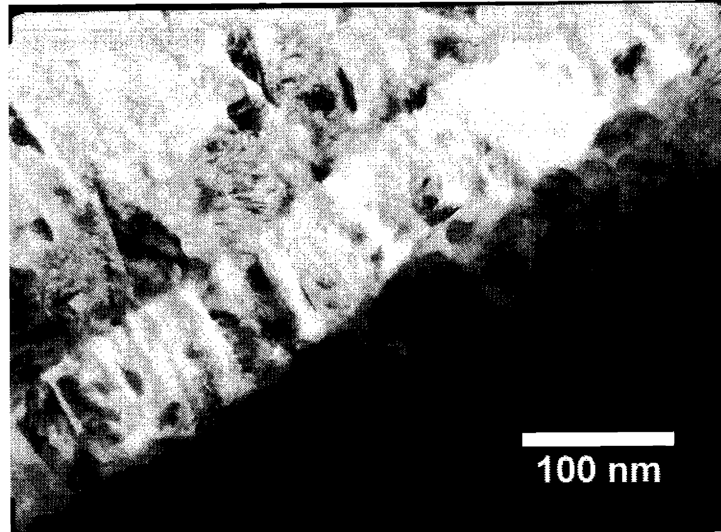

Figure 3.26: Sandwich of four XTEM II-CVD films. Bottom layer: 71°C, 0.15 Å/s and 500V H-atom assisted deposition. Second layer: H-atom beam accidentally extinguished. Third layer: H-atom source re-started, but hydrogen dissociation is insufficient to remove all of the carbon. Top layer: 79°C, 0.2 Å/s and 500V.

3.8 XPS Quantitative Analysis.

XPS determined the composition of the II-CVD films using the ion beam profiling technique described in Chapter 2. Figure 3.27 shows an XPS spectrum after ion beam profiling, which removes organic contamination. Figure 3.28 zooms in on the Cu and C peaks. The binding energy of the carbon corresponds to graphitic C-C bonding. The shape of the left hand side of the curve indicates that there are also some higher energy bonds, which is consistent with amorphous carbon.

Figure 3.29 plots the XPS quantitative analysis as a function of temperature at 1 Å/s and minimum ion flux rate (~1 $\mu A/cm^2$), which corresponds to 0.1 Å/s at low temperatures. This data confirms that higher growth rates lead to greater carbon fractions. Figure 3.30 compares the XPS data to volume fraction of columns (converted to equivalent atomic fraction) in the microstructure. Both plots indicate that the columns do not account for the XPS copper fraction, but notice that the difference between column fraction and atomic fraction is considerably larger at

low growth rate. This leads to either of two conclusions: the area surrounding the matrix does in fact contain copper, or there is a systematic error in the XPS quantitative analysis. However, the discrepancy is much greater at 0.1 Å/s than 1 Å/s, which suggests that the latter case is improbable. STEM analysis resolved this issue by probing the regions in between the columns, which is the topic of the next sub-chapter.

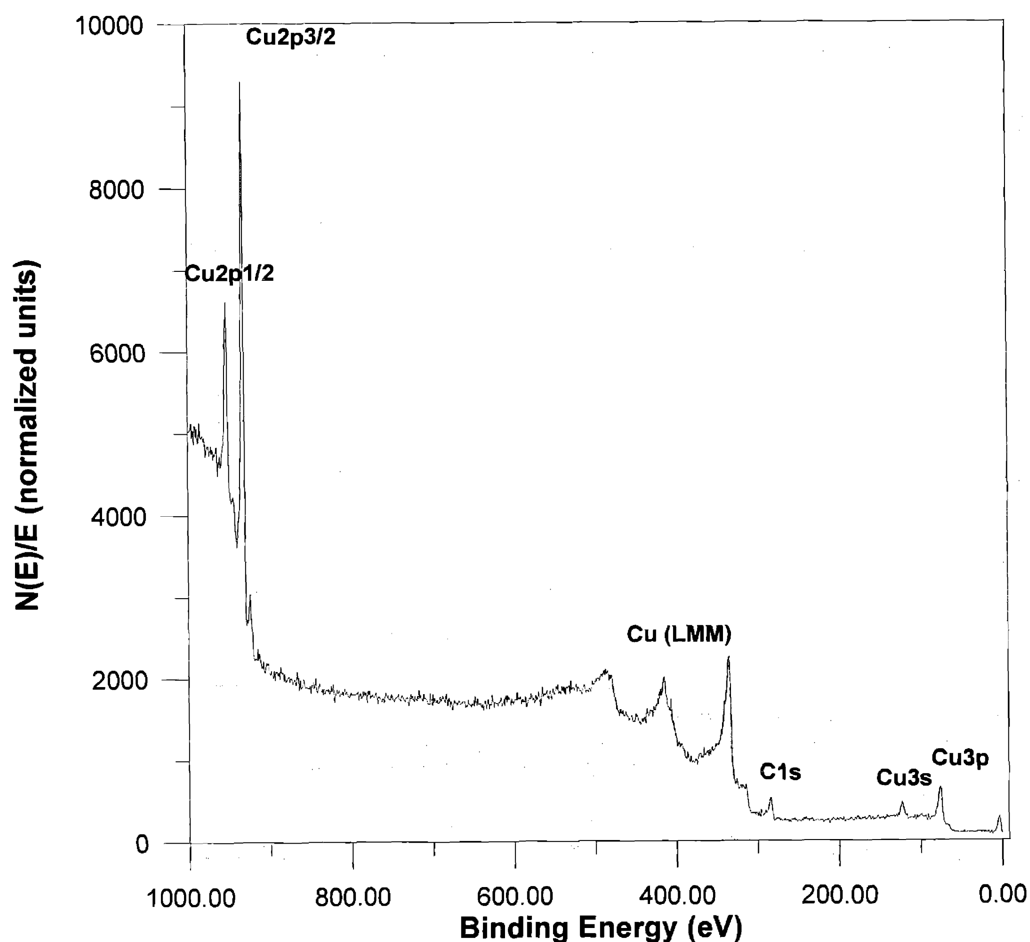

Figure 3.27: XPS spectrum after ion sputter profiling for sample at 79°C and 1 Å/s.

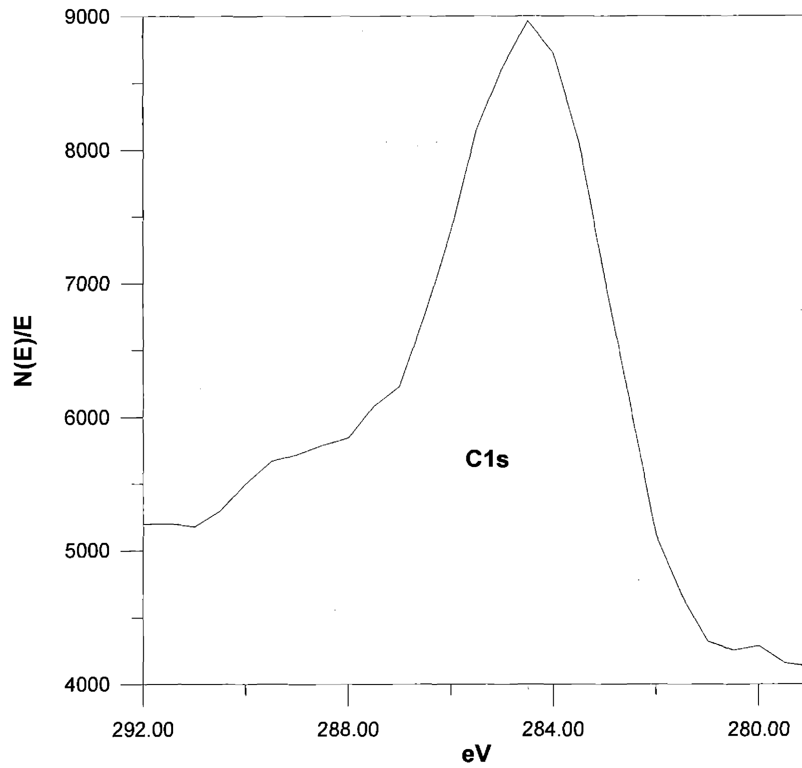

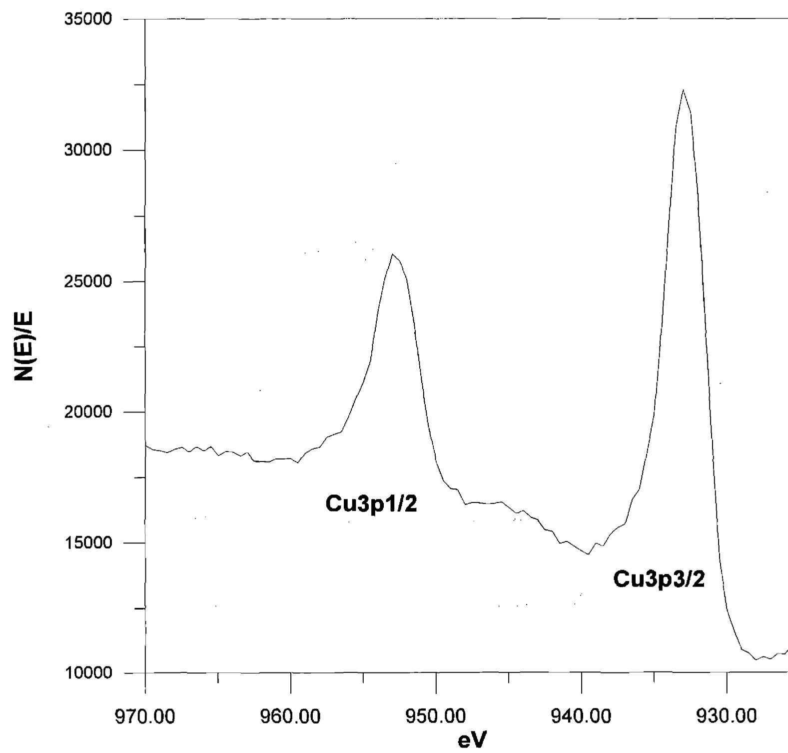

Figure 3.28: C1s and Cu3p spectra, which are used for quantitative analysis. From a sample deposited at 25°C and 1 Å/s.

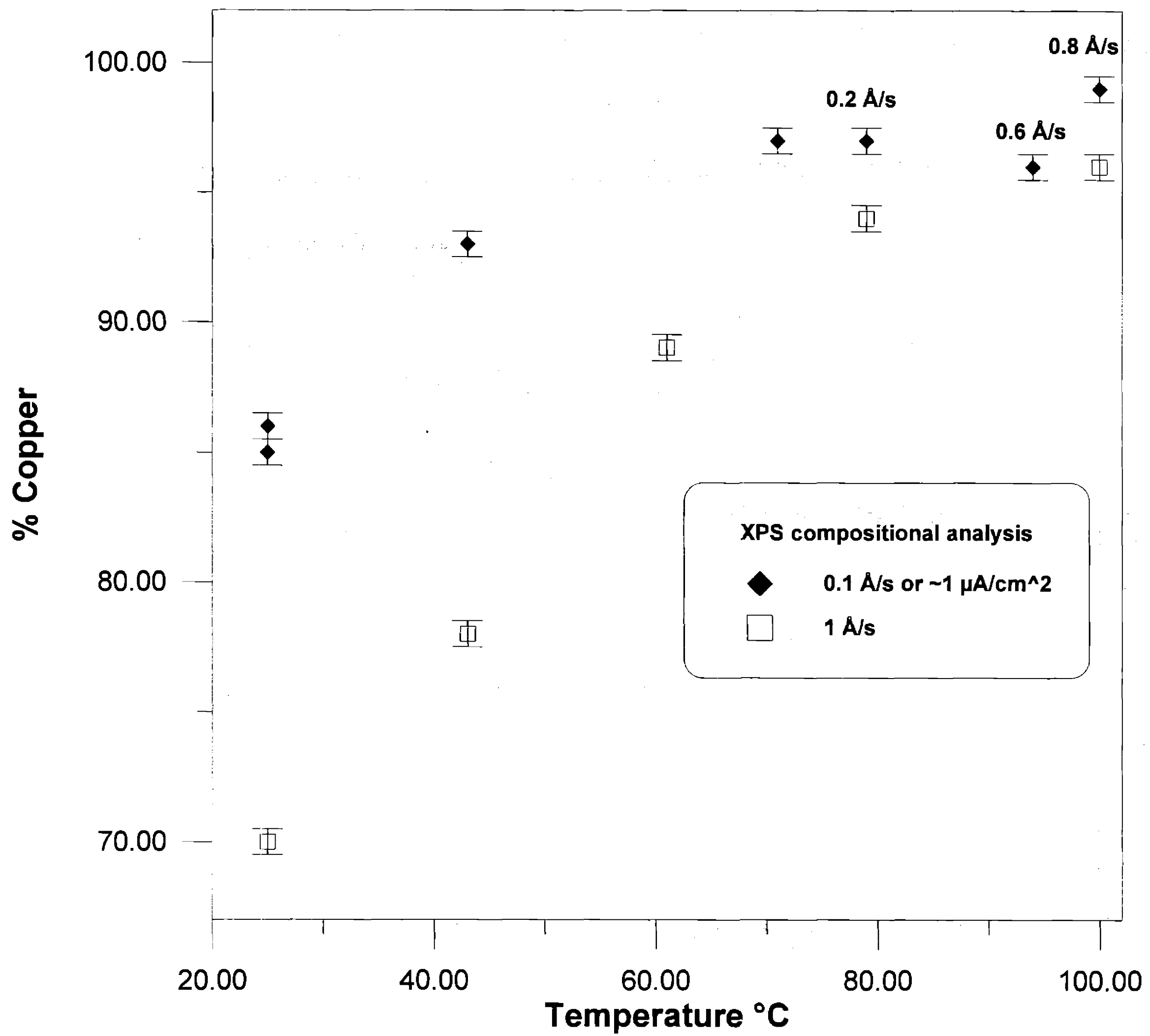

Figure 3.29: % Cu versus temperature at 1 Å/s and "low ion flux". (The latter equals 0.1 Å/s at low temperatures.) The points are labeled when the growth rate is greater than 0.1 Å/s.

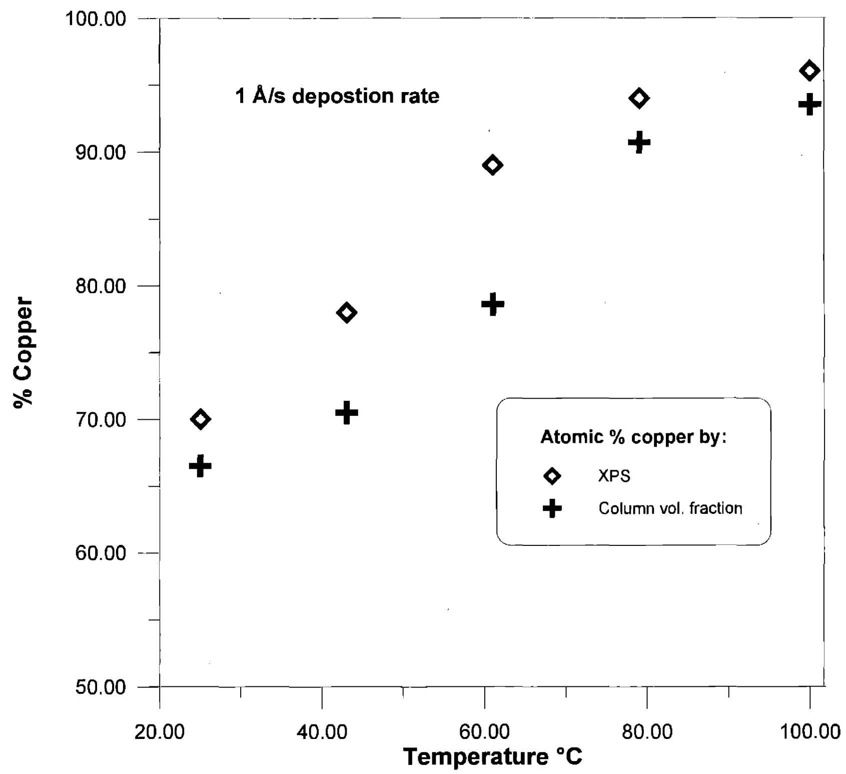

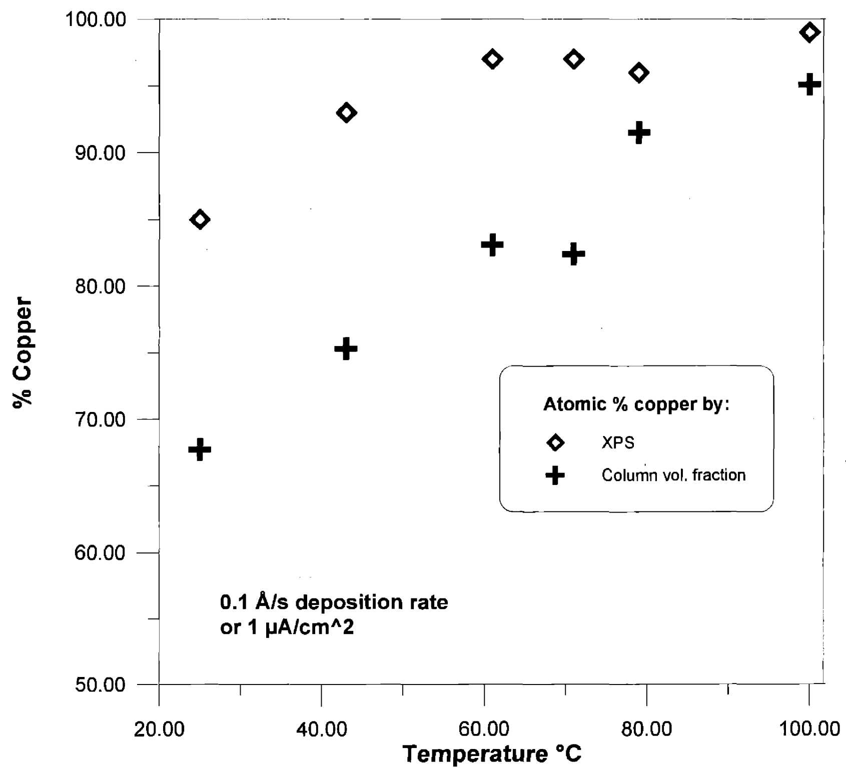

Figure 3.30: Comparison of XPS data with volume fraction of copper columns (converted to atomic fraction) at 1 Å/s and 0.1 Å/s (or 1 µA/cm^2 equivalent ion flux.)

3.9 STEM-EDS Analysis

STEM-EDS analysis produced EDS maps of the microstructure that compared directly to a STEM image of the same region. In this case, a Cu K-α map of the surface should produce a digitized image that resembles the columnar microstructure. (Figure 3.31.) However, it was not possible to do the same mapping for carbon because of ubiquitous contamination with organic matter of any surface that had been exposed to the environment. Figure 3.31 verifies that the columns are in fact copper but the analysis is somewhat inconclusive concerning the inter-columnar regions. The Cu K-α peaks translate to a digitized image with eight levels of gray; the image suggests that there is copper outside the columns.

EDS spectra from single points provide better data and the 1 nm resolution of the VG-H603 STEM permitted probing in between the copper columns. Comparing Figure 3.32 and Figure 3.33 show spectra on and off columns for 0.1 Å/s and 1.0 Å/s deposition, respectively. Extraneous carbon contamination precludes quantitative analysis but the spectra do verify the presence of copper outside the columns. Furthermore, the peak ratio at 1 Å/s is approximately 4.5:1 while it is only 2.75:1 at 0.1 Å/s. This agrees with the XPS data inasmuch as it indicates that the lower growth rate incorporates a higher inter-columnar copper fraction. It is important to maintain the same electron beam current for these comparative experiments. The spectra are taken in quick succession and the bremstrahlung intensity at 0 eV serves as a yardstick for the electron beam current.

Figure 3.34 shows the spectra for 0.3 Å/s deposition at 43°C and 200 eV. These conditions produce a microstructure that exhibits incomplete coverage of copper columns. It appears that the columnar growth mechanism shuts off locally. The EDS spectra indicate that the intensity ratio is only 2:1. XPS analysis measured

that the film contains 80 atomic % copper while the converted volume fraction is only ~55 atomic % copper. Furthermore, the microstructure is metastable as illustrated by Figure 3.35. The high intensity field emission electron beam of the VG-H603 supplied sufficient energy to regrow the microstructure.

Thus, the EDS analysis verifies that the microstructure matrix incorporates excess copper and the characteristic microstructure in the ion-flux-limited regime appears to evolve independently of the carbon impurity level. This runs contrary to intuition but proves to be invaluable information prior to developing a model for II-CVD microstructure evolution. It must account for constant column diameter even though the carbon content increases with the growth rate.

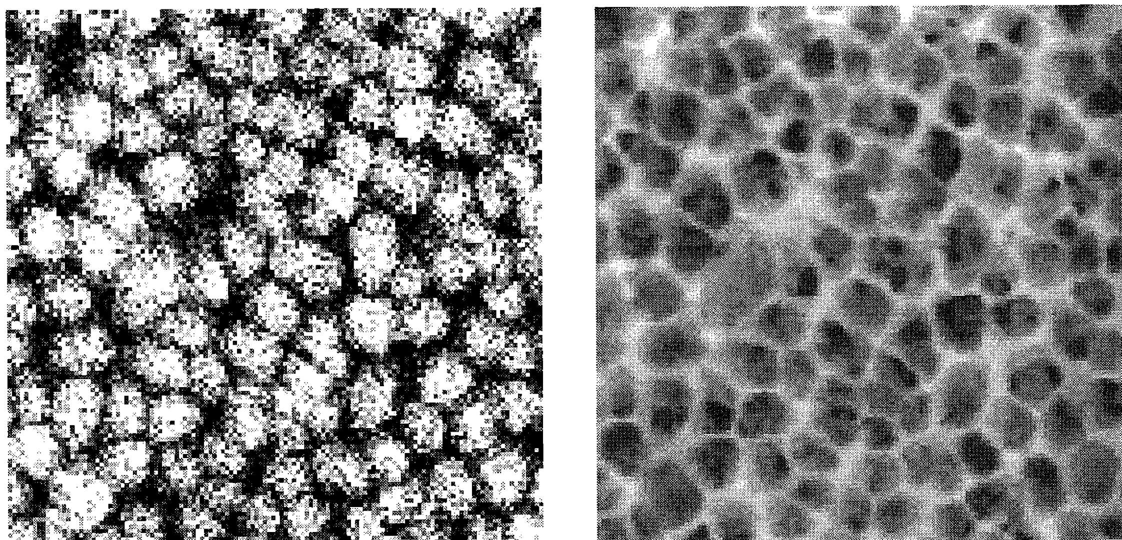

Figure 3.31: STEM-EDS Cu K-α map (left) and bright field STEM image (right) of the same region. 0.1 Å/s deposition at 500 eV and 25°C.

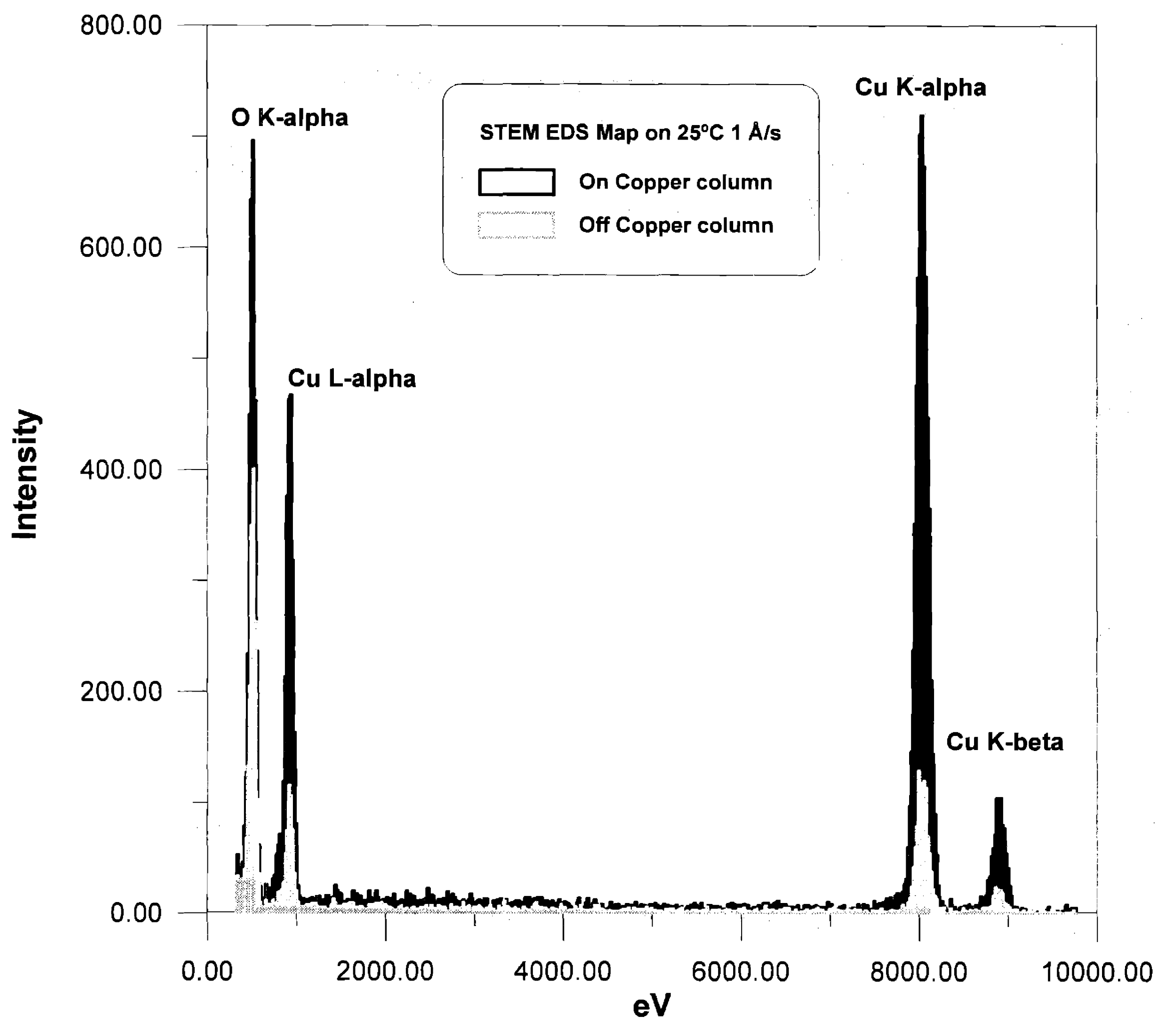

Figure 3.32: STEM-EDS spectra on/off column. 0.1 Å/s deposition at 25°C with 500 eV ion beam.

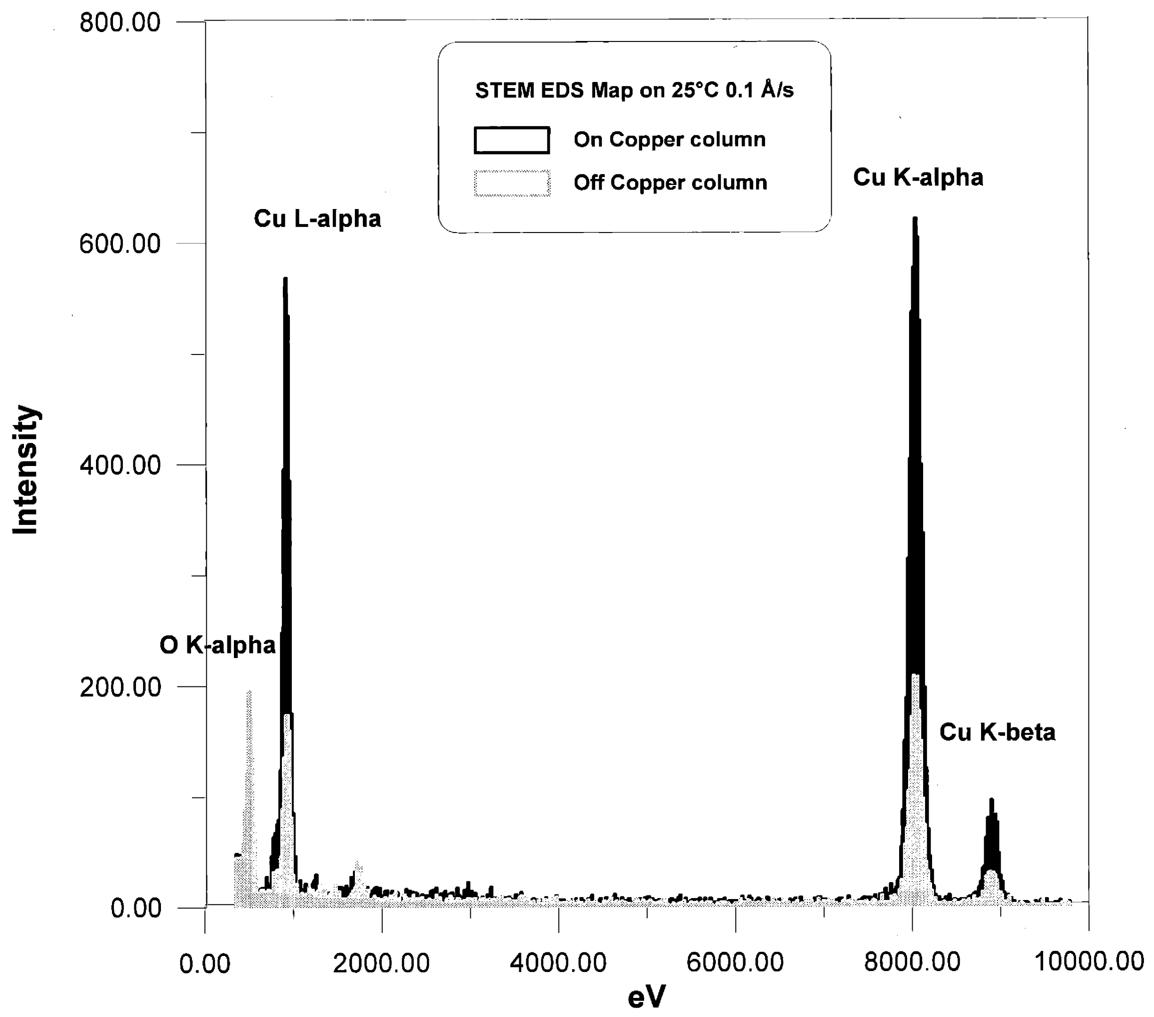

Figure 3.33: STEM-EDS spectra on/off column. 0.1 Å/s deposition at 25°C with 500 eV ion beam.

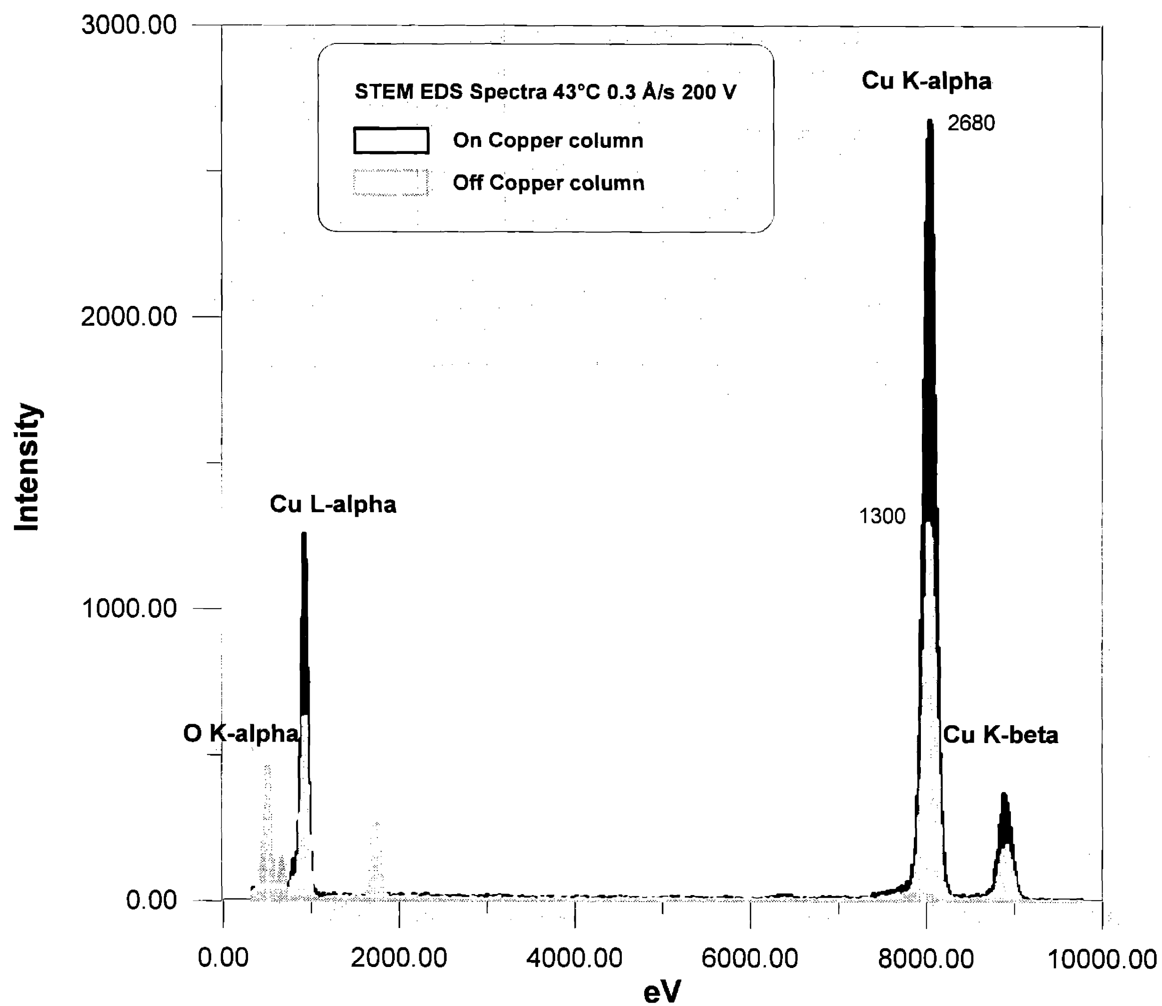

Figure 3.34: STEM-EDS spectra on/off column. 0.3 Å/s deposition at 43°C with 200 eV ion beam.

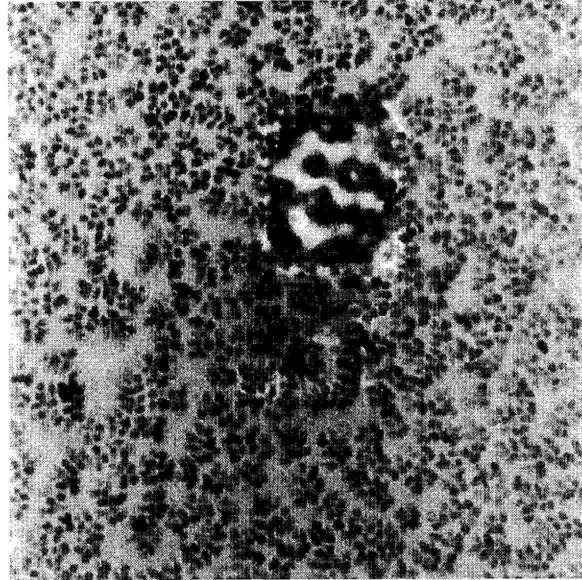

Figure 3.35: STEM image of 0.3 Å/s film at 43°C and 200 eV ion beam energy. Note the sparse surface coverage and the effect of the field electron beam as it rastered the central rectangle. (Viewed at higher magnification.)

3.10 Microstructure Evolution: Ion Beam Voltage

The previous section illustrated the effect of low ion beam voltage on the microstructure: irregular coverage and low density of columns at 200V and 43°C. It is important to understand the effect of beam voltage on II-CVD because a practical application of this research concerns FIB deposition at 25 keV. The Kaufman ion gun limits the range of voltages to 200V-1000V. The variable voltage experiments were conducted in the ion-flux-limited regime and use a fixed growth rate of 0.3 Å/s. The choice of 0.3 Å/s relates to a number of factors: the ion gun operation is stable without prolonged deposition time; the same ion flux yields this growth rate across the range of voltages; and it should not produce any "channeling" in the microstructure, which occurs at higher growth rates. Figure 3.36 illustrates the effect of an increasing beam voltage with respect to the number of atoms sputtered by each ion. Notice that the carbon does not sputter at 200V. This will produce higher carbon fraction but the effect

also depends on the overall sputtering probability. Chiang's surface kinetic model predicted relatively high precursor surface coverage at 0.3 Å/s in the ion-flux-limited regime – an average of approximately 2% empty surface sites – so the sputtering contribution is not significant.[12] Thus, zero carbon sputtering cannot explain the microstructure of Figure 3.37. The STEM-EDS analysis showed that the intercolumnar regions contain high fractions of copper.

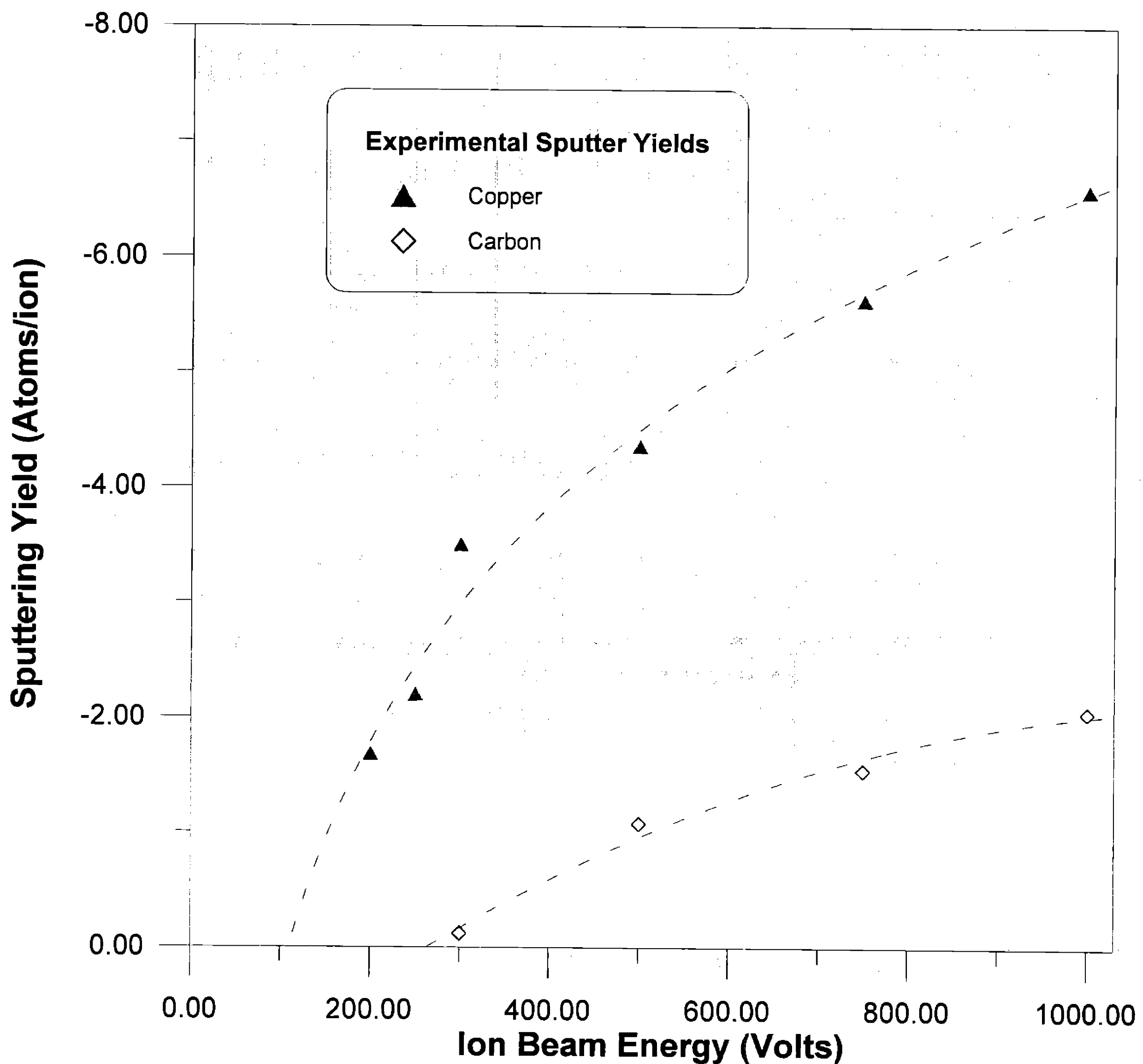

Figure 3.36: Experimentally measured (QCM) sputter yield for pure carbon and copper versus beam voltage.

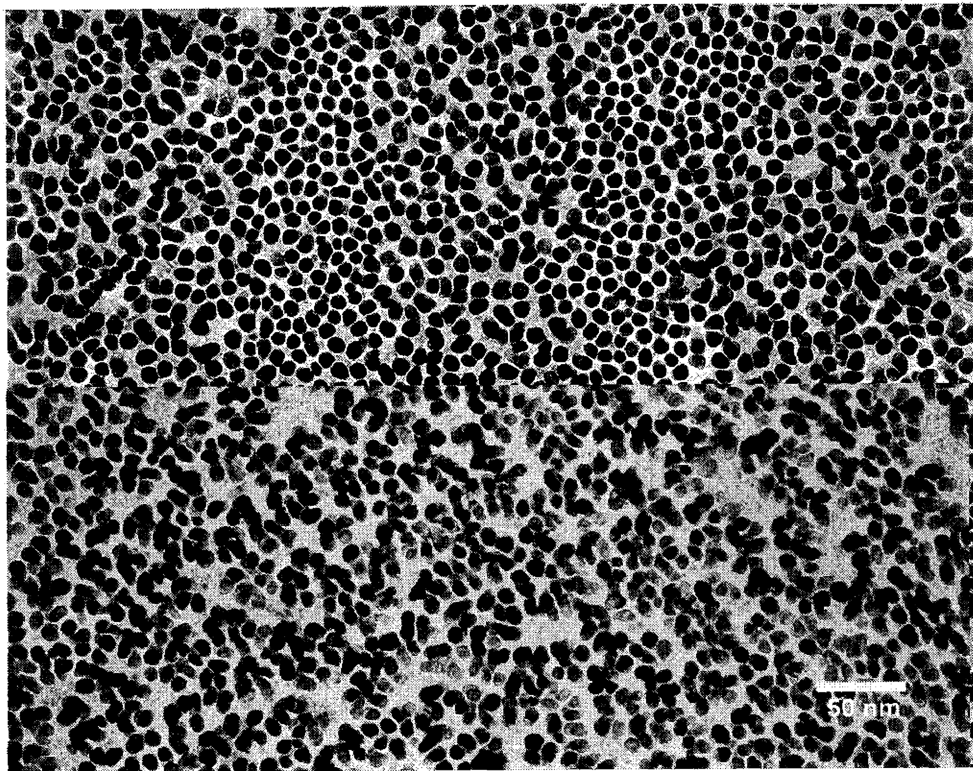

Figure 3.37: Split screen image of two regions at 200V and 43°C. 5.5 μA/cm^2 ion flux.

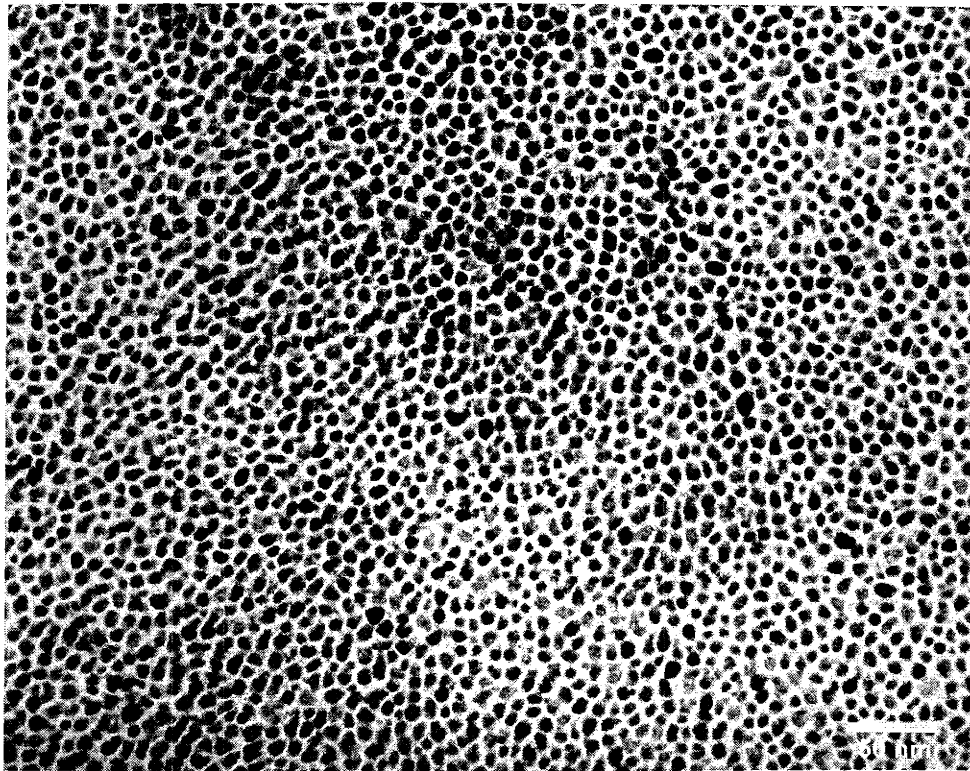

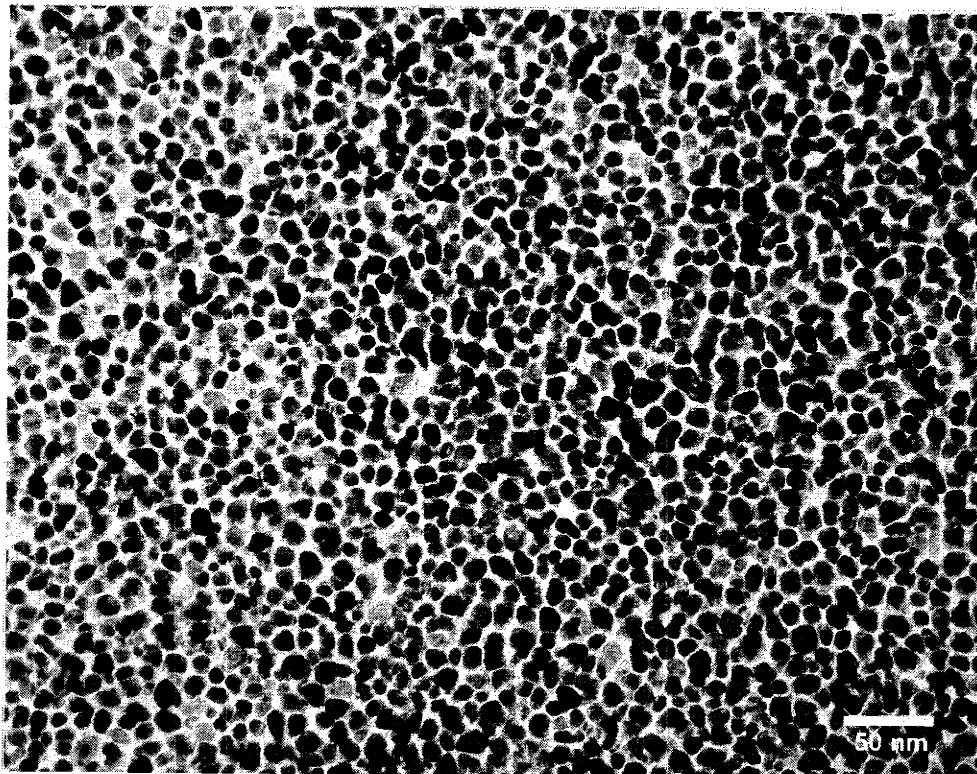

Figure 3.38: Microstructures at low ion beam voltage. Top: 300V, 25°C and 0.3 Å/s. Bottom: 200V, 71°C and 0.3 Å/s.

The beam voltage has a significant impact on the column diameter. Figure 3.39 illustrates the increase in average column diameter with beam voltage. Notice the drop in columnar diameter from the higher voltage range (500 to 1000V) to the lower voltage deposition range (200V to 300V). Furthermore, II-CVD at 200V and 25°C does not produce a columnar structure; however, the observed diffraction pattern verified that this film contains copper. Similarly, Figure 3.37 shows that the column density is not constant across the film at 43°C and 200V. The STEM-EDS verifies that the higher grayscale level in the background is in fact due to a high fraction of copper outside the columns. The upper half of Figure 3.37 indicates that the background is lighter around high-density clusters of columns due to a lower copper fraction outside the columns in this region. At 71°C and 200V (Figure 3.38; bottom), coverage is continuous but the column diameter (14.6 nm) is only equivalent to deposition at 25°C and 500V. Figure 3.38 also shows that there is a greater distribution of column diameters with many sub-10 nm columns interspersed in the microstructure. The microstructure at 300V has continuous columnar coverage at all three temperatures. Deposition at 25°C and 300V exhibits the smallest measured average column diameter (10.7 nm) of any II-CVD film analyzed in course of these experiments. (Figure 3.38; top.)

The STEM-EDS analysis at 43°C and 200V indicates that the beam voltage affects the microstructure evolution mechanism rather than simply increasing carbon incorporation. The XPS quantitative analysis (Figure 3.40) verifies that the carbon fractions in the 200V to 300V range do not account for the smaller column diameters. For example, compare the column diameter at 25°C and 300V (10.7 nm) to that at 25°C, 500V and 1 Å/s (14.5 nm) where the copper fractions are similar: 68% and 70%, respectively. Similarly, the average column diameter at 200V and 43°C is only 11.8 nm, but the copper fraction (80%) is greater than that for 43°C, 500V and 1 Å/s (77%) where the average column diameter is 16.5 nm. At 71°C, where the mixed II-CVD and thermal CVD mechanism prevails, there is little difference in copper fractions but a marked

difference in column diameter (Figure 3.39) between 200 to 300V and the higher ion beam voltages.

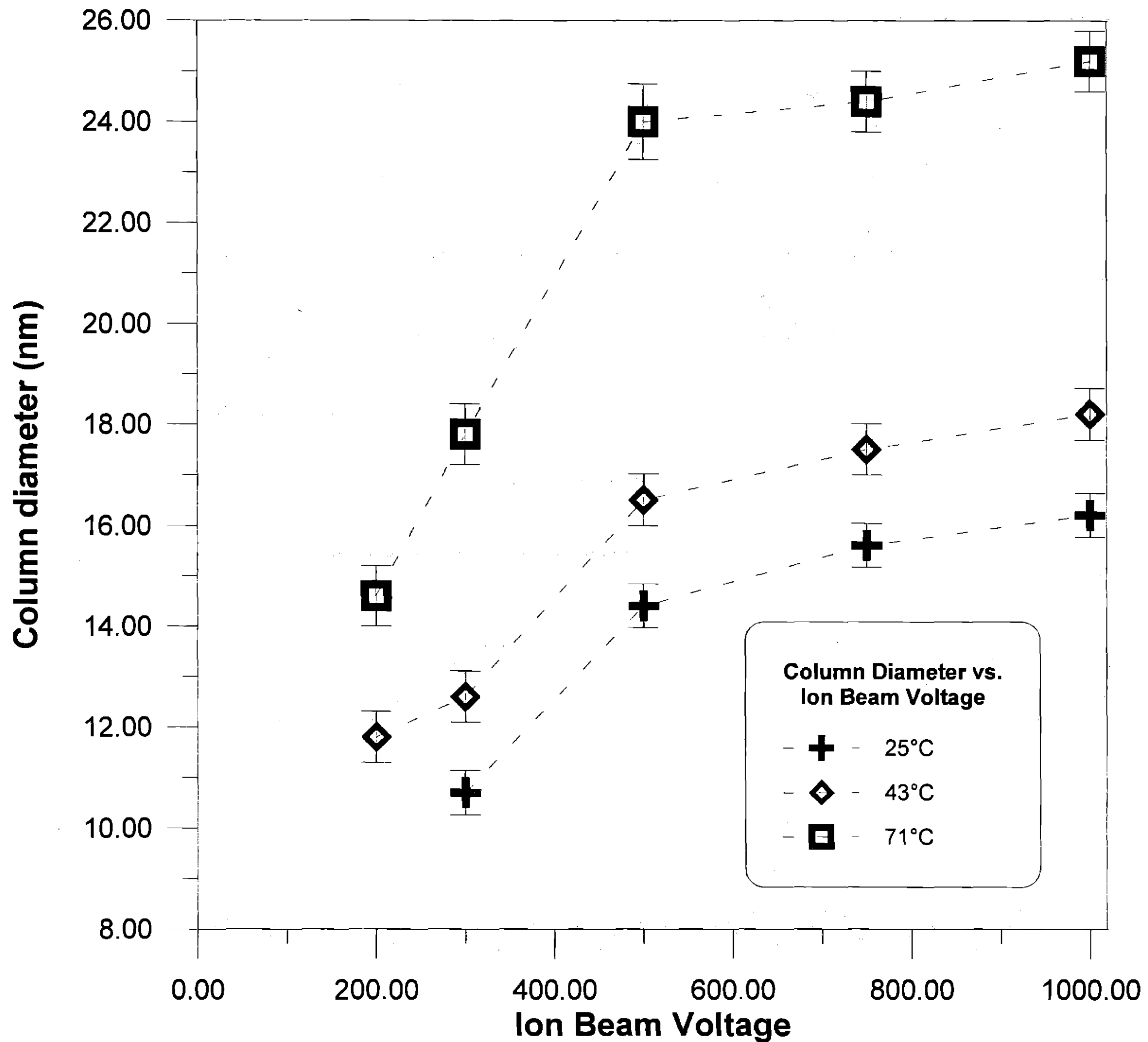

Figure 3.39: Column diameter versus ion beam voltage at three different process temperatures. Growth rate is constant at 0.3 Å/s. II-CVD at 25°C and 200V does not produce the characteristic columnar structure.

Clearly, the ion beam voltage has an effect on the microstructure evolution. Deposition at 200V and 300V leads to smaller column diameters. The data is not conclusive about the effect between 500V and 1000V; here, the gradual increase in column diameter could still be due to an increase in copper fraction. The microstructure model in Chapter 4 will address this issue. Keep in mind that FIB

deposition at 25 kV produces a similar microstructure, so the increase in column diameter must reach a limit at some voltage that is not too much greater than 1000V. Della Ratta found that the average column diameter at 25°C with a 25 kV focused ion beam is approximately 20 μm.[33] Although this number represents an estimate by Della Ratta rather than a result from quantitative microanalysis, it is consistent with the trend exhibited by Figure 3.39 assuming that the curves for 25°C and 43°C approach asymptotes.

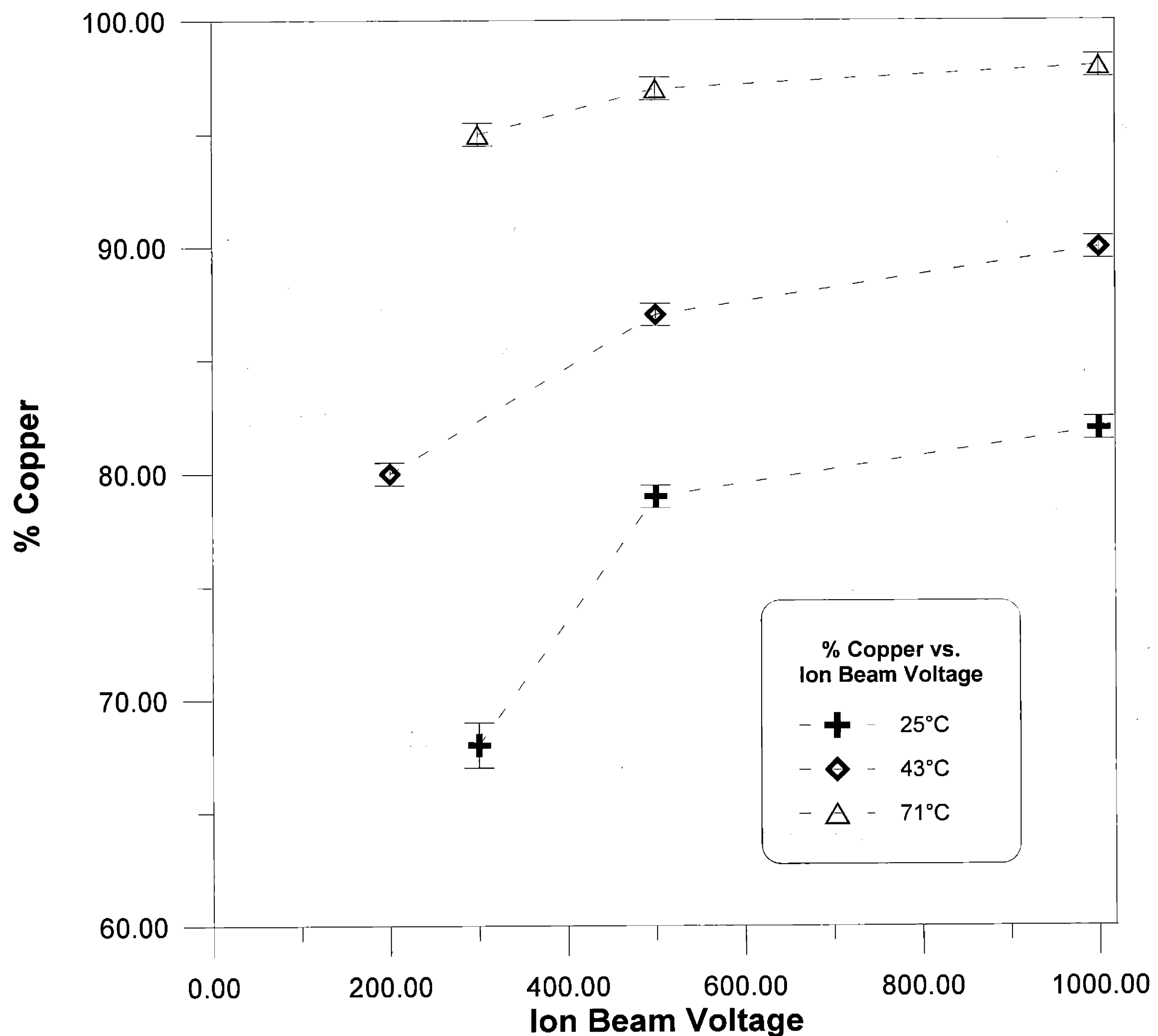

Figure 3.40: Ion beam voltage versus % copper at 0.3 Å/s for three different temperatures.

3.11 Topography: AFM and SEM

AFM determined if there is any macroscopic roughening of films deposited by II-CVD. Comparing figures Figure 3.41 and Figure 3.42 indicates that the surface roughens at higher temperature: 0.5 nm RMS roughness at 25°C, and 2.0 nm RMS roughness at 100°C. The 0.5 nm RMS roughness is equivalent to the value for the underlying uncoated Si_3N_4 substrate. Clearly, the increased roughness at 100°C is due to the onset of mixed regime thermal II-CVD.

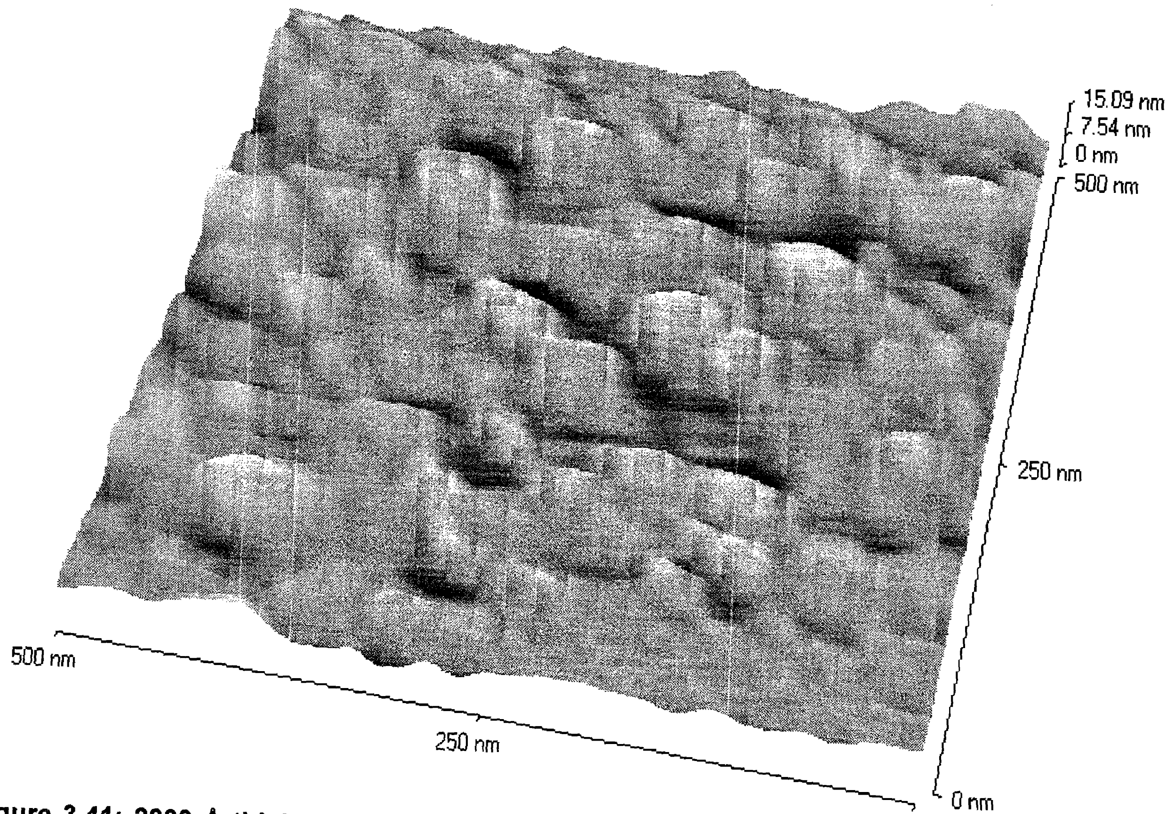

Figure 3.41: 2000 Å thick film deposited on Si3N4 at 100°C and 1.1 Å/s with 500 eV ions. The RMS roughness is 2.0 nm.

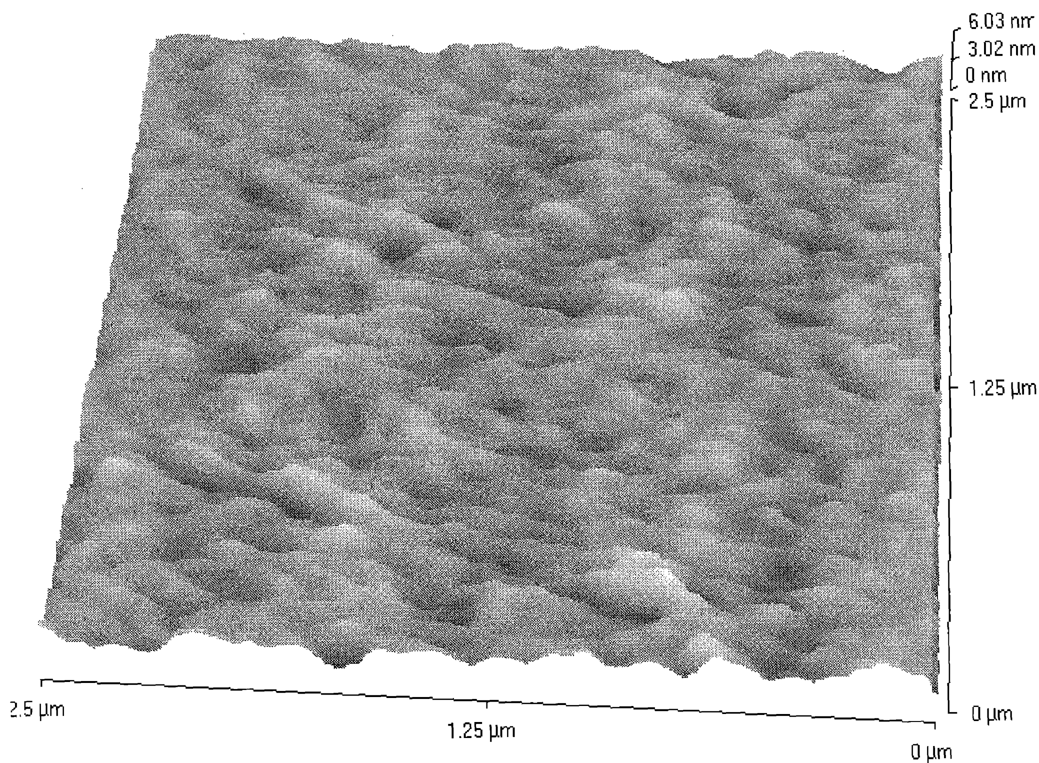

Figure 3.42: 2000 Å thick film deposited on Si_3N_4 at 25°C and 1 Å/s with 500 eV ions. The RMS roughness is 0.5 nm.

Cross-sectional SEM investigated II-CVD films that were deposited conformally on plasma etched polysilicon substrates at 25°C. Again, the II-CVD replicates the underlying substrate roughness. Figure 3.43 (d) shows the roughness of the etched polysilicon prior to deposition. Thus, the topographies of the other SEMs replicate the substrate roughness. The conformal coverage in the deep trench (a) is remarkable. Most CVD process lead to conformal coverage because they are substrate mediated.

(a)

(b)

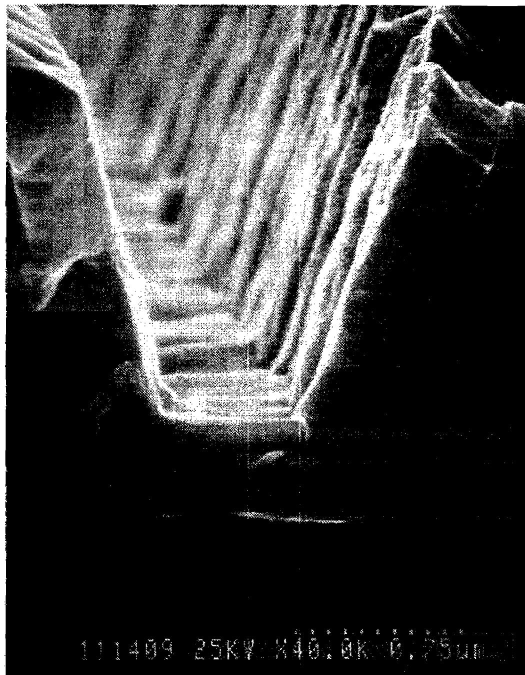

(c)

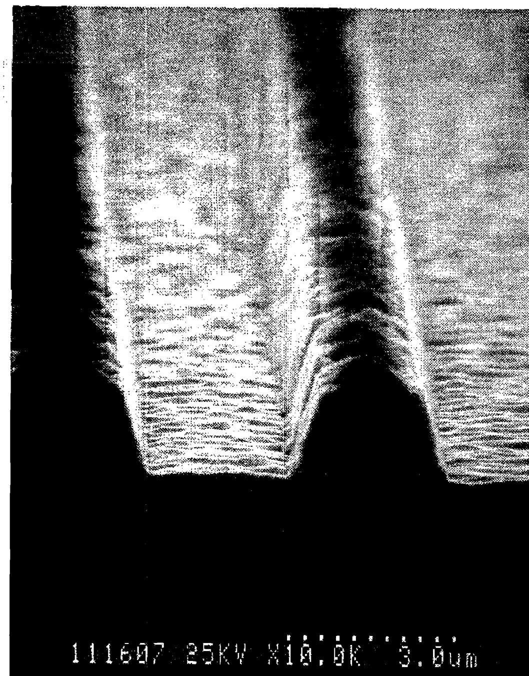

(d)

Figure 3.43: SEM cross-sections of II-CVD film on etched polysilicon. Notice the conformal coverage. (d) shows the polysilicon before it was coated.

However, the deposition rate in II-CVD scales with the ion flux, which decreases as the cosine of an angle deviating from perpendicular ion bombardment. On the

other hand, the sputtering yield of ion bombardment scales approximately as a reciprocal cosine function up to a limit in the range between 60° and 80°; the deposition yield in II-CVD may also scale in this way. Thus the two effects cancel each other. Figure 3.43 (a) has very steep sidewalls (approximately 77°) and the film appears to be thinner towards the bottom of the trench. On the left-hand sidewall there is a ledge that orients the surface toward the ion beam; consequently, the film is thicker above it. The slope below the ledge is thinner because of the steeper slope of the sidewall.

3.12 Summary

This section summarizes and recaps the experimental data and associated conclusions:

- The Cu(I)hfac(vtms) precursor chemisorbs as a monolayer at room temperature. At higher temperatures (above 60°C) the precursor molecule slowly decomposes and deposits copper, indicating the threshold for contribution from thermal CVD with this particular precursor.

- Two primary deposition regimes are identified: the *ion-flux-limited* regime and the *gas-flux-limited* regime. The latter regime has insufficient gas flux, which produces incomplete precursor surface coverage during deposition. This leads to increased simultaneous sputtering of the evolving film; sputtering favors copper over carbon, so the films in this regime tend to have lower purity. The former regime has sufficient gas coverage and the growth rate is a function of the ion flux, which is considered to be the desirable deposition condition for II-CVD.

- Expressions were developed in order to determine quantitative data from planar TEM micrographs. The primary metric, *average column diameter*, was found from an expression that relates average number of columns per unit area in cross-section with the number of intersections per unit length of a line that traverses the same cross-section. This system is an adaptation of a technique originally devised by Fullman. The volume fraction of copper columns is determined by conventional metallographic point counting.

- The average column diameter is independent of the growth rate for constant substrate temperatures below 60°C in the *ion-flux-limited regime*. The column diameter is a function of the temperature; *therefore, the temperature alone determines the column diameter in this regime below 60°C.*

- The column diameter increases with decreasing growth rate at temperatures above 60°C. Thermal CVD becomes a factor above this temperature.

- XTEM verifies that the microstructure is continuously columnar through the cross-section. The diffraction patterns show some degree of texture: the mechanism favors growth perpendicular to the {111} family of planes. Dark-field XTEM indicates that the columns' crystal structures are highly faulted, but it is possible that the columns are single crystal. II-CVD at 100°C still retains a columnar microstructure, even though it contains less than 1% carbon.

- H-atom-assisted CVD effectively removes the carbon impurity and produces a non-columnar, equiaxed microstructure.

- XPS quantitative analysis shows that the copper fraction in the films increases with temperature and decreases with growth rate. The copper atomic fraction is compared to the fraction of copper columns in the microstructure – units are adjusted to atomic % copper. The fraction of

copper columns is smaller, but the discrepancy is much larger at low growth rate conditions.

- STEM-EDS verifies that there is copper outside the columns in the "matrix" of the microstructure. Qualitatively, STEM-EDS also provides evidence that there is more copper outside the columns at low growth rate conditions. Furthermore, low voltage (200-300V) depositions yield large copper peaks outside the columns; here, the microstructure is irregular with varying densities of copper columns.

- Above 500V the column diameter is a weak function of ion beam voltage; the column diameter increases with the voltage. However, the column diameter shows a marked decrease when the ion beam voltage drops to 200V or 300V. The copper fraction decreases with lower ion beam voltage, but the data suggests that the marked reduction in column diameter also relates to a mechanistic effect in the microstructure evolution. The lower energy ions do not provide the same level of enhancement to the surface diffusion of carbon.

- AFM shows that the surface of the II-CVD thin films roughen at higher temperature. This is due to the onset of thermal CVD at these temperatures.

- SEM shows that the II-CVD produces conformal coverage over steep sidewalls. The projected surface area that sees the ion flux scales with the cosine of this angle, while the deposition yield of II-CVD shows reciprocal cosine dependence up to a certain limit – analogous to conventional sputtering yield. These effects balance each other, which leads to conformal coverage with uniform thickness.

Chapter 4: Microstructure Model

4.1 Revisiting The Kinetic Model

This section outlines Chiang's kinetic model and presents an extension that yields better fit to experimental data.[12] One goal of this thesis is to present a unified model where the deposition conditions – *ion flux, gas flux and temperature* – predict the film composition and microstructure. Applying Chiang's model to the experimental data shows that it falls short in predicting composition and growth rates at very low ion flux.

Chiang presented a phenomenological model based on a reaction pathway that agrees with Gross's findings[49] for UHV decomposition of the precursor molecule:[12]

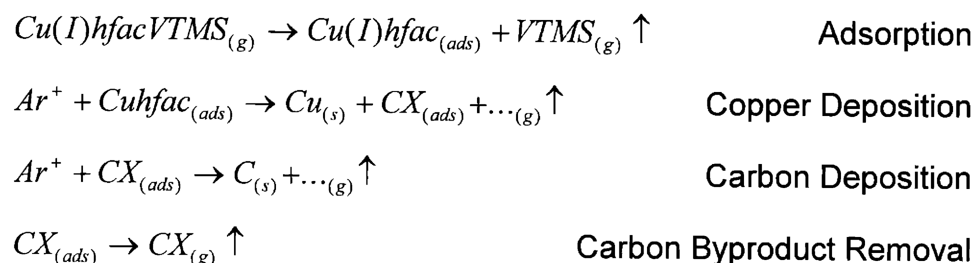

$$Cu(I)hfacVTMS_{(g)} \rightarrow Cu(I)hfac_{(ads)} + VTMS_{(g)} \uparrow \qquad \text{Adsorption}$$

$$Ar^{+} + Cuhfac_{(ads)} \rightarrow Cu_{(s)} + CX_{(ads)} + \ldots_{(g)} \uparrow \qquad \text{Copper Deposition}$$

$$Ar^{+} + CX_{(ads)} \rightarrow C_{(s)} + \ldots_{(g)} \uparrow \qquad \text{Carbon Deposition}$$

$$CX_{(ads)} \rightarrow CX_{(g)} \uparrow \qquad \text{Carbon Byproduct Removal}$$

Pyrolytic CVD produces lower carbon contamination than II-CVD because higher temperature increases the desorption rate of organic byproducts; also, II-CVD may produce more non-volatile products. Chiang's LITD (laser induced thermal decomposition) experiments identified CCO as the non-volatile CX byproduct. The equations represent a global simplification of the complex reactions, but they do capture the true functional dependencies. Chiang expressed the reaction as rate equations using Langmuir-Hinshelwood notation:

$$r_{ads} = K_{ads} f_g \theta \qquad \text{Adsorption Rate}$$

$$r_{dep}^{Cu} = K_{dep}^{Cu} f_i \theta_{Cuhfac} \qquad \text{Cu Deposition Rate}$$

$$r_{dep}^{C} = K_{dep}^{C} f_i \theta_{CX} \qquad \text{C Deposition Rate}$$

$$r_{des} = K_{des} \theta_{CX} \qquad \text{Organic Byproduct Removal Rate}$$

where f_g and f_i represent gas and ion flux, respectively, θ the fraction of empty sites, θ_{Cuhfac} the fraction of surface sites occupied by precursor molecules, and θ_{CX} the fraction of sites occupied by CX byproduct. The significance of surface sites in these equations agrees with the qualitative understanding of surface coverage, which in turn determines the ion-flux and gas-flux-limited regimes. The ratio of copper to carbon deposition rate (#/cm^{2}s) determines – after subtracting sputtering rates from the respective components – the composition of the II-CVD film. The net deposition rate is, of course, the sum of the two minus the effective sputtering rates.

Chiang determined the rate coefficients from experimental data. K_{des} is the most difficult rate coefficient to determine since it can only inferred from the rate of carbon deposition – quantitatively, the carbon fraction in the film. Chiang devised a clever method to determine the ratio using the following equation:

$$\frac{r_{dep}^{Cu}}{r_{dep}^{C}} = 1 + \frac{K_{des}}{K_{dep}^{C} f_i} \approx \frac{f_{Cu}}{1 - f_{Cu}}$$

where F_{Cu} is the atomic fraction of copper from XPS data. The approximate equality is due to the omission of sputtering. Therefore, this treatment is not valid at low surface coverage and high ion flux – i.e, the gas-flux-limited regime. Chiang rewrote the equation so that the slope of a plot of ion flux versus a function of the copper fraction is equal to $\frac{K_{des}}{K_{dep}^{C}}$:

$$f_i = \frac{K_{des}}{K_{dep}^C}(\frac{1-f_{Cu}}{2f_{Cu}-1}) \qquad [4.1]$$

Figure 4.1 shows the fit of f_i versus $(\frac{1-f_{Cu}}{2f_{Cu}-1})$. K_{dep}^C is the rate constant for the decomposition yield of carbon, which is measured as a yield of carbon atoms per Ar^+ ion. Therefore, K_{dep}^C is independent of ion flux and temperature; Chiang determined that it is approximately equal to 4.5 C atoms/ Ar^+ ion. So K_{des} equals 4.5 multiplied by the slope of the least squares fit in Figure 4.1.

Now, consider the trend that the data points in Figure 4.1 follow: they do not fall randomly on either side of the least-squares fit. Note that the fit is forced through the origin: as the ion flux rate goes to zero there is infinite time for CX byproduct to desorb and the film becomes pure copper. Chiang elected to use a least squares fit in order to make the analysis less sensitive to error introduced by the XPS data, but this assumes that K_{des} is independent of ion flux. He implicitly assumed that interaction of an ion with CX byproduct only leads to carbon incorporation. However, the reaction pathway is quite complex and CX really represents a number of different byproduct species. Therefore, it is possible that an increase in the ion flux also contributes to an increase in the byproduct desorption rate. Analysis of higher temperature II-CVD will shed more light on the issue later in this chapter. (Sub-chapter 4.5 "High" Temperature II-CVD.) Another explanation could be that K_{des} compensates for an over-simplification of the carbon sputtering mechanism in the surface kinetic model.

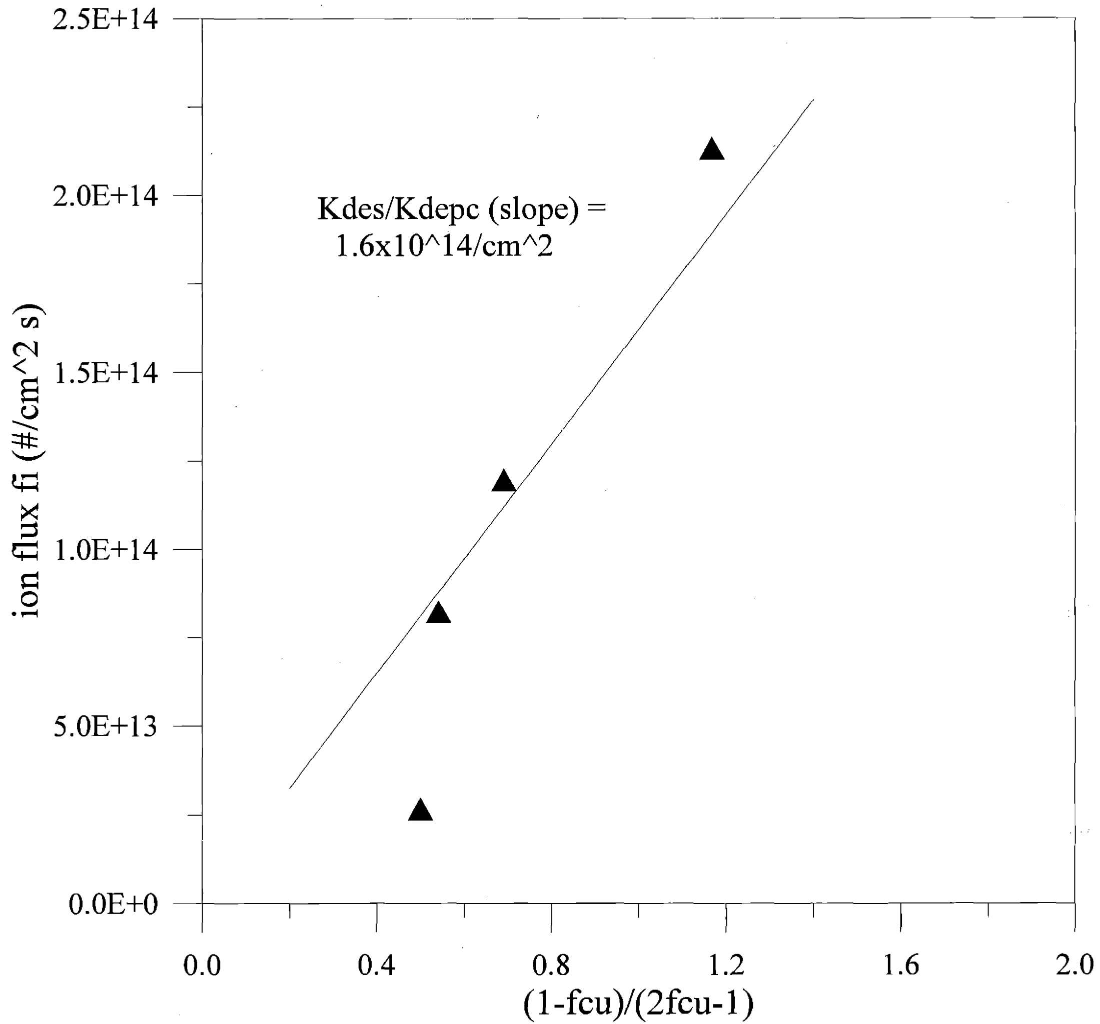

Figure 4.1: Ion flux vs.(1-F_{Cu})/(2F_{Cu}-1). F_{Cu} (atomic fraction of copper) is determined by XPS. Assuming that K_{des} is independent of ion flux, the slope equals $\frac{K_{des}}{K^{C}_{dep}}$. From [12].

Instead of fitting the data as in Figure 4.1, equation [4.1] should be applied directly. Graphically, this is equivalent to drawing lines from the origin to each data point in Figure 4.1 and determining the slopes. Chiang did not investigate the temperature dependence of K_{des}. Figure 4.2 illustrates the non-linearity of K_{des} versus ion beam flux. Figure 4.3 plots K_{des} values calculated from XPS data and equation [4.1] versus 1/T. The plot shows that there is an activation energy of 0.3 eV for byproduct desorption at all three growth rates. (Constant growth

rate is approximately equivalent to constant ion flux.) This is consistent with the expected physical adsorption of the organic byproduct.

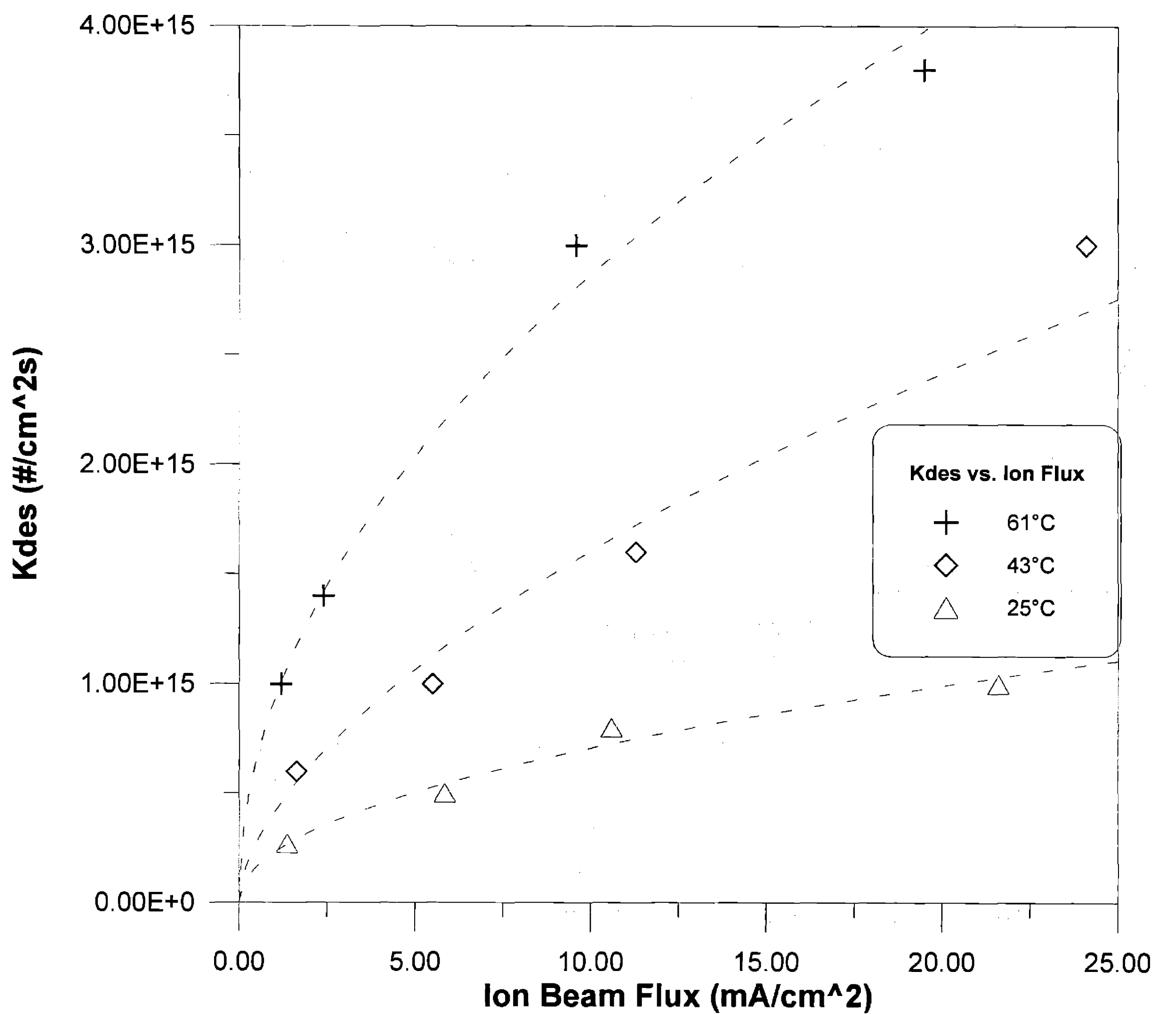

Figure 4.2: The non-linearity of K_{des} versus ion flux. The curves illustrate that the linear approximation breaks down at low ion flux.

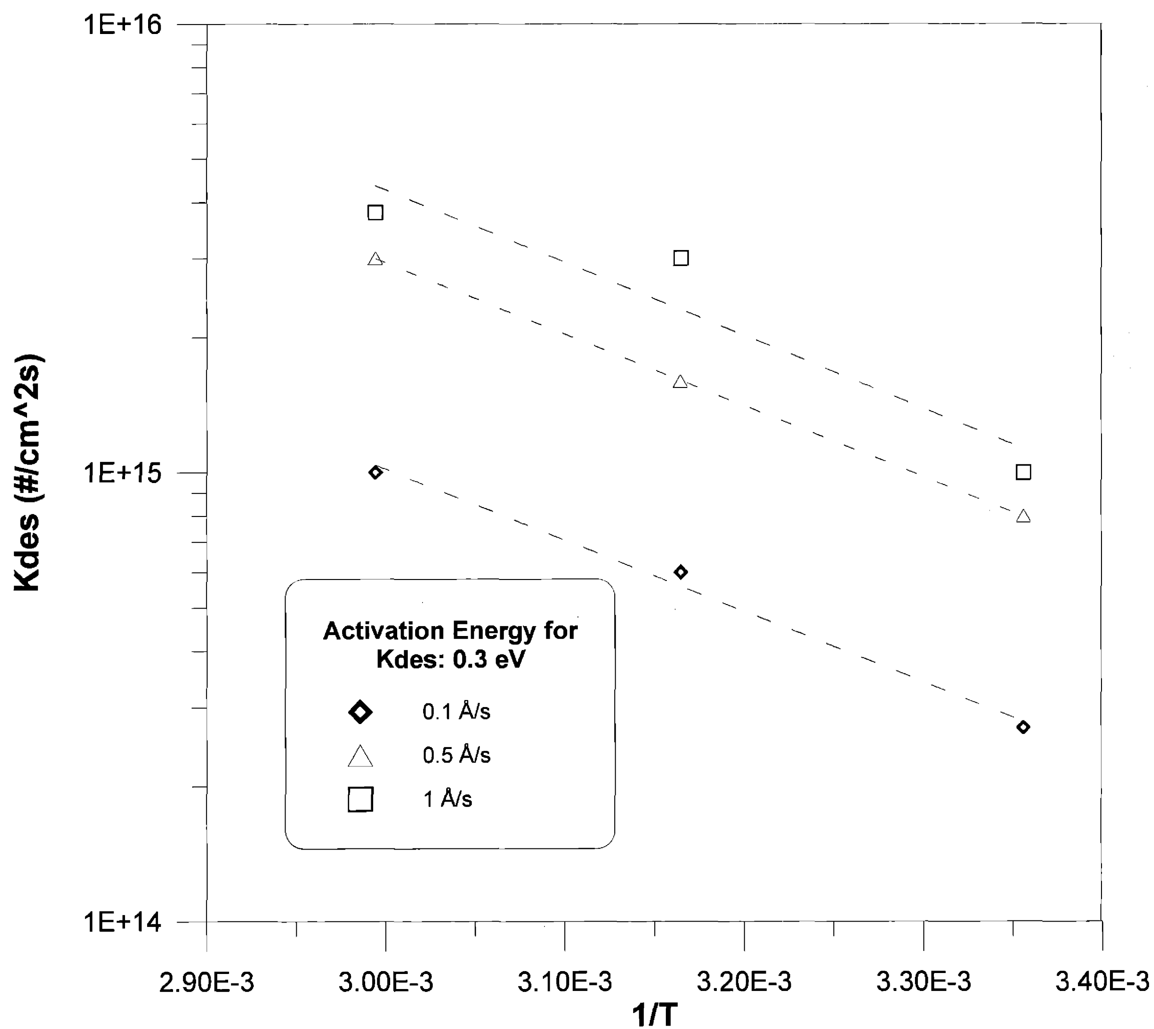

Figure 4.3: Arrhenius plot of K_{des} versus 1/T at constant growth rates. The plot shows that there is an apparent activation energy of 0.3 eV for byproduct desorption.

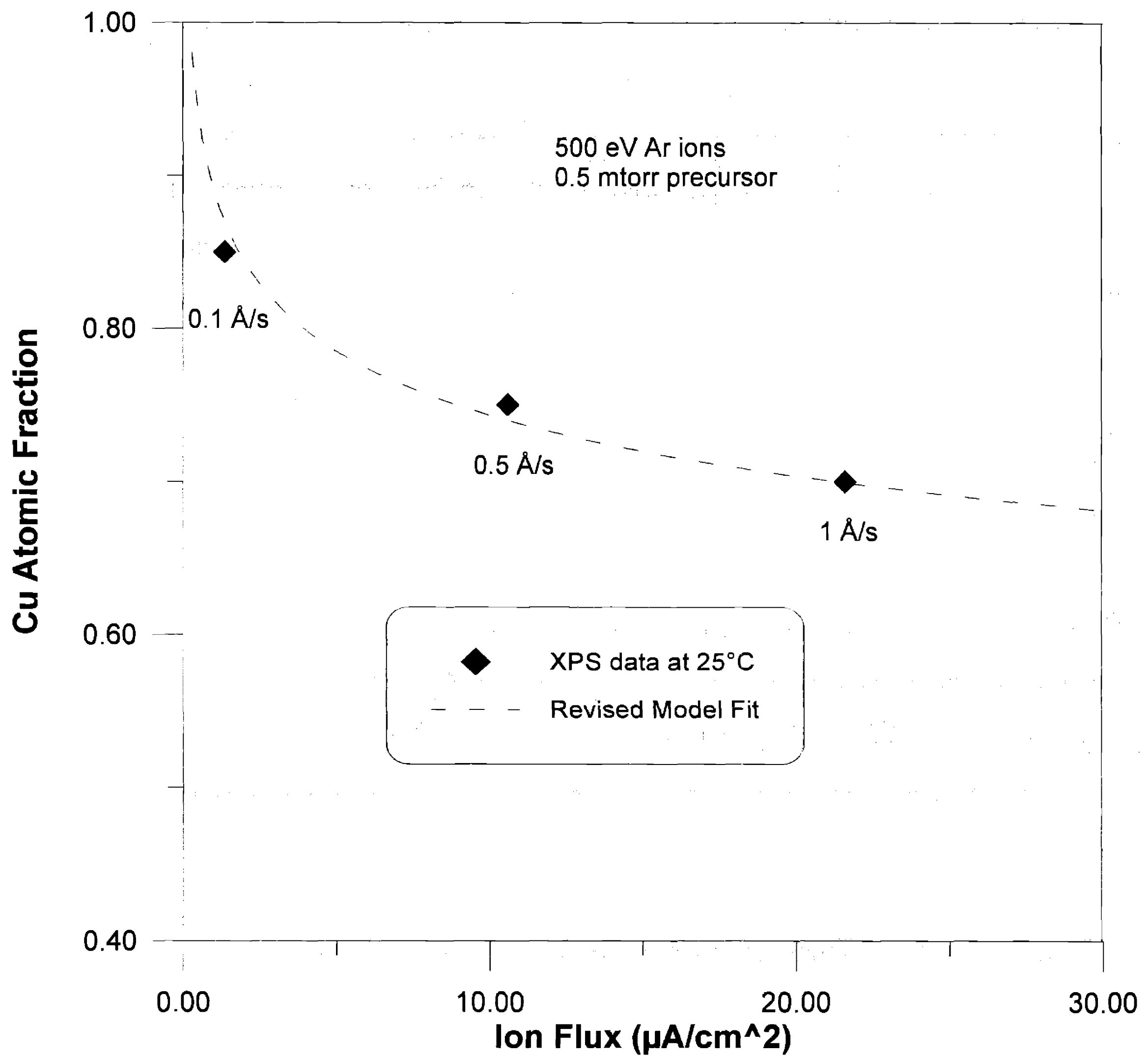

Figure 4.4: Comparison of extended surface kinetic model to XPS data.

Finally, Figure 4.4 illustrates the improved fit to XPS data with the extended surface kinetic model that permits K_{des} to vary with the ion flux. *This extended kinetic model can supply composition data to the microstructure model (sub-chapter 4.4) when experimental XPS data are not available.*

4.2 Cellular Growth

This section reviews cellular growth with a view to illustrate how II-CVD follows this mechanism. The discussion also contrasts the growth conditions of II-CVD with those of conventional CVD and PVD. Before addressing cellular growth, it is instructive to contrast the II-CVD process with classical mechanisms of nucleation and growth of thin films.

There are three classical modes of thin film growth. Two-dimensional layer-by-layer growth (Frank-van der Merwe growth) occurs when the binding between film atoms is less than or equal to that between the film atoms and the substrate. This mechanism is relatively rare; it occurs in homoepitaxy and special cases of semiconductor-on-semiconductor and metal-on-metal heteroepitaxial growth, such as Cd on W.[57] The second mechanism, Stranski-Krastanov, follows two-dimensional growth for a few monolayers and then switches to a three-dimensional growth mode. This three-dimensional mechanism is known as Volmer-Weber growth where islands nucleate on the substrate and coalesce into a continuous film. This requires stronger interatomic binding of the adsorbed atoms than that between the substrate and adsorbed atoms; therefore, this process depends on the wetting angle of the adsorbate. Metal film growth on an insulating substrate usually follows this mechanism.

Figure 4.5 illustrates Volmer-Weber growth. At the initial nucleation stage, an adatom on the substrate has a finite lifetime before it desorbs. It may combine with other adatoms to form a nucleus. A balance of volume and surface free energies determines a minimum critical size for a nucleus. A stable nucleus develops into an "island" via direct incorporation from the vapor phase, and coalescence with adatoms and subcritical nuclei. Eventually, the inter-island spacing reaches a critical limit where the islands begin to merge. (Contrast this with a plan view room temperature II-CVD microstructure of closely packed

"islands" that do not merge.) Secondary nucleation, growth and coalescence fill any voids between the islands, which leads to continuous film formation. The characteristic II-CVD microstructure at room temperature *cannot* follow this mechanism. The microstructure would have to percolate if it followed a nucleation and growth mechanism. The II-CVD columnar microstructure has very small variance in column diameters; in fact, it is similar to the cellular microstructure observed in alloy solidification due to constitutional supercooling.

Another fact that precludes Volmer-Weber growth in II-CVD relates to its dependence on the wetting angle of the adsorbate on the substrate. The experiments demonstrate that characteristic II-CVD microstructure arises on a wide variety of substrates – silicon nitride, amorphous carbon and copper – without any apparent effect on the microstructure. Furthermore, the XTEM samples in Chapter 3 show sharp microstructure transitions in response to significant change in deposition conditions.

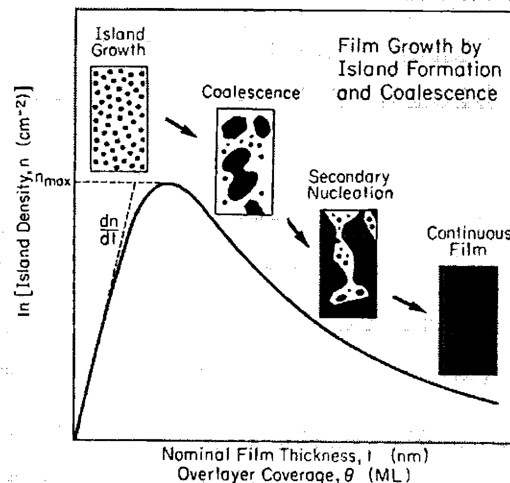

Figure 4.5: Schematic of island density (n) as a function of overlayer coverage during nucleation and growth. From [57].

In the 1950s, scientists attempted to tackle diffusion controlled metallurgical phenomena such as solidification, eutectoid (pearlitic) growth and discontinuous precipitation. The difficulty in formulating a mathematical solution was due to the fact that the diffusion equation becomes indeterminate because the growth velocity is a function of a length parameter. Attempts to solve these problems invoked criteria that have no real physical basis, such as maximum growth velocity or maximum free energy decrease. An example of this treatment is Cahn's model of cellular segregation reactions from 1958.[58] Cahn showed that the behavior of the cellular segregation reactions depend on the ratio of the mobility of the boundary to the diffusion coefficient along the boundary. The solution to the diffusion problem is indeterminate since it permits a range of growth velocities; therefore, Cahn assumed that growth velocity is proportional to the net free energy decrease due to the cellular segregation process. Cahn's model is revisited later in this chapter because his treatment of surface diffusion provides a foundation for the II-CVD microstructure model, albeit with different boundary conditions. Fortunately, many thin film processes, including II-CVD, do not suffer from this problem of indeterminateness because the growth velocity is imposed externally. In II-CVD the externally controlled ion-flux determines the growth velocity in the (desirable) ion-flux-limited regime.

In 1964, Mullins and Sekerka presented a classic paper that addressed cellular segregation in solidification processes from the perspective of morphological instability.[59] When growth of a stable phase occurs by migration of an interface between the stable and metastable phases, *the interface is subject to morphological instability whenever the region adjacent to the interface is either supersaturated or supercooled*. Consider iso-concentration profiles at a planar interface extending into a supersaturated solution. A perturbation of the interface then leads to a higher concentration gradient in the vicinity of this perturbation compared to the gradient at the planar interface. The increased concentration gradient leads to faster growth at the perturbation. An analogous argument accounts for cellular solidification of pure solids into supercooled liquids. Here

the temperature gradient increases in the vicinity of a perturbation of the planar interface. Capillarity serves to counteract morphological stability so that perturbations with a radius of curvature smaller than a critical value will not grow. Modeling the morphological instability is very complex because the boundary conditions introduce highly non-linear components. The boundary itself is dynamic and its motion couples to the solution of the problem. The breakthrough of Mullins and Sekerka's analysis was due to their linearizing of the entire system of equations.

Mullins and Sekerka solved the solidification problem by considering a solid-liquid interface that has been perturbed in the form of a periodic wave. The solidification involves a binary alloy with a concentration gradient in the melt and temperature gradients in both the melt and solid. They obtained the solution by developing partial differential equations that govern the transport of heat in the liquid and solid, and transport of solute in the liquid. They assumed that no diffusion occurs in the solid phase and the liquid/solid interface is at equilibrium. The local interface velocities calculated from heat flow relations must equal those evaluated from diffusion considerations. Furthermore, they must equal $v + (d\delta/dt)\sin\omega x$, where v is the velocity of the planar interface, δ is the amplitude of the perturbation, ω ($=2\pi/\lambda$) is the wave number, and x is the coordinate along the interface. The solution of the partial differential equations is quite complex. Please refer to the original paper [59] or a more recent, general analysis by Trivedi and Kurz, which extends the analysis to rapid solidification.[60] *The theoretical analysis leads to one overriding conclusion: whenever the sum of the solute and thermal diffusion lengths exceeds the capillary length, one expects a tendency toward morphological instability at sufficient undercooling or supersaturation.*

Morphological instability also arises in thin film deposition. Van den Brekel and Jansen presented a stability analysis of atmospheric pressure CVD (APCVD) that is analogous to Mullins and Sekerka's treatment.[61] The main difference in the treatment relates to heat transfer and diffusion through a laminar boundary

layer. Thus, there is not much difference in the solutions to the diffusion equations. The stability criterion relies on the magnitude of the gas phase concentration gradient to drive the growth process toward morphological instability. It also depends on the sign of the decomposition reaction of the gas precursor. They showed that an exothermic reaction on a substrate that is hotter than the gas encourages morphological instability, and vice versa for endothermic reactions. In another paper, Van den Brekel came to the interesting conclusion that CVD is inherently unstable.[62] His stability criterion predicts that there will always be perturbation frequencies that tend to grow. However, the analysis only applies capillarity as a stabilizing factor, so there is no consideration of surface diffusion. Note that the process conditions of II-CVD are very different from APCVD. In APCVD the precursor transport to the surface is diffusion driven; hence, it forms a boundary layer. In II-CVD the chamber pressure is only 10^{-5} torr and the local precursor pressure at the substrate is 0.5 mtorr. The lack of thermal or concentration gradients simplifies the model for II-CVD considerably compared to APCVD.

The vacuum conditions in II-CVD are similar to PVD (physical vapor deposition); however, the PVD deposition process is ballistic whereas II-CVD is *surface mediated*. Dirks and Leamy studied morphological instability in PVD on a particle level and suggested that columnar microstructure is due to self-shadowing of the vapor beam by the growing film.[63] Shadowing of lower asperites by higher protrusions tends to yield a higher deposition rate on the highest protrusions and their growth at the expense of smaller ones. Figure 4.6 illustrates this effect. Srolovitz applied perturbation theory to study morphological stability in vapor deposition.[64] He showed that a columnar microstructure results from a balance between shadowing and surface diffusion. Higher substrate temperature drives the process toward stability since the adatom mobility increases with temperature. Srolovitz's model predicts the transition temperature from zone I to zone II microstructure, as well as the length scales of both the unstable modes and the grain structure.

Porous columnar microstructure – so-called zone I microstructure – evolves at low temperature and high growth rates in PVD due to the aforementioned self-shadowing process. At intermediate temperature the microstructure develops columnar grains (zone II), which have metallurgical grain boundaries. Higher temperature leads to equiaxed microstructure (zone III) with minimum surface topography. *Il-CVD does not follow this behavior.* In fact, AFM (atomic force microscopy) maps from Chapter 3 indicate that the macroscopic surface becomes rougher at higher temperature.

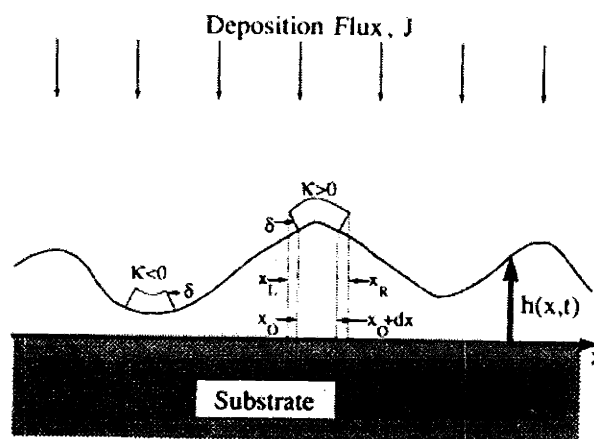

Figure 4.6: Columnar microstructure evolution via shadowing in PVD. K is the curvature of the surface and δ is an atomic radius. If the surface curvature is negative (K<0) then a surface element sees a smaller flux (J) of atoms, and vice versa. From [64].

These qualitative observations of film growth behavior in relation to substrate temperature constitute so-called structure zone models (SZM) for film growth. They are purely empirical and were introduced by Movchan and Demchishin.[65] Figure 4.7 illustrates the SZM by Thornton for PVD.[66]

On the other hand, high temperature does not necessarily lead to stability in CVD. For example, Chin et al. found that SiC deposition by CVD becomes strongly faceted at high temperature.[67] Viljoen investigated the effect of reactor conditions on the stability criteria.[68] He showed that the temperature effect depends on whether the process is diffusion controlled or reaction controlled. If

the process is reaction controlled, then an increase in temperature leads to morphological instability.

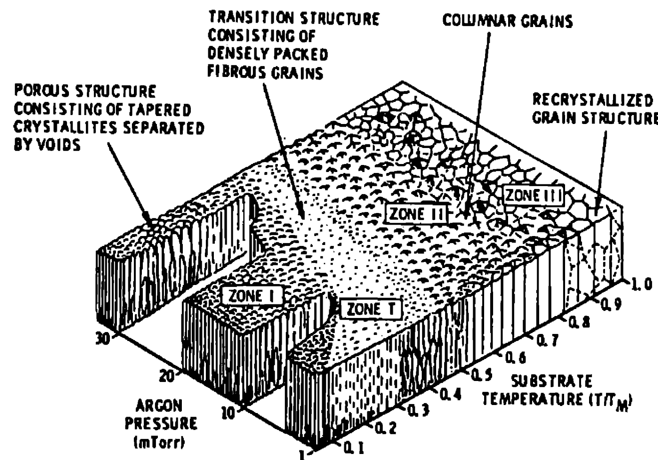

Figure 4.7: Structure Zone Model (SZM) for PVD by Thornton. The SZM plots the microstructure versus substrate temperature and the Argon gas pressure used in the sputter process. From [66].

The conclusion of this review of columnar growth in film deposition is that the mechanism of cellular growth in II-CVD is very different from both PVD and CVD. It does not have the concentration gradient in the gas phase that leads to classical morphological instability in CVD. In PVD the morphological instability is mainly due to self-shadowing, but this is impossible in II-CVD because the deposition process is not ballistic.

The author proposes the following mechanism for cellular growth in II-CVD. The cellular growth process in II-CVD involves rejection of carbon at the evolving surface of the copper column. As the II-CVD process decomposes the precursor molecules, copper and carbon adatoms form on the surface. Considering conditions at the tip of an evolving column, copper adatoms bond to the copper column while the carbon adatoms are free to diffuse along the surface. The diffusion distance of carbon adatoms before the surface effectively becomes

"frozen in" as part of the bulk primarily determines the characteristic column diameter.

Ro showed that high carbon fraction leads to the breakdown of cellular growth in II-CVD using the DMG(hfac) precursor to deposit gold.[16] *Clearly, the characteristic radius of the columnar structure has become too small and capillarity resists cellular growth.* Thus, the mechanism requires a substantial majority phase of the metal. The complete breakdown of cellular growth does not happen in the copper system, although deposition at high ion flux in the gas-flux-limited regime as well as deposition at low voltage both exhibited localized areas without the characteristic regular microstructure. Furthermore, the diameters of columns that do form are significantly smaller compared to those deposited at the same temperature under preferred conditions. On the other extreme, complete removal of carbon with the H-atom beam does not produce cellular growth. (See Chapter 3.7.)

4.3 Surface Diffusion

This analysis suggests that the column radius is sensitive to the carbon fraction of the growing film. However, the quantitative metallography shows unequivocally that the column radius stays constant with increasing growth rate at constant temperature, while the XPS data indicates an increase in carbon fraction with the growth rate. The explanation for this behavior relates to the effect of ion bombardment on surface diffusion. In other words, the increased ion flux at higher grow rates also increases the surface diffusion rate. Remember that the film growth rate scales linearly with ion flux in the ion-flux-limited regime.

The literature documents enhanced surface diffusion of adatoms for PVD with simultaneous ion bombardment. Marinov investigated the effect of ion

bombardment on three-dimensional Volmer-Weber growth of silver thin films.[69] Simultaneous ion bombardment led to larger islands with greater inter-island separation. He argued that this is due to both enhanced surface diffusion as well as sputtering of subcritical islands. Marinov's analysis was only qualitative since it is impossible to separate the two effects that lead to larger island formation. Cotell et al. revisited Marinov's experiments and did not discover the same effect.[70] The nature of nucleation and growth introduces the uncertainty of substrate effects; therefore, it is not really a good process for analysis of surface diffusion.

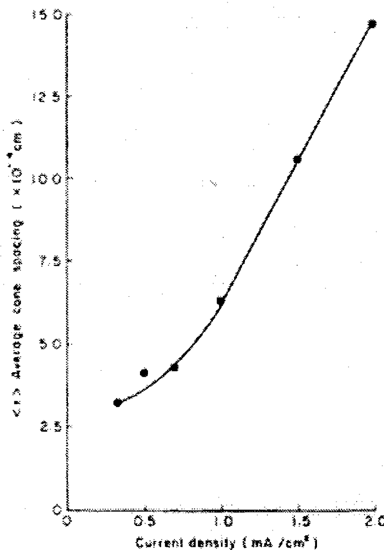

Figure 4.8: From Rossnagel et al.: increase in average cone spacing of Mo versus ion beam current density (1000 eV Ar) in ion beam texturing experiment. From [72].

Rossnagel et al. investigated the enhancement of surface diffusion due to ion bombardment during ion beam texturing of surfaces.[71] This process involved the simultaneous seeding of a surface and high ion flux sputtering. In this system the ion flux greatly exceeds the arrival rate of depositing adatoms. The adatoms diffuse across the surface and form islands, which is analogous to the initial stage of Volmer-Weber growth. The islands that continue to grow are preserved

by a greater flux of adatoms across the surface than removed by sputtering. The islands grow into cones over time and the spatial density of these cones is a measure of the surface diffusion. Rossnagel et al. demonstrated approximately linear increase in average cone spacing of Mo with increasing ion flux (1000 eV Ar ion beam) at constant substrate temperature beyond some level of ion flux.[72] (Figure 4.8.)

Thus, there is evidence in the scientific literature that there is enhancement of surface diffusion that scales with the flux of ion bombardment. The ion-enhanced diffusion probably stems from collision cascades that excite surface phonons. For II-CVD, consider carbon adatoms at an excited state and consider a linear increase in the surface diffusion coefficient pre-exponential. The surface should be viewed as a "near-surface region"[73] of several atomic layers above what is considered to be the bulk of the evolving film. There is no appreciable bulk diffusion in the temperature range of II-CVD; therefore, the evolving microstructure represents a time history of the surface. The lack of thermal and concentration gradients in the near-surface region simplifies the mathematics of the model as it uses averaged compositions of carbon and copper. This formulation establishes a link from the surface kinetic model in the sense that one can incorporate the average film composition predicted by the surface kinetic model into the microstructure model.

4.4 The Microstructure Model

This section formulates a microstructure model for II-CVD, which predicts the observed cellular growth and reproduces the change in columnar diameter as the experimental parameters change. The microstructure model has to predict independence of column diameter with increasing film growth rate and ion flux.

So far, we have stressed surface diffusion as the governing mechanism. The empirical data must fit a Fickian formulation of surface diffusion, which yields a surface diffusion constant ($\tilde{D}_s$) – also known as the diffusivity – for the mechanism.

It is useful to consider the classical treatment of Fickian diffusion. Consider a surface atom that has to overcome an energy barrier (E_A). If the atom is oscillating in its potential well with a frequency v_0 (attempt frequency), then the probability that it will get over the barrier is equal to $v_0 \exp(-E_A/kT)$ where k is Boltzmann's constant. Now consider two planes in the X direction that are separated by an atomic distance (a). If c is the concentration of impurity atoms, then there are ac atoms in a plane per unit area and the net number diffusing atoms is:

$$-v_0 \exp(-E_A/kT) a \, \mathrm{d}(ac)/\mathrm{d}X.$$

Comparing this expression to Fick's first law:

$$j = -\tilde{D}_S(\partial c / \partial x),$$

then $\tilde{D}_S \approx v_0 a^2 \exp(-E_A / kT) \approx D_0 \exp(-E_A / kT)$

This is the classical, simplified expression for diffusion via a nearest-neighbor mechanism. The expression requires that an Arrhenius plot of column radius versus 1/T yields an activation energy for diffusion. However, it will be shown that the derived expression for II-CVD is more complicated, as it is not possible to express the equation as a simple product of a temperature independent component and a temperature dependent component. *This is due to the fact that*

the incoming concentration of impurity is also a function of temperature in II-CVD.

The pre-exponential part of the diffusion coefficient is critical in explaining the empirical independence of microstructure with respect to film growth rate. The ν_o term represents the attempt frequency, which is approximated as the Debye frequency – approximately 10^{13} s^{-1}. Thus, D_0 should be approximately 10^{-3} cm^2/s if this simple model of surface diffusion holds – implicitly, a random walk between nearest-neighbor sites.[74] The ion flux will influence this attempt frequency by putting the adsorbed, migrating surface atoms into an excited state. In other words, the ion flux induces surface phonons that serve to increase the vibrational attempt frequency of the adsorbed atoms. *The model assumes that the attempt frequency scales linearly with the ion flux.* This constitutes a key assumption for the microstructure model.

4.4.1 Surface Diffusion Modeling In The Literature

Cahn modeled eutectoid growth of pearlite in the Fe-C system and showed that surface diffusion controls the phase segregation.[58] Atzmon et al. revisited this treatment for phase separation in film growth and columnar growth for PVD co-deposition of Al-Ge.[75,76] This recent analysis represents the first systematic study of multicomponent film growth. The governing steady-state equation for surface diffusion from Cahn, using Atzmon's notation:

$$\frac{\partial c}{\partial t} = \tilde{D}_s \nabla_s^2 c + \mathrm{v}\left(\frac{c_0 - c}{\delta}\right)$$

The "s" subscript designates the surface; $\tilde{D}_s$ is the surface diffusion constant; c is the solute concentration (carbon for II-CVD); c_0 is the composition in the parent phase (i.e., composition arriving from gas phase for film growth); v is the

growth rate; δ is the thickness of the region where surface diffusion is active. The characteristic length scale of the problem is:

$$\rho = \sqrt{\frac{\tilde{D}_S \delta}{v}}$$

In eutectoid growth the system selects its own growth rate, so Cahn had to invoke a questionable free energy reduction argument to solve the problem and determine the length scale. Fortunately, thin film growth has an externally imposed growth rate, which simplifies the problem considerably. Atzmon investigated phase separation for co-evaporated Al-Ge, which forms Ge-rich columnar "domains". The problem was solved in cylindrical coordinates. However, the morphology is the converse of II-CVD: the columnar domains represent the minority phase. The essential boundary condition for Atzmons's model is $\frac{\partial c}{\partial r} = 0$ for r >> R where R is the column diameter. *This is not applicable in II-CVD where the spacing between the columns is much smaller than the column diameter.*

4.4.2 Microstructure Model for II-CVD

Appendix B presents the full derivation of the diffusion equation for the II-CVD system. This section presents the fundamental steps in the derivation. The surface diffusion equation is solved at steady-state in cylindrical coordinate space where r = R is the column diameter, r = 0 is the column center and c is the carbon atomic concentration:

$$\frac{\partial c}{\partial t} = \frac{\tilde{D}_s}{r}\left(r\frac{\partial^2 c}{\partial r^2} + \frac{\partial c}{\partial r}\right) - \frac{vc}{\delta} + \frac{vc_0}{\delta} = 0$$

This represents a Fickian diffusion equation at the surface plus a source term ($\frac{vc_0}{\delta}$) for a net deposition yield with composition c_0. ($-\frac{vc}{\delta}$) represents a sink term as material becomes part of the bulk when the film boundary moves along. The equation is multiplied by r^2 to express it as a Bessel function and the solution is:

$$c = C_1 I_0(\frac{r}{l}) + C_2 K_0(\frac{r}{l}) + c_0$$

where $l = \sqrt{\frac{\tilde{D}_S \delta}{v}}$ and I_0 is a modified Bessel function of order 0.

Boundary conditions:

From symmetry, $\frac{\partial c}{\partial r} = 0$ at $r = 0$.

$c \approx 0$ at r = R, i.e. pure copper at the column/matrix boundary where carbon has the shortest diffusion distance. Carbon has infinitesimal solubility in copper: 0.04 % at the peritectic temperature. (See Figure 4.9.) Extrapolation of the Cu-C phase diagram to room temperature suggests that the saturation fraction of C in Cu is less than 1×10^{-5} (atomic fraction).

One cannot apply any boundary conditions to the matrix (area surrounding the columns) since it is a two-phase region composed of copper and amorphous carbon. *STEM analysis showed that the matrix contains the excess of copper that is a function of the deposition conditions.* (See Chapter 3.9.)

Cu-C Phase Diagram

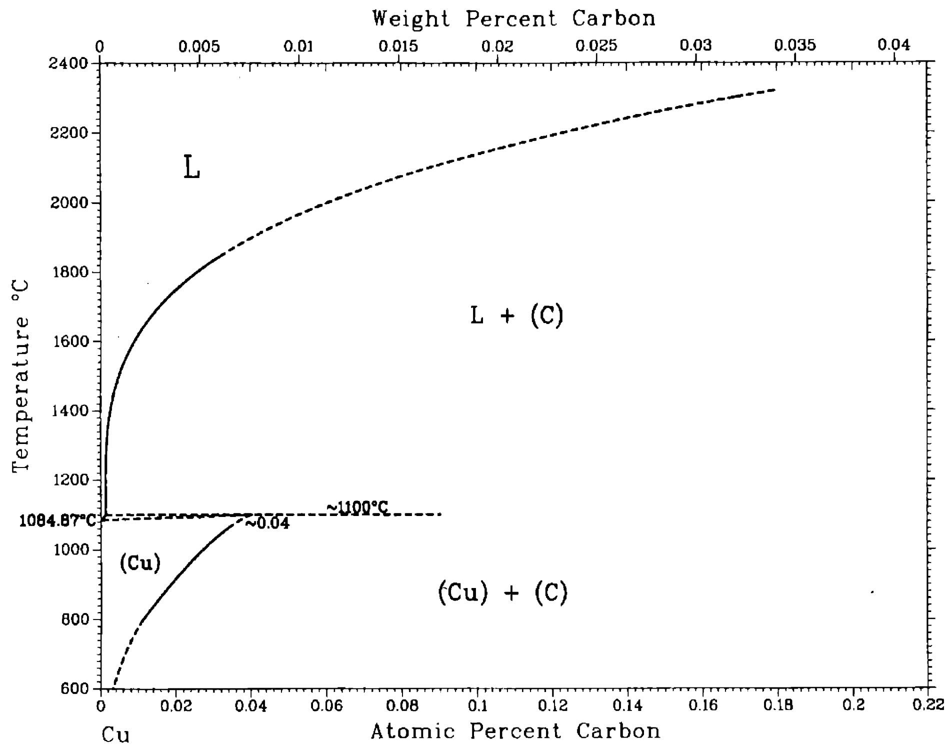

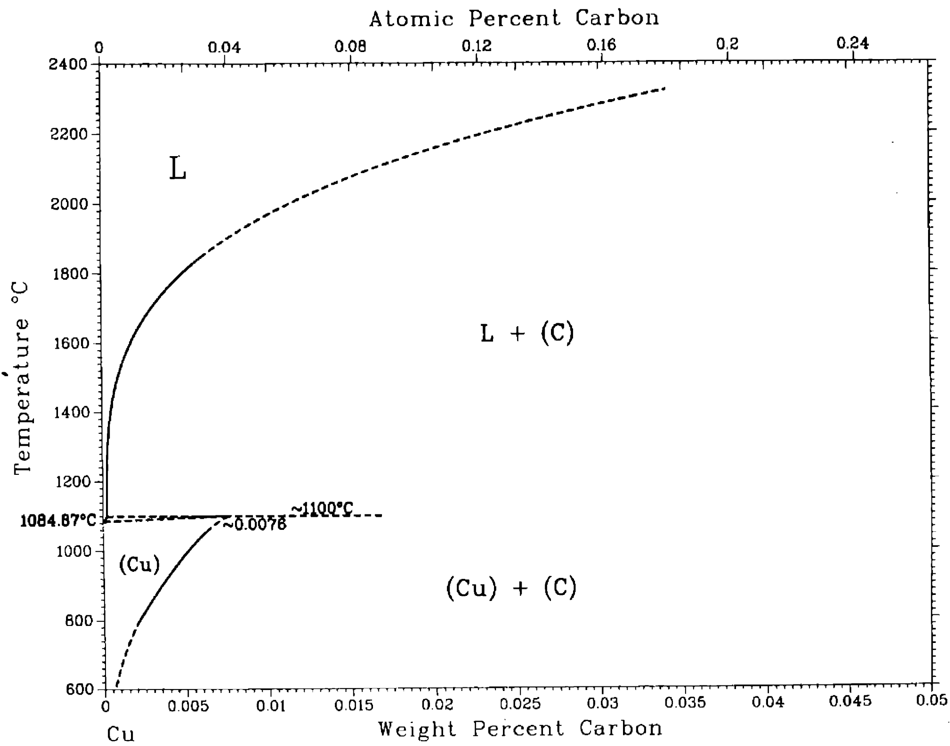

Figure 4.9: Cu-C phase diagram, constructed from thermodynamic data. Note that the peritectic solubility of C in Cu is only 0.04 atomic %.From [77].

The limit for the carbon fraction at r = 0, which represents the center of a copper column, is at its maximum. The model requires some level of super-saturation. The choice is somewhat arbitrary, but a selection within two orders of magnitude of the approximate equilibrium concentration is reasonable: 1×10^{-3} atomic fraction. This value is also consistent with the detection limit of XPS quantitative analysis. Fortunately, the exact magnitude of this small number has negligible impact on the solution of the equations due to the form of the modified Bessel function (I_0).

So, $c = 1 \times 10^{-3}$ at $r = 0$:

$$I_0\left(\frac{R}{l}\right) = \frac{1}{1 - \frac{1 \times 10^{-3}}{c_0}}$$

l is re-expressed as a product of constant and ion flux dependent components:

$$l = \sqrt{\frac{\tilde{D}_S \, \delta}{v}} = \sqrt{\exp\left(-E_A / kT\right) \delta} \sqrt{\frac{D_0}{v}} \qquad [4.2]$$

D_0 (the diffusion constant's pre-exponential) and v are functions of the ion flux. The model assumes that D_0 scales linearly with the measured ion flux *(i),* which is reasonable from an atomistic view of diffusion. The pre-exponential incorporates the jump frequency of the atoms. As discussed earlier, the model assumes that the ion-induced phonons increase this jump frequency. The $\sqrt{\exp\left(-E_A / kT\right) \delta}$ term is constant at any given temperature. *Thus,* $\sqrt{\frac{i}{v}}\, I_0^{-1}\left(1 - \frac{1 \times 10^{-3}}{c_0}\right)^{-1}$ *should be approximately constant for a range of growth rates at constant temperature if the model satisfies the experimental data.*

4.4.3 Activation Energy for Surface Diffusion

The literature documents that experimental measurement of the surface diffusion pre-exponential is very difficult and reasonably reliable data only started to appear in the late 1980s. However, Ehrlich made an important argument in a review paper: reliable experiments using modern techniques invariably point to a pre-exponential in the vicinity of 10^{-3} cm^2/s when surface diffusion is the controlling mechanism.[74] *These results are independent of substrate and diffusing species.*

As noted earlier, the solution of the diffusion equation for II-CVD does not allow for simple graphing of 1/T versus column diameter to determine the activation energy. However, this model for II-CVD postulates a surface diffusion mechanism, which therefore allows determination of the activation energy by assuming that the pre-exponential is in the 10^{-3} cm^2/s range. The model further assumes an approximately linear relationship between growth rate (or ion flux) and the diffusion pre-exponential in order to account for the independence of column diameter in relation to growth rate as depicted in Figure 3.16.

Growth Rate (function of ion flux)	0.1 Å/s	0.5 Å/s	1 Å/s
Calculated Average E_A	0.50 eV	0.46 eV	0.43 eV

Table 4-2: Calculated average activation energy (E_A) based on a diffusion pre-exponential that scales from 10^{-4} to 10^{-3}, corresponding to 0.1 Å/s and 1 Å/s respectively.

Temperature	Calculated E_A		
	0.1 Å/s	0.5 Å/s	1 Å/s
25°C	0.48 eV	0.44 eV	0.41 eV
43°C	0.48 eV	0.46 eV	0.43 eV
61°C	0.50 eV	0.49 eV	0.46 eV

Table 4-3: Calculated activation energy for different temperatures and growth rates. Following the underlying assumption of the model, the pre-exponential is 10^{-4}, $5X10^{-3}$ and 10^{-3} for 0.1 Å/s, 0.5 Å/s and 1 Å/s, respectively.

The data in Table 4-2 shows that the calculated activation energy based on the aforementioned assumptions is in the 0.4 to 0.5 eV range. The calculated activation energy decreases slightly with ion flux (growth) rate because the effect of ion flux on the diffusion pre-exponential is not strictly linear – the linearity is a reasonable approximation. The calculated activation energy for a specific growth rate exhibits a slight increase in calculated activation energy with temperature. (Table 4-3.) This is due to the gradual onset of thermal CVD as temperature increases. Chapter 4.5 examines the onset of thermal CVD in detail and Chapter 3 demonstrated that temperatures above 60°C significantly altered the microstructure evolution due to the thermal CVD growth component.

4.4.4 Testing The Model: Ion-Flux-Limited Regime

The validity of the experimental data is tested in the ion-flux-limited regime at temperatures up to 61°C, which is the limit before the onset of thermal CVD. In this range, the model should predict that the column diameter is independent of growth rate. The results are presented in tables, which include:

- Experimental data
- Microstructure model predictions
- Kinetic model predictions

The microstructure model is normalized to the 0.5 Å/s deposition rate because the monitored experimental data are typically quite stable at this growth rate.

The data at 25°C and 61°C fit the model very well. There are no XPS composition data at 0.3 Å/s so the calculation uses a carbon concentration predicted by the surface kinetic model, which also serves to demonstrate the possibility of effectively linking the models. The extended kinetic model also relies on XPS data to determine K_{des}, so this value has to be extrapolated from values calculated at other growth rates. Figure 4.3 suggests that this method should be reliable.

Comparison of the kinetic model's growth rate with the measured growth rate serves as a yardstick for possible errors in the XPS data. The model becomes very sensitive to error in XPS data above 90% Cu. At 61°C the model appears to underestimate the column diameter by approximately 5%. If the XPS quantitative analysis had indicated 95% Cu then the model would overestimate the Cu fraction by 11%. (The XPS data are rounded to the nearest percent.)

At 43°C the data do not fit the model as well. This is also due to the sensitivity to error in the XPS data; qualitatively, 93% Cu appears to be higher than what is expected at 0.1 Å/s and 81% Cu is lower than expected at 0.5 Å/s. The analysis shows that the column diameter based on the composition predicted by the kinetic model (90% Cu) yields a better fit. Figure 4.10 and Figure 4.11 provide graphical illustrations of the fit of the data to the microstructure model.

Data:				
rate (Å/s)	0.1	0.3	0.5	1.0
ion flux ($\mu A/cm^2$)	1.37	5.85	10.6	21.6
Cu column diameter (nm)	**14.5**	**14.4**	**14.5**	**13.6**
%Cu columns	67.8	65.9	65.8	66.5
%Cu (XPS)	85	NA	75	70
Microstructure model:				
$\sqrt{\frac{i}{v}}\, I_0^{-1}\left(1 - \frac{1\text{x}10^{-3}}{c_0}\right)^{-1}$	0.603	0.608*	0.597	0.567
Cu column diameter (nm)	**14.7**	**14.6**	**14.5**	**13.6**
Kinetic model:				
%Cu	85	78.9	75.6	69.9
rate (Å/s)	0.09	0.3	0.50	0.94
empty sites (%)	0.7	2.2	3.5	5.7
kdes($\#/cm^2s$)	2.70E+14	5.00E+14	7.00E+14	1.00E+15

(*) Using %Cu from Kinetic model.

Table 4-4: Microstructure model and associated data at 25°C

Data:				
rate (Å/s)	0.1	0.3	0.5	1.0
ion flux (μA/cm^2)	1.2	2.4	9.6	19.5
Cu column diameter (nm)	**22.6**	**21.5**	**21.8**	**20.3**
%Cu columns	84.7	NA	80.2	80.9
%Cu (XPS)	94	[94]*	91	89
Microstructure model:				
$\sqrt{\frac{i}{v}}\, I_0^{-1}\left(1 - \frac{1\text{x}10^{-3}}{c_0}\right)^{-1}$	0.900	0.900	0.928	0.845
Cu column diameter (nm)	**21.4**	**21.4**	**21.8**	**19.9**
Kinetic model:				
%Cu	96.4	94.8	91.8	87.8
rate (Å/s)	0.09	0.16	0.51	1.04
empty sites (%)	0.64	1.3	3.9	8.0
kdes(#/cm^{2}s)	1.00E+15	1.4E+15	3.00E+15	3.8E+15

(*) Using %Cu from Kinetic model.

Table 4-5: Microstructure model and associated data at 61°C.

Data:				
rate (Å/s)	0.11	0.29	0.52	1.0
ion flux (μA/cm^2)	1.4	5.5	11.3	24.1
Cu column diameter (nm)	**16.9**	**16.5**	**16.9**	**17.3**
%Cu columns	75.3	74.0	74.6	73.8
%Cu (XPS)	93	NA	81	78
Microstructure model:				
$\sqrt{\frac{i}{v}}\, I_0^{-1}\left(1 - \frac{1\text{x}10^{-3}}{c_0}\right)^{-1}$	0.857 0.716*	0.753	0.678	0.663
Cu column diameter (nm)	**21.3/ 17.8***	**18.8****	**16.9**	**16.5**
Kinetic model:				
%Cu	89.8	87.2	84.6	77.0
rate (Å/s)	0.10	0.29	0.55	1.0
empty sites (%)	0.7	2.2	4.3	7.4
kdes(#/cm^{2}s)	6.00E+14	1.00E+15	1.6E+15	3.00E+15

(*) For 90% Cu

(**) Using %Cu from kinetic model

Table 4-6: Microstructure model and associated data at 43°C.

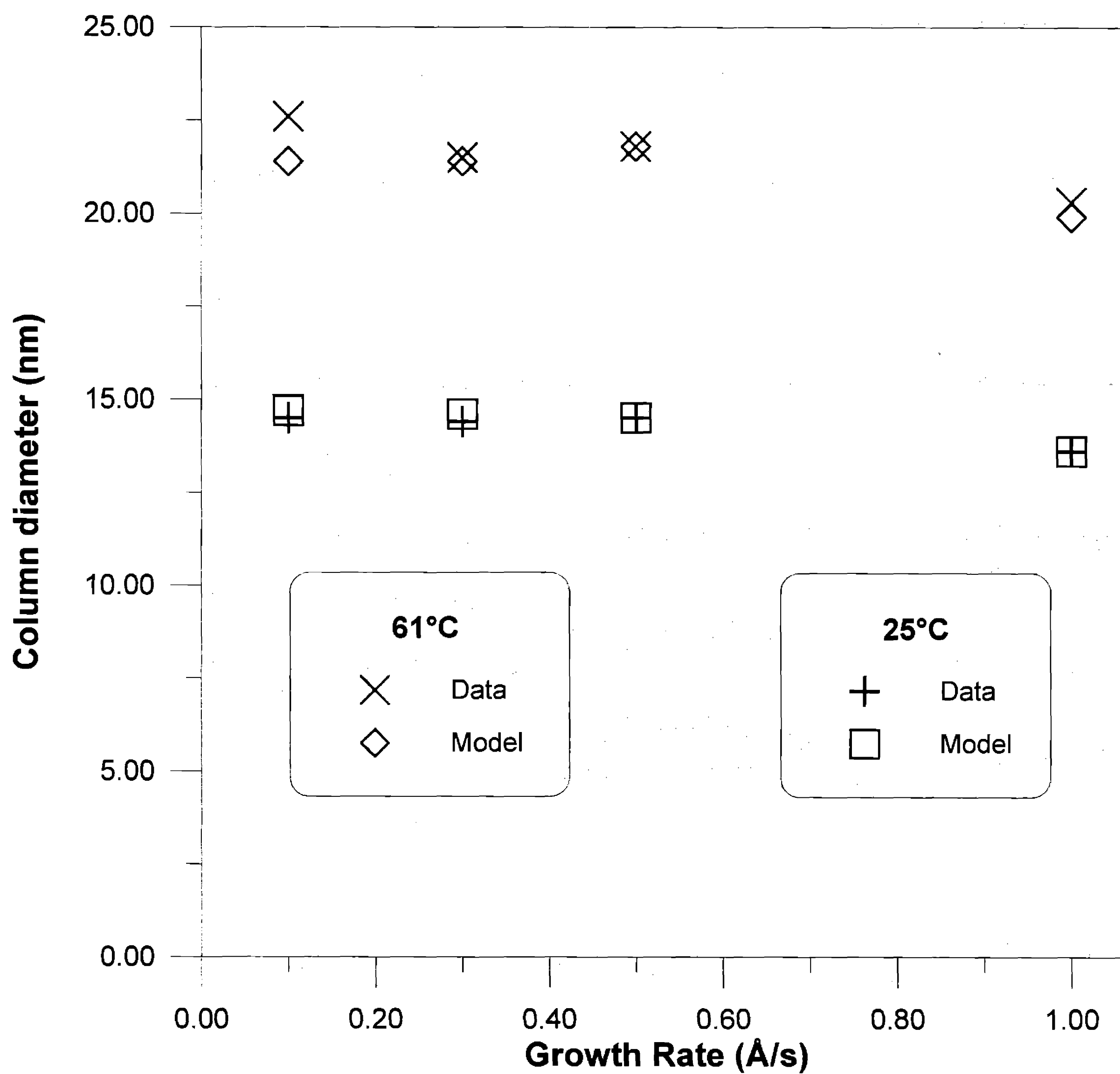

Figure 4.10: Graphical comparison of measured column diameters to microstructure model at 61°C and 25°C. Note the excellent fit.

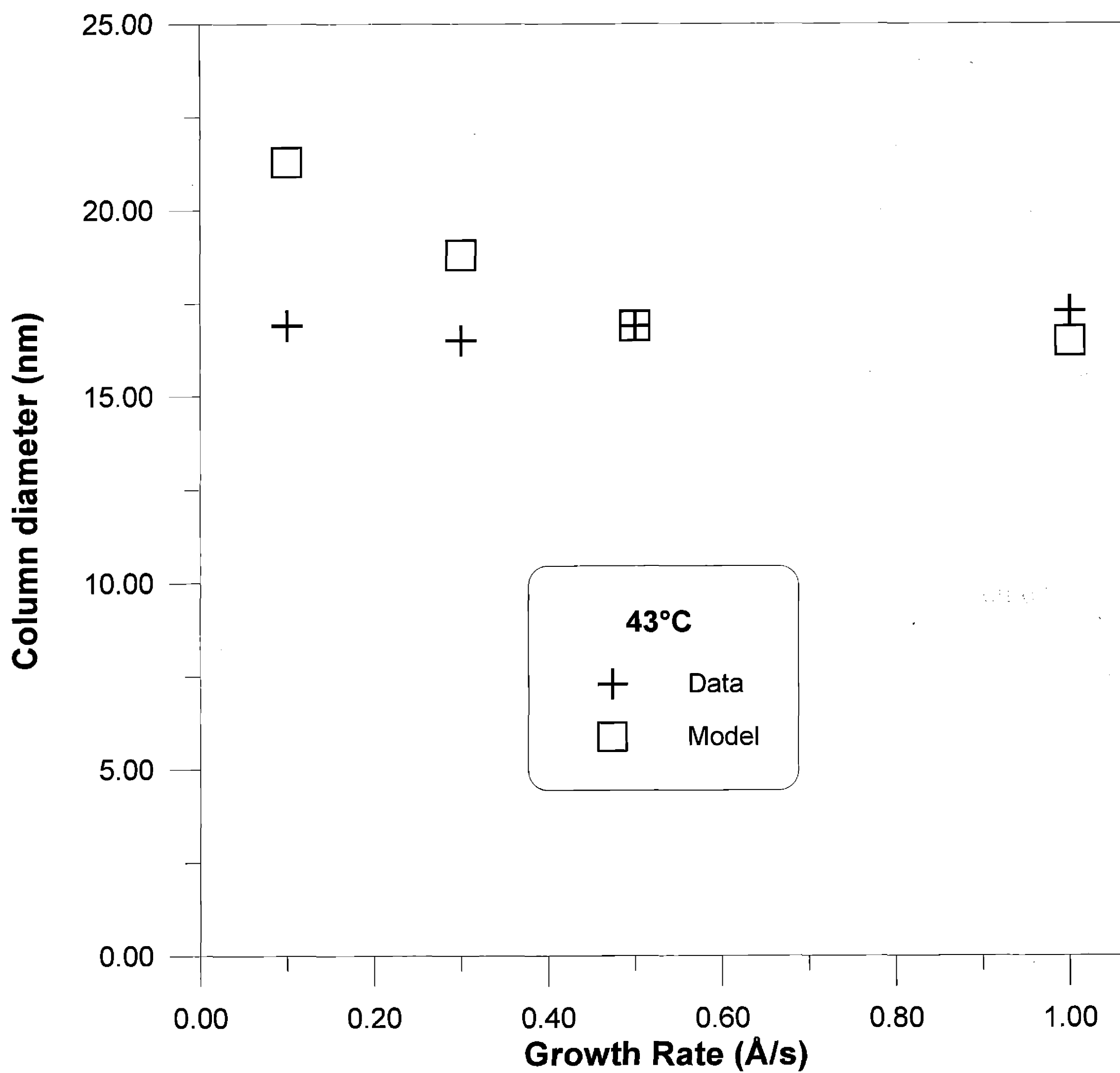

Figure 4.11: Comparison of measured column diameters to microstructure model at 43°C.

4.4.5 Testing The Model: Ion Beam Voltage

Consider the effect of ion beam voltage within the context of the microstructure model. Figure 3.10 illustrates that II-CVD at 200V and 300V produces much smaller column diameters and even extinguishes columnar growth at 200V and 25°C. The effect is mechanistic because the same carbon fractions would produce much larger column diameters at 500V. With regard to this model, the lower voltage does not bring the carbon adatoms to a sufficiently excited state and this does not enhance the surface diffusion to the same extent. However, increasing voltage also reduces the carbon fraction and the increase in column diameter is not as marked between 500V and 1000V. (Figure 3.38.)

The microstructure model predicts an increase in column diameter due to the increased copper fraction at higher ion beam voltage. The question is whether it is sufficient to account for the increase in column diameter. Table 4-7 investigates the model prediction by comparing deposition at 300V, 500V and 1000V at 25°C. Table 4-8 compares 500V and 1000V at 43°C. Within the margin of error, the model predicts that the increase in column diameter is due to the increase in copper fraction between 500V and 1000V. This result suggests that the ion enhanced surface diffusion does not depend on ion beam voltage beyond some limit in the range between 300V and 500V. Recall that the model must also be applicable to II-CVD at the much higher voltages of a FIB (25 keV) that Della Ratta used in his work, or an implanter (70 keV) that Ro used for some of his experiments.[33,16] The model would not be satisfactory if it predicted a continuous increase in surface diffusion with increasing ion beam voltage.

Data:	300V	500V	1000V
rate (Å/s)	0.3	0.3	0.3
ion flux ($\mu A/cm^2$)	5.6	5.85	5.6
Cu column diameter (nm)	**10.7**	**14.4**	**16.1**
%Cu (XPS)	68	79	82
Microstructure model:			
$\sqrt{\frac{i}{v}}\, I_0^{-1}\left(1 - \frac{1\text{x}10^{-3}}{c_0}\right)^{-1}$	0.576	0.608	0.645
Cu column diameter (nm)	**11.3**	**14.4**	**15.7**

Table 4-7: Investigating model at 25°C and 0.3 Å/s at 500V and 1000V.

Data:	500V	1000V
rate (Å/s)	0.29	0.33
ion flux ($\mu A/cm^2$)	5.5	5.5
Cu column diameter (nm)	**16.5**	**18.2**
%Cu (XPS)	87	90
Microstructure model:		
$\sqrt{\frac{i}{v}}\, I_0^{-1}\left(1 - \frac{1\text{x}10^{-3}}{c_0}\right)^{-1}$	0.753	0.819
Cu column diameter (nm)	**16.5**	**18.0**

Table 4-8: Investigating model at 43 and 0.3 Å/s at 500V and 1000V.

4.4.6 Testing The Model In the Gas-Flux-Limited Regime

In the gas-flux-limited regime the deposition conditions are a function of gas flux, ion flux and substrate temperature. The ratio of ion flux to growth rate (i/v) is large compared to the ion-flux-limited regime. Increased ion flux enhances surface diffusion, which leads to larger column diameters. On the other hand, the gas-flux-limited regime produces films with higher carbon fractions, which tends toward smaller column diameters. The microstructure model captures the fact that these two effects tend to balance in the ion-flux-limited regime. The gas-flux-limited regime exhibits variance in column diameter at any given temperature.

Unfortunately, the deposition conditions in this regime were not exactly reproducible because the deposition apparatus did not allow for accurate monitoring of the gas flux. Therefore, it is not possible to confidently compare the microstructure on a TEM grid to the quantitative XPS analysis on a Si_3N_4 coated silicon die. However, considering the large ion flux to growth rate ratio it is reasonable to assume that there is very little copper outside the columns. Therefore, the volume fraction of copper columns determined by quantitative microscopy – after converting it to atomic fraction – serves as a fair estimate of the atomic fraction of copper. The model testing uses the column diameter measured at 0.5 Å/s in the ion-flux-limited regime as the baseline for each temperature range.

Table 4-9 and Table 4-10 show that the microstructure model works reasonably well at lower ion fluxes, but then it becomes progressively worse as the ion flux increases. The model over-predicts the column diameters at high ion flux. There are a number of plausible explanations. The model assumes a linear dependency of the diffusion constant's pre-exponential on the ion flux. This represents an initial guess that appears to work quite well in the ion-flux-limited regime. Possibly, the relatively high ion fluxes bring out the real non-linearity. It may also be due to a geometric effect in the sense that the carbon fraction

dictates that the microstructure cannot accommodate the column diameter predicted by the model. Finally, it is important to reiterate that the analysis relies on an estimate of the film composition.

Data:	Ion flux ltd.	Gas flux ltd.	Gas flux ltd.
rate (Å/s)	0.5	0.24	0.43
ion flux (μA/cm^2)	10.6	10.6	21.9
Cu column diameter (nm)	**14.5**	**14.2**	**12.4**
%Cu columns	65.8	64.9	52.5
Microstructure model:			
$\sqrt{\frac{i}{v}}\, I_0^{-1}\left(1 - \frac{1\text{x}10^{-3}}{c_0}\right)^{-1}$	0.597	0.634	0.650
Cu column diameter (nm)	**14.5**	**15.1**	**15.8**

Table 4-9: Comparison of measured column diameters to microstructure model in the gas-flux-limited regime at 25°C.

Data:	Ion flux ltd.	Gas flux ltd.	Gas flux ltd.	Gas flux ltd.
rate (Å/s)	0.52	0.18	0.33	0.34
ion flux (μA/cm^2)	11.3	7.2	16.7	29.1
Cu column diameter (nm)	**16.9**	**19.8**	**17.0**	**14.5**
%Cu columns	65.8	73.0	70.9	59.3
Microstructure model:				
$\sqrt{\frac{i}{v}}\, I_0^{-1}\left(1 - \frac{1\text{x}10^{-3}}{c_0}\right)^{-1}$	0.678	0.770	0.796	0.836
Cu column diameter (nm)	**16.9**	**19.2**	**19.8**	**20.8**

Table 4-10: Comparison of measured column diameters to microstructure model in the gas-flux-limited regime at 43°C.

4.5 "High" Temperature II-CVD

The growth process becomes a mixed regime of II-CVD and thermal CVD above 61°C. Recall that thermal CVD researchers cite 130°C as the lower limit for thermal CVD of copper with the Cu(I)hfac(VTMS) precursor.[48] The relative contribution of thermal CVD is, of course, larger for low ion flux II-CVD. The invariance of column diameter in the ion-flux-limited regime no longer holds, as it tends to be slightly larger at lower growth rates. Nevertheless, cellular growth still appears to be the controlling mechanism at 100°C where XPS analysis indicates that there is less than 1% carbon. The model also becomes sensitive to experimental error at higher temperatures because the difference in carbon fraction is comparable to the experimental error of the XPS analysis.

The synergistic effects at high temperature do deserve some attention. At 100°C and 1.1 $\mu A/cm^2$ the II-CVD growth reaches 0.8 Å/s whereas the equivalent growth rate at room temperature would be less than 0.1 Å/s. However, the thermal CVD contribution is not linear; its intrinsic growth rate is nowhere near this level and it appears to decay slowly over time.

Figure 4.12 and Figure 4.13 illustrate some rate experiments that investigate this phenomenon. The runs followed the same procedure as the adsorption experiments presented in Chapter 3. The vacuum system was pumped down to 1×10^{-8} torr and the QCM substrate was sputter cleaned before starting the experiment. Notice that the deposition rate started out at an appreciable level and then decayed slowly to an approximate steady-state rate of 0.05 Å/s. The initial rate was 0.15 Å/s at 79°C and 0.35 Å/s at 100°C. This suggests that carbonaceous byproduct builds up on the substrate and inhibits deposition. The thermal energy in this temperature range is sufficient to decompose the precursor molecule but the temperature is not high enough to desorb the byproduct at an appreciable rate. *Therefore, byproduct desorption is the rate*

limiting step that inhibits thermal CVD. Also, the synergistic effect observed in II-CVD is due to ion assisted desorption of the byproduct.

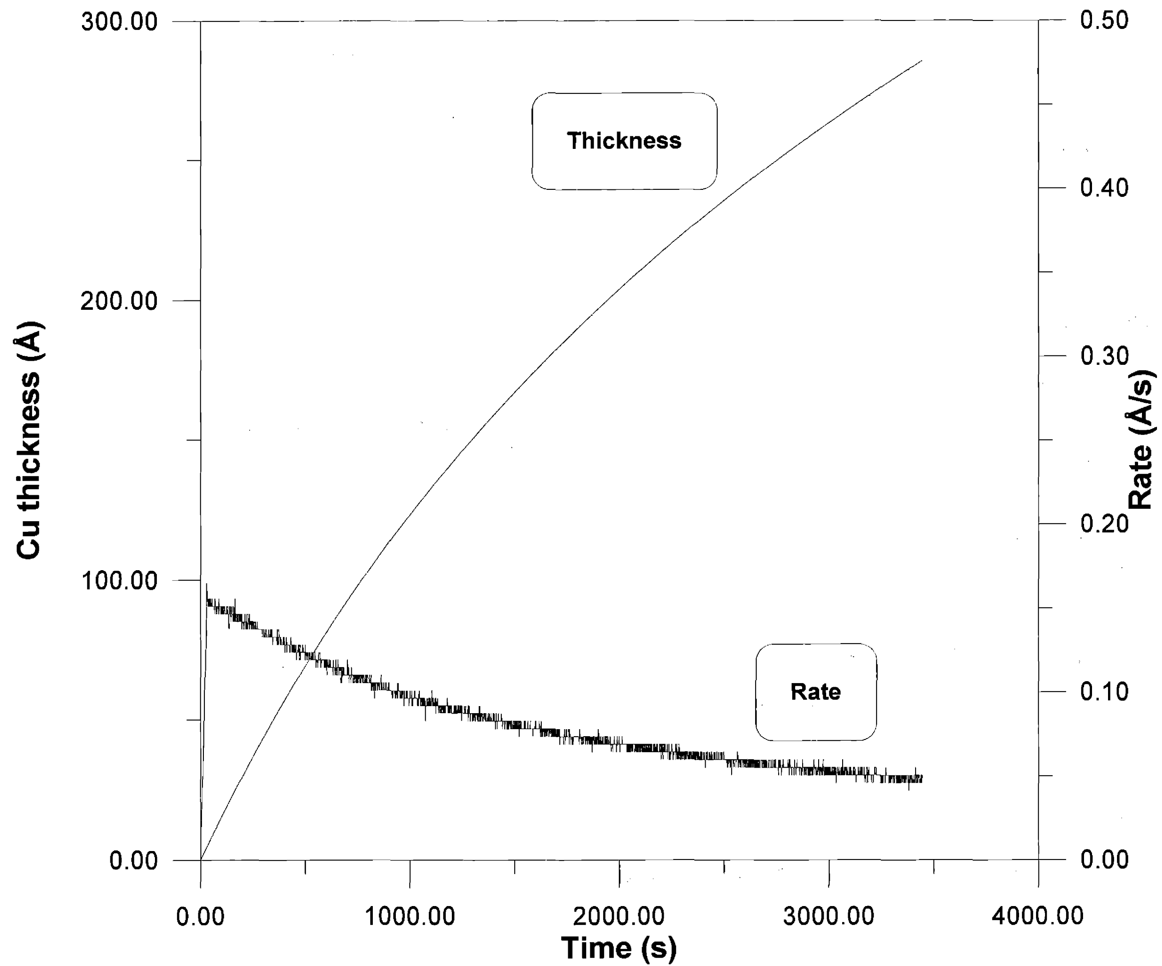

Figure 4.12: Rate and film thickness versus time for thermal CVD at 79°C on QCM substrate. The surface was sputter cleaned before starting the deposition.

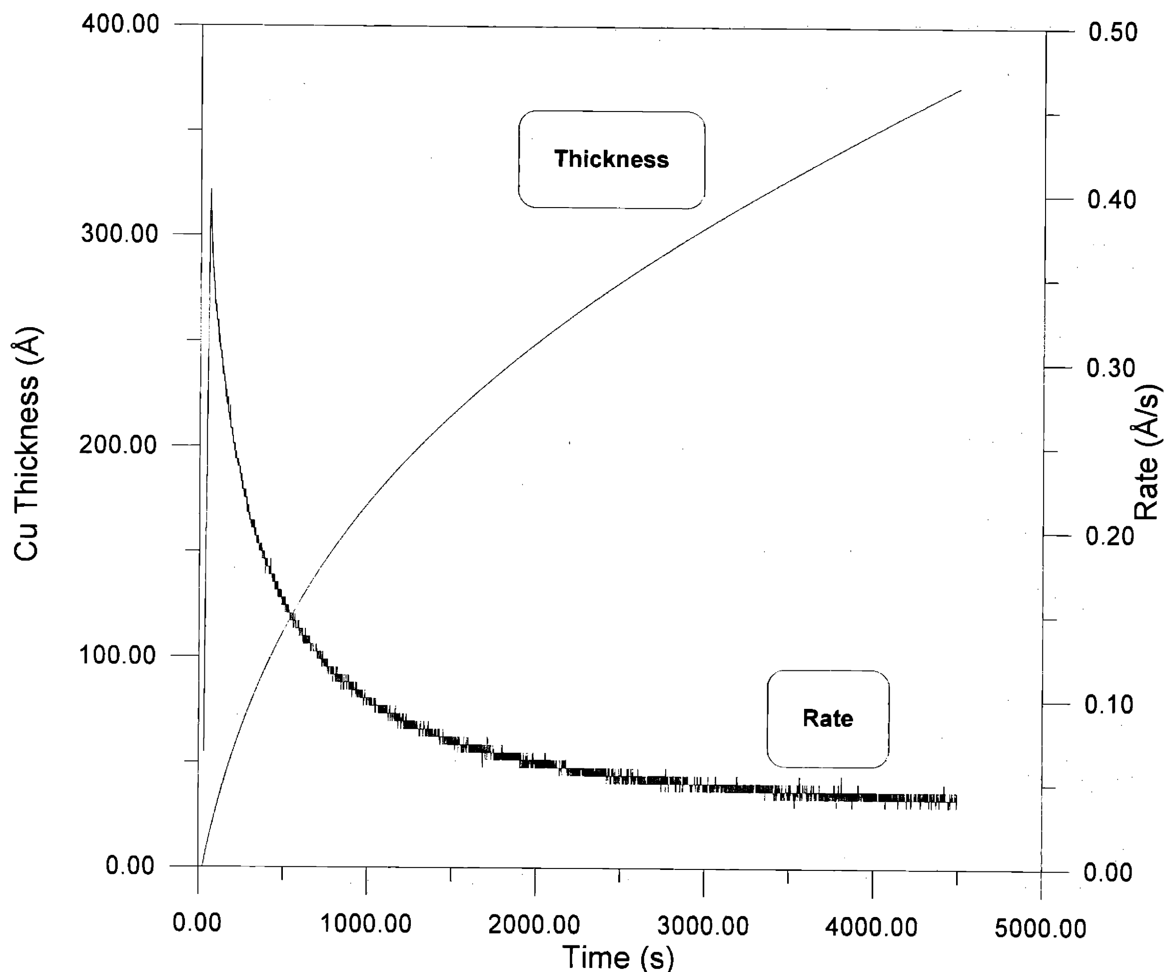

Figure 4.13: Rate and film thickness versus time for thermal CVD at 100°C on QCM substrate. The surface was sputter cleaned before starting the deposition.

Figure 4.14 further illustrates this process. The experiment monitored the deposition rate with and without ion enhancement at 100°C and 1.5 μA/cm^2. The initial deposition rate was approximately 0.75 Å/s, which is 7-8 times faster than II-CVD at 25°C at the same ion flux. Then the ion gun was shut off and the film continued to grow via thermal CVD. The rate decayed as depicted in Figure 4.13. After 2000 seconds the ion gun was turned on again and the growth rate re-established itself at 0.8 Å/s.

This effect also lends credence to the extension of Chiang's surface kinetic model. Clearly, the ion flux enhances byproduct desorption. Therefore, K_{des} must

scale with the ion flux rather than being independent as originally proposed by Chiang.

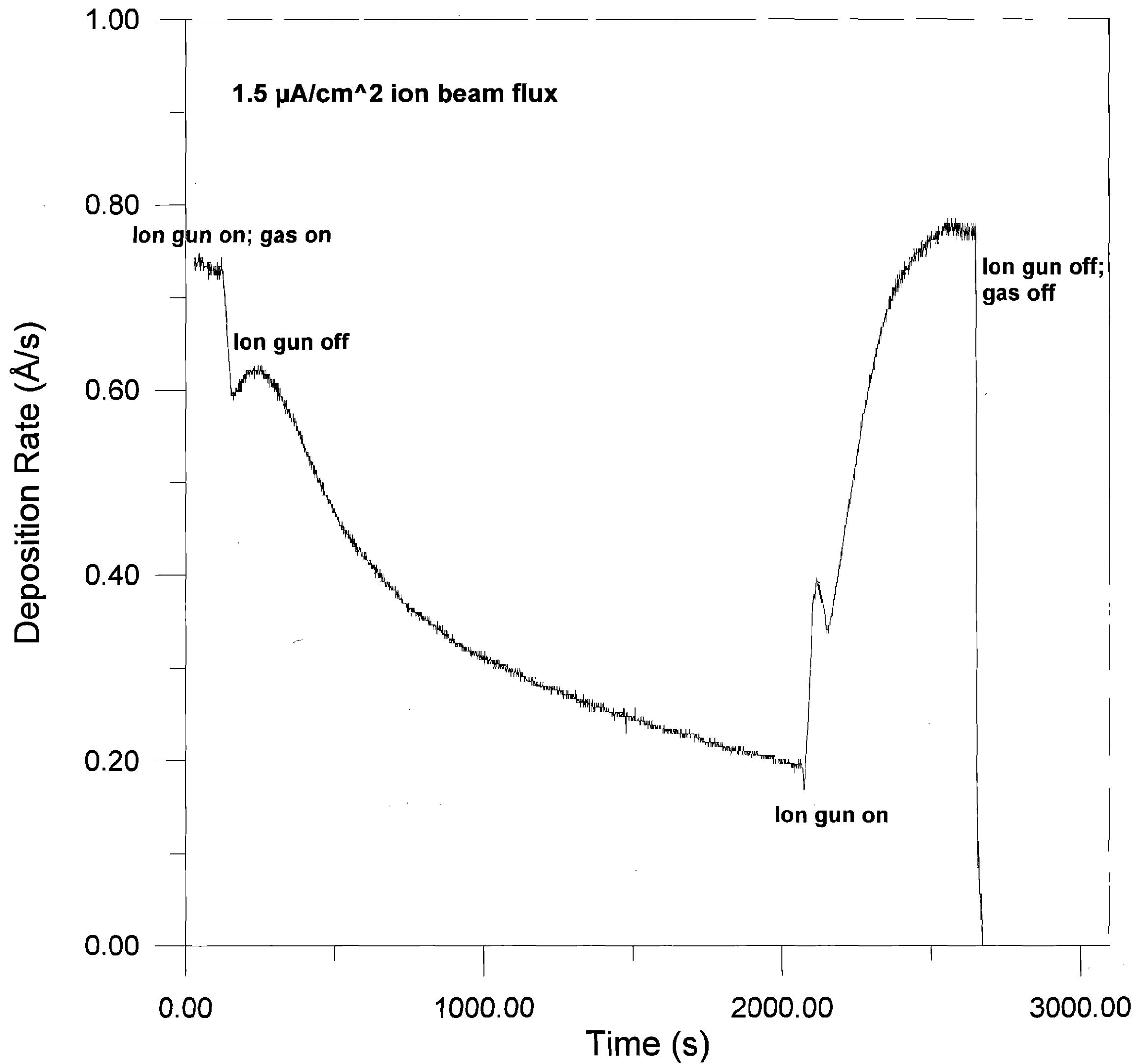

Figure 4.14: Rate experiment that investigates the effect of ion flux for CVD at 100°C. The substrate was sputter cleaned before starting the deposition. After establishing an initial growth rate the ion gun was turned off. After 2000 seconds the ion gun was turned on again for a short time interval before shutting off both the ion gun and gas source.

4.6 Discussion

The microstructure model relies on ion enhanced surface diffusion to explain the fact that column diameter remains invariant at constant temperature in the ion-flux-limited regime of II-CVD. The model fits the data accurately at all temperatures except 43°C, which is due to anomalies in the experimental data. The model does fall short of predicting the microstructure evolution at high ion fluxes in the gas-flux-limited regime. This either relates to the over-simplification in assuming that the diffusion equation pre-exponential scales linearly with the ion flux, or the difficulty in obtaining accurate data under these deposition conditions.

The model describes a mechanism that leads to morphological instability and cellular growth. Capillarity counteracts this growth process. For II-CVD of copper from Cu(I)hfac(VTMS) it appears that capillarity does not restrict the process for the examined deposition conditions; deposition at 200V and 25°C is the only exception. Here, a combination of lower surface diffusion enhancement and higher carbon fraction produces a characteristic column diameter that is too small to overcome capillarity. Similarly, deposition at 200V and 43°C has irregular surface coverage where cellular growth appears to be shut off in certain areas. Otherwise, cellular growth proceeds for all other deposition conditions that were investigated with this chemical precursor; the smallest observed average column diameter is 10.7 nm at 25°C and 300V. At the other extreme, cellular growth proceeds at 100°C where the carbon fraction is below 1%. *Only the nominally pure H-atom assisted deposition exhibits an equiaxed non-cellular microstructure because the carbon impurity has been eliminated.*

Figure 4.15 bolsters the argument for cellular growth. The TEM image shows a deposition where the initial growth condition was hydrogen atom beam assisted, which yielded an equiaxed grain structure (approximately 200 nm thick). Upon

extinguishing the hydrogen atom beam the microstructure transitioned abruptly to the characteristic columnar appearance. A nucleation and growth mechanism would not exhibit this abrupt transition. The sample was imaged in a region that was heavily etched during sample preparation.

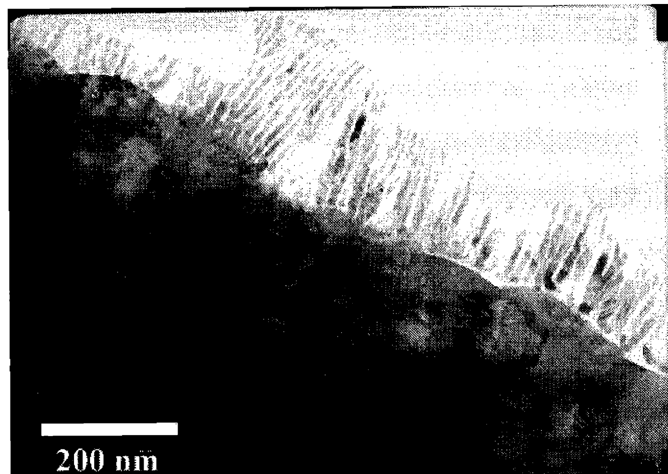

Figure 4.15: Characteristic columnar microstructure in area that has been heavily etched during sample preparation. The bottom layer was a Hydrogen atom beam assisted deposition, which accounts for the equiaxed microstructure.

Figure 4.16 also provides evidence supporting the cellular growth mechanism. The XTEM shows a sandwich of three II-CVD films grown near minimum deposition rates. Note the sharp transition between the bottom (71°C) and middle layer (25°C). The bottom layer has a microstructure that is representative

of the mixed regime where thermal CVD plays a role. The transition can only be the result of a cellular growth mechanism. A nucleation and growth process would not exhibit an immediate transformation in growth process, especially at such a low growth rate. The surface was sputtered before resuming growth at the new temperature setting. This assures that a nucleation and growth mechanism would not be interrupted by build-up of adsorbate. On the other hand, there is no apparent boundary between the 25°C and 43°C layers. The increase in characteristic average column diameter is only 15% and the change in characteristic column density is less than 10%. This represents an insufficient perturbation in the growth conditions for the formation of an abrupt transition. Thus, it does not disqualify cellular growth.

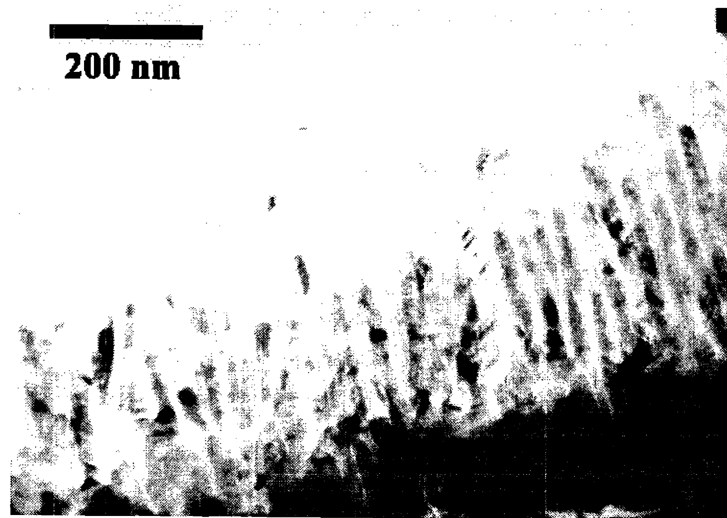

Figure 4.16: XTEM sandwich of three II-CVD films. Bottom: 71°C and 0.15 Å/s. Middle: 25°C and 0.1 Å/s. Top: 43°C and 0.1 Å/s. There is no boundary between middle and top layer. 500 eV ions. Each film is nominally 150 nm thick.

Chapter 5: Conclusions and Future Work

This thesis presents a successful model for II-CVD leading to cellular growth where surface diffusion of the carbon impurity dictates the column spacing of the characteristic microstructure. The model assumes that the ion flux has an approximately linear effect upon the diffusion constant's pre-exponential. The model is quite successful in predicting the constant column diameter observed for temperatures up to 61°C and it even predicts the increase in column diameter at low growth rate for deposition at 79°C.

On the other hand, the model falls short of accounting for trends in the "gas-flux-limited regime". This could be due to the over-simplification of the linear effect of ion bombardment on the surface diffusion or possibly a deviation from non-linearity when the ion flux to growth rate ratio becomes very large. Furthermore, the film composition could not be quantified in this regime and it was highly susceptible to experimental error. Clearly, this calls for further investigation of deposition in this regime. It may yield information that could improve the microstructure model and further quantify the relationship between ion flux and surface diffusion. The existing apparatus did not allow for accurate data collection in this regime because the gas flux was extremely sensitive to sample positioning.

The ion beam voltages examined in this thesis (up to 1000V) are much lower than those used in commercial FIB systems where typical beam voltages are 25kV and up. The data show that the column diameters increase with voltage. There is a significant increase in column diameter in going from 200V to 500V but the difference is not as a great when comparing 500V to 1000V ion beam flux. In fact, the microstructure model suggests that the increase for the latter case is exclusively due to an increase in film purity at higher temperature. Thus, the effect of ion bombardment on surface diffusion is independent of voltage

above ~500V. Nevertheless, it would be interesting to further examine the effects of voltage by, for example, using a 5kV ion gun with the current apparatus.

The applicability of these relatively low voltage and low ion flux experiments to commercial FIB deposition might be questioned. The FIB is rastered across the surface and an area sees an ion flux of ~1 A/cm^2 for a dwell time on the order of 1 μs. As long as the precursor gas is not depleted over this period of time – i.e. the dwell time is sufficiently short – then it is analogous to the ion-flux-limited regime. Empirically, FIB has produced similar microstructures even though the column diameters may be slightly larger. The slight increase in column diameter is due to the slight increase in purity with ion beam voltage. *Thus, the microstructure model can also be applied to FIB deposition.*

Depositing nominally pure copper films at room temperature with the H-atom assisted deposition process is also a tremendous scientific breakthrough. The next step would be to modify a commercial FIB and test to see if sufficient carbon removal is possible with the high instantaneous ion beam flux. Also, it would be useful to discover other reactive species that are easier to produce and deliver than hydrogen atoms.

While applications in FIB microsurgery are important, the possibility of controlling the nano-cellular microstructure opens up other possible applications. Armed with an understanding of the II-CVD mechanism, it allows further investigation of deposition of thin film systems where phase segregation is desirable. With a suitable precursor, the II-CVD process could, for example, grow high-density magnetic thin films. The interlaced impurity would isolate the magnetic metal columns. Although the recording heads will continue to limit the achievable magnetic recording density for some time, this nanoscale microstructure would enable media densities on the order of a terabit/in^2. This constitutes a new frontier for II-CVD processing and it could also foster research into wafer-scale II-CVD systems in order to make it commercially viable.

Appendix A: Volume Fraction of Close Packed Columns

Volume fraction of a close packed array of columns. The hexagon in Figure A-1 covers the area of three columns. The area or volume fraction is given by:

$$f = \frac{3\pi(d/2)^2}{6d(d/2)(\sin(60))} = \frac{\pi}{4\sin(60)} = 0.906$$

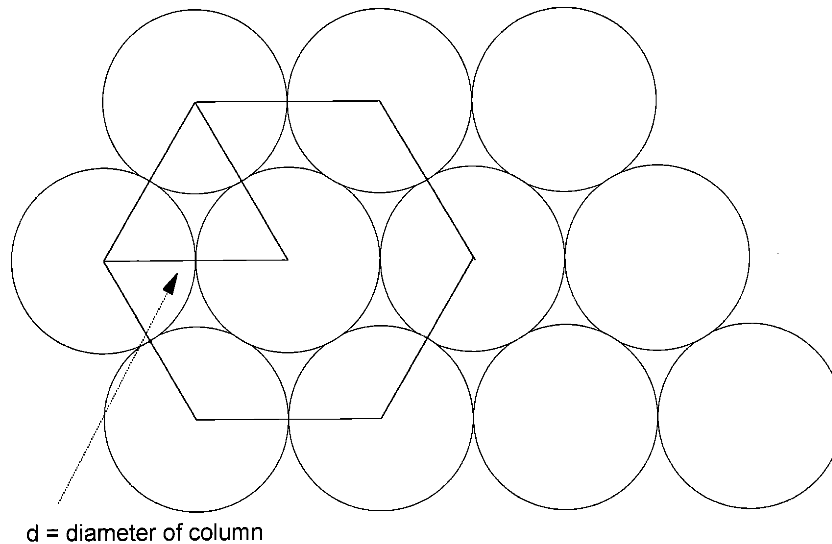

Figure A-1: Geometry of close packed array of columns in cross-section

Appendix B: Microstructure Model

Equation for surface diffusion; expressed in cylindrical coordinates:

$$\frac{\partial c}{\partial t} = \frac{\tilde{D}_s}{r}\left(r\frac{\partial^2 c}{\partial r^2} + \frac{\partial c}{\partial r}\right) - \frac{vc}{\delta} + \frac{vc_0}{\delta} = 0$$

Fick component | sink term | source term arriving with composition c_0

δ = surface boundary thickness | v = growth rate

At steady-state after multiplying by r^2:

$$r^2\frac{\partial^2 c}{\partial r^2} + r\frac{\partial c}{\partial r} - \left(\frac{c}{l^2}\right)r^2 + \left(\frac{c_0}{l^2}\right)r^2 = 0$$

The equation is written in the form of a BESSEL function

where $l = \sqrt{\frac{\delta D}{r}}$

General solution: $c = C_1 I_0\left(\frac{r}{l}\right) + C_2 K_0\left(\frac{r}{l}\right)$

Particular solution (where c is constant): $-c\left(\frac{r^2}{l^2}\right) + c_0\left(\frac{r^2}{l^2}\right) = 0 \Rightarrow c = c_0$

So, $c = C_1 I_0\left(\frac{r}{l}\right) + C_2 K_0\left(\frac{r}{l}\right)_1 + c_0$

Boundary conditions:

$$\frac{\partial c}{\partial r}=0 \text{ at } r=0 \qquad \text{(center of column)}$$

$$\Rightarrow C_2=0 \text{ since } K_1(0)\rightarrow\infty$$

$$c=0 \text{ at } r=R \qquad \text{(boundary of column)}$$

$$\Rightarrow C_1=\frac{-c_0}{I_0\left(\frac{R}{l}\right)}$$

So $c=c_0\left(1-c_0\frac{I_0\left(\frac{r}{l}\right)}{I_0\left(\frac{R}{l}\right)}\right)$

The carbon concentration (c) is at its thermodynamic solubility limit at $r=0$:

$$c_{LIM}=c_0\left(1-\frac{I_0(0)}{I_0\left(\frac{R}{l}\right)}\right)$$

$$\Rightarrow I_0\left(\tfrac{R}{l}\right)=\frac{1}{1-\frac{c_{LIM}}{c_0}}$$

$$\Rightarrow R=\sqrt{\frac{\tilde{D}_S\,\delta}{v}}\,I_0^{-1}\left(\frac{1}{1-\frac{c_{LIM}}{c_0}}\right)$$

Then the Ion flux dependent terms are separated in the expression for *R*:

$$\Rightarrow R = \sqrt{\exp\ (-E_A / kT)\ \delta}\ \sqrt{\frac{D_0}{\mathrm{v}}} I_0^{-1} \left(\frac{1}{1 - \frac{c_{LIM}}{c_0}} \right)$$

where $\sqrt{\frac{D_0}{\mathrm{v}}}$ is the Ion-flux dependent term.

Appendix C: Glossary

AFM	Atomic Force Microscopy.
Cu(I)hfac(vtms)	Copper hexafluoroacetylacetonate vinyltrimetylsilane; the metalorganic precursor for copper that was used in this work.
Cupraselect®	Schumacher's registered trademark name for Cu(I)hfac(vtms).
DMGhfac	Dimethylgold hexafluoroacetylacetonate: metalorganic precursor for gold that was used in earlier II-CVD research at MIT.
FIB	Focused Ion Beam.
FIBD	Focused Ion Beam Deposition: localized direct-write II-CVD using a focused ion beam.
II-CVD	Ion-induced Chemical Vapor Deposition
LITD	Laser Induced Thermal Desorption: technique that was used by Chiang to detect chemical species on the surface during II-CVD.
OFHC	Oxygen Free High Conductivity (Copper)
QCM	Quartz Crystal Microbalance: instrument that monitors instantaneous thin film growth rate.
SEM	Scanning Electron Microscopy.
STEM	Scanning Transmission Electron Microscopy.
STEM-EDS	Scanning Transmission Electron Microscopy - Energy Dispersive x-ray Spectroscopy.
TEM	Transmission Electron Microscopy.
XPS	X-ray Photoelectron Spectroscopy: analytical technique that is used for quantitative compositional analysis in this work.
XTEM	Cross-sectional Transmission Electron Microscopy.

Endnotes

[1] Micrion, Peabody, MA. (Company later acquired by FEI Company, Hillsboro, OR.)

[2] Formerly reported by IBM at http://www.chips.ibm.com/services/asg/appnotes/app06.html

[3] http://www.ibm.com/chips/techlib/techlib.nsf/techdocs/90D608583DF6C8EF87256C7C00566304/$file/focused_lowbeam.pdf

[4] G Stengl, H Löschner, W. Maurer and P. Wolf, SPIE Symp. Microlithography, March 10-15, 1985.

[5] A consortium created to commercialize IPL.

[6] W. Finkelstein and A. Mondelli, Semiconductor International, May 1995.

[7] K. Gamo et al., Japan J. Appl. Phys. **23**, L293 (1984).

[8] P. G. Blauner, Y. Butt, J. S. Ro, C. V. Thompson, J. Melngailis, J. Vac. Sci. Technol. B **7**, 1816 (1989).

[9] A. D. Dubner, "Mechanism of Ion Induced Deposition", Ph.D. Thesis MIT (Sept. 1990)

[10] A. D. Dubner, A. Wagner, J. Appl. Phys. **66**, 870 (1989)

[11] A. D. Dubner, A. Wagner, J. Appl. Phys. **65**, 3636 (1989)

[12] T.P. Chiang, "Surface Kinetic Study of Ion Induced Chemical Vapor Depositon of Copper", Ph.D. Thesis MIT (February, 1996)

[13] Schumacher Co., Carlsbad, CA. (A subsidiary of Air Products Inc.)

[14] L. H. Dubois, P. M. Jeffries, G. S. Girolami, Mater. Res. Soc. Symp. Proc. V-7, 375 (1992)

[15] G. Zau, Ph.D. Thesis, unpublished.

[16] J-S Ro, "Microstructure and Mechanism of Gold Films Grown by Ion Induced Deposition", Ph.D. Thesis MIT (June 1997).

[17] C.R. Brundle, C.A. Evans, S. Wilson, eds., *Encyclopedia of Materials Characterization*, Butterworth-Heinemann, Stoneham, MA, 1992.

[18] Sharon Vacuum Company, Brockton, MA.

[19] FEI Company, Hillsboro, OR.

[20] CTI-Cryogenics, a division of Helix Technology Corporation, Mansfield, MA.

[21] Leybold Vakuum GmbH, Cologne, Germany.

[22] Sycon Instruments, Syracuse, NY.

[23] Schumacher Co., Carlsbad, CA. (A subsidiary of Air Products Inc.)

[24] J. A. T. Norman, B. A. Muratore, P. N. Dyer, D. A. Roberts, A. K. Hochberg, J. de Physique IV, C2-271 (1991).

[25] Commonwealth Scientific, Alexandria, VA.

[26] Kimball Physics, Wilton, NH.

[27] Ion Tech, Fort Collins, CO. (A subsidiary of Veeco Instruments.)

[28] ASTeX Products, Wilmington, MA. (A subsidiary of MKS Instruments, Andover, MA.)
[29] B.J. Wood, H. Wise, J. Phys. Chem. **66**, 1049 (1962).
[30] J. Geddes, R.W. McCullough, A. Donnelly, H.B. Gilbody, Plasma Sources Sci. Technol.**1,** 93 (1993).
[31] JEOL USA, Inc., Peabody, MA.
[32] Ted Pella Inc., Redding, CA.
[33] Anthony D. Della Ratta, "Focused Ion Beam Induced Deposition of Copper", S.M. Thesis MIT (June, 1993).
[34] H.R. Kaufman, *Fundamentals of Ion-Source Operation,* Commonwealth Scientific, Alexandria, VA, 1984.
[35] M-Line Accessories Measurements Group, Inc., Raleigh, NC.
[36] VCR Group, South San Francisco, CA.
[37] Gatan, Inc., Pleasanton, CA.
[38] Topometrix Corporation, Santa Clara, CA. (Acquired by Veeco Instruments, Plainview, NY.)
[39] Perkin Elemer Instruments, Norwalk, CT.
[40] C.R. Brundle, "XPS Photelectron Spectroscopy" in C.R. Brundle, C.A. Evans, S. Wilson, eds., *Encyclopedia of Materials Characterization*, Butterworth-Heinemann, 1992.
[41] VG Microscopes, East Grinstead, United Kingdom. (Subsidiary of Fisons Ltd.)
[42] Link/Oxford, High Wycombe, United Kingdom.
[43] J.I. Goldstein et al., *Scanning Electron Microscopy and X-Ray Microanalysis,* Plenum PresshNew York, 1984.
[44] L.B. Valdes, *Proc. IRE*, **42**, 420 (1954).
[45] Alessi Inc., Irvine, CA.
[46] Jian Li, Robert Blewer, and J.W. Mayer, "Copper-Based Metallization for ULSI Applications," MRS Bulletin, June 1993.
[47] J.A.T. Norman, B.A. Muratore, P.N. Dyer, D.A. Roberts, A.K. Hochberg, Journal de Phsique IV, C2-271 (1991).
[48] J.A.T. Norman, D.A. Roberts, A.K. Hochberg, Mater. Res. Soc. Symp. Proc. **282**, 347 (1992)
[49] V.M. Donnelly and M.E. Gross, J. Vac. Sci. Technol. A **11**(1), 66 (1993).
[50] M. E. Gross and V. M. Donnelly, Mater. Res. Soc. Conf. Proc. ULSI-VII, 355 (1992).
[51] L.H. Dubois, P.M. Jeffries, G.S. Girolami, Mater Res. Conf. Proc. ULSI-VII, 375 (1992).
[52] R.L. Fullman, Journal of Metals **5**, 449 (1953).
[53] C.S. Smith and L. Guttman, Journal of Metals **4**, 150 (1952).
[54] George F. van der Voort, *Metallography: Principles and Practice,* New York, 1984.

[55] J.E. Greene, S.A. Barnett, J.E. Sundgren and A. Rockett, "Low-energy Ion/surface Interactions During Film Growth From the Vapor Phase," in T. Itoh, ed., *Ion Beam Assisted Film Growth*, Elsevier Science, Amsterdam, 1989.

[56] Personal communication with H. Inglefield, MIT.

[57] J.E. Greene, S.A. Barnett, J.E. Sundgren and A. Rockett, "Low-energy Ion/surface Interactions During Film Growth From the Vapor Phase," in T. Itoh, ed., Ion Beam Assisted Film Growth, Elsevier Science, Amsterdam, 1989.

[58] J. W. Cahn, Acta. Met. **7,** 18 (1959).

[59] W.W. Mullins and R.F. Sekerka, J. Appl. Phys. **35**, 444 (1964).

[60] R. Trivedi and W. Kurz, Acta Met. **34**, 1663 (1986).

[61] C.H.J Van den Brekel and A.K. Jansen, J. Crystal Growth **43**, 364 (1978).

[62] C.H.J Van den Brekel, Philips J. Res. **33**, 20 (1978).

[63] Dirks, A.G., and H.J. Leamy, Thin Solid Films **47**, 219 (1977)

[64] D.J. Srolovitz, A. Mazor and B.G. Bukiet, J. Vac. Sci Tech. **A6**, 2371 (1988).

[65] B.A. Movchan and A.V. Demchishin, Fizika Metalov i Metalovedenije **28**, 653 (1969).

[66] J.A. Thornton, J. Vac. Sci. Tech. **A4**, 490 (1974).

[67] J. Chin, P.K. Gantzel, and R.G. Hudson, Thin Solid Films **40**, 57 (1977).

[68] H.J. Viljoen, J.J Thiart and V. Hlavacek, AIChE Journal **40**, 1032 (1994).

[69] M. Marinov, Thin Solid Films **46**, 267 (1977).

[70] C.M. Cotell, J.A. Sprague, and C.R. Gossett, Mat. Res. Soc. Symp. Proc. **202**, 31 (1991).

[71] H.R. Kaufman and R.S. Robinson, J. Vac. Sci. Technol. **16** (2), 175 (1979).

[72] S.M. Rossnagel, H.R. Kaufman and R.S. Robinson, Surface Science **123**, 89 (1982).

[73] D.C. Gray, "Beam Simulation Studies of Plasma-Surface Interactions In Flurocarbon Etching of Si and SiO_2", Ph.D. Thesis MIT (1992).

[74] G. Ehrlich, Surface Science **246**, 1 (1991).

[75] M. Atzmon, D.A. Kessler and D.J. Srolovitz, J. Appl. Phys. **72** (2), 442 (1992).

[76] C.D. Adams, M. Atzmon, Y-T. Cheng and D.J. Srolovitz, J. Mater Res. **7**, 653 (1992).

[77] T.B. Massalski, editor-in-chief, "Binary Alloy Phase Diagrams", ASM International, Materials Park, OH, 1990.